Title
Exploiting hydrophobic and electrostatic interactions for the effective removal of aqueous contaminants

Author
Rao, Unnati

Publication Date
2020

Peer reviewed|Thesis/dissertation

UNIVERSITY OF CALIFORNIA

Los Angeles

Exploiting hydrophobic and electrostatic interactions for the effective removal of aqueous contaminants

A dissertation submitted in partial satisfaction of the
requirements for the degree of Doctor of Philosophy
in Civil Engineering

by

Unnati Rao

2020

ABSTRACT OF THE DISSERTATION

Exploiting hydrophobic and electrostatic interactions for the effective removal of aqueous contaminants

by

Unnati Rao
Doctor of Philosophy in Civil Engineering
University of California, Los Angeles, 2020
Professor David Jassby, Chair
Professor Jennifer Ayla Jay, Co-chair

Water treatment processes using membrane technology, electrochemistry and nanomaterials have shown tremendous promise in the last several years. While pressure driven membrane treatment processes are capable of treating water sources containing a wide variety of contaminants, they suffer from several challenges such as osmotic pressure limitations and surface scaling and fouling. Membrane distillation is a vapor pressure driven process that does not suffer from osmotic pressure limitations, and hence can be used for the treatment of high salinity sources. However, fouling is still a major concern, along with the added high energy requirements. In this work, we look at a membrane distillation system that successfully separated non-volatile contaminants from a dairy farm waste stream, resulting in a concentrated stream of nutrients to be used as fertilizer, and a dilute stream of volatile compounds that can be used as the feed in fermentation processes. We also looked at treatment of high salinity brines by membrane distillation. Due to the excellent heat and electrically conductive properties of carbon nanotubes, an electrically conducting membrane fabricated by coating a polymeric membrane with a carbon nanotube suspension proved successful in mitigating inorganic scaling to a large extent. The externally applied electric potential reduced scale deposition by electrostatic repulsion and electrokinetic mixing. In another aspect of our research activities, we studied the degradation of perfluoroalkyl substances, a class of contaminants of

emerging concern that are highly recalcitrant carcinogenic compounds. Typical remediation of these compounds takes place through adsorption on activated carbon followed by incineration. Studies have shown that they can be degraded by electrochemical oxidation. We utilized the excellent sorption and electrically conductive properties of carbon nanotubes to develop a novel degradation mechanism, where an externally applied potential weakened the C-F bonds, and hydrated electrons generated by UV light resulted in defluorination. We extended this study to linear perfluoroalkyl substances having different chain lengths and headgroups, studied the feasibility of this mechanism on dechlorination of chlorinated solvents commonly co-occurring in groundwater, studied the impact of mixtures of perfluoroalkyl substances and verified the two-electron mechanism by evaluating degradation rates of isotopically labeled and unlabeled compounds.

The Dissertation of Unnati Rao is approved.

Sanjay K. Mohanty

Sharon L. Walker

Jennifer Ayla Jay, Committee Co-chair

David Jassby, Committee Chair

University of California, Los Angeles

2020

DEDICATION

This dissertation is dedicated to my parents, my fiancé, and the rest of my family who always encouraged me to pursue my dreams. Your encouragement and support kept me going.

TABLE OF CONTENTS

LIST OF FIGURES

LIST OF TABLES

ACKNOWLEDGEMENTS

I would like to thank my adviser, Dr. David Jassby, for his mentorship and extensive guidance. His support, optimism and patience have helped me overcome many frustrations and experimental failures, and have grown me as an individual and a researcher. The life lessons I learnt from him will continue to have a lasting influence on my life. His passion for research has inspired me to bring my best, and his constructive feedback has improved my writing skills. I also thank David giving me the opportunity to move to UCLA, and for his support during the transition. I would like to thank Dr. Sharon Walker for her guidance during the initial stage of my Ph.D., and her willingness to help whenever I reached out despite being at a different university. I deeply appreciate my committee members Dr. Jennifer Jay and Dr. Sanjay Mohanty for their time and help. Dr. Eric Hoek's guidance and support while at UCLA were instrumental in completing my degree.

In addition, I would like to acknowledge my friends and lab-mates, without whose help and support this would have been impossible. At my low points, they encouraged me to carry on. I particularly thank Dr. Yiming Su, who made major contributions in chapters 4 and 5. I also thank Dr. Alexander Dudchenko, Dr. Wenyan Duan, Dr. Caroline Kim and Dr. Xiaobo Zhu for their training and guidance. I started out as a clueless researcher, and they were extremely patient with all my questions. I appreciate the undergraduate students; Benjamin Rammelsberg at UCR; and Jin Sung Park, Alice Barber and Anna Kathryn Blake at UCLA who helped me extensively with experimental work.

VITA

2014 Master of Science in Civil and Environmental Engineering

Carnegie Mellon University, Pittsburgh, PA, USA

2013 Bachelor in Engineering in Chemical Engineering

University of Mumbai, Mumbai, India

JOURNAL PUBLICATIONS

Unnati Rao, Yiming Su, Chia Miang Khor, Bongyeon Jung, Shengcun Ma, David M. Cwiertny, Bryan M. Wong, David Jassby. "Structural Dependence of Reductive PFAS Defluorination in a UV/Electrochemical System". *Environmental Science and Technology (2020).*

Unnati Rao, Arpita Iddya, Bongyeon Jung, Chia Miang Khor, Zachary Hendren, Craig S. Turchi, Tzahi Y. Cath, Eric M.V. Hoek, Guy Z. Ramon, David Jassby. "Mineral Scale Prevention on Electrically Conducting Membrane Distillation Membranes using Induced Electrophoretic Mixing". *Environmental Science and Technology. (2020, vol 54, issue 6, 3678-3690)*

Unnati Rao, Roy Posmanik, Lindsay E. Hatch, Jefferson W. Tester, Sharon L. Walker, Kelley C. Barsanti, and David Jassby. "Coupling hydrothermal liquefaction and membrane distillation to treat anaerobic digestate from food and dairy farm waste." *Bioresource technology* 267 (2018): 408-415.

Yiming Su, **Unnati Rao,** Chia Miang Khor, Madeline G. Jensen, Lynn M. Teesch, Bryan M. Wong, David M. Cwiertny, David Jassby. "Potential-Driven Electron Transfer Lowers the Dissociation Energy of the C–F Bond and Facilitates Reductive Defluorination of Perfluorooctane Sulfonate (PFOS)". *ACS Appl. Mater. Interfaces (2019, volume 11, issue 37, 33913-33922)*

Bongyeon Jung, Caroline Y. Kim, Shiyuan Jiao, **Unnati Rao**, Alexander V. Dudchenko, Jefferson Tester, David Jassby. "Enhancing boron rejection on electrically conducting reverse osmosis membranes through local electrochemical pH modification". *Desalination. (2019, vol 476, pages 114-212)*

Jishan Wu, Jingbo Wang, Yiming Liu, **Unnati Rao**, Eric M.V. Hoek, David Jassby, Richard B. Kaner. "Sustainable Desalination and water reuse" *(Book, submitted)*

Presto, Albert A., Timothy R. Dallmann, Peishi Gu, and **Unnati Rao**. "BTEX exposures in an area impacted by industrial and mobile sources: source attribution and impact of averaging time." *Journal of the Air & Waste Management Association 66, no. 4 (2016): 387-401.*

PATENTS

David Jassby, **Unnati Rao**, Eric M.V. Hoek. "Prevention of mineral scale on electrically conductive membranes" U.S. Provisional Application No. 62/946,064

CONFERENCE PRESENTATIONS

Mitigating Mineral Scaling on Desalination Membranes via Induced Electrophoretic Mixing. *North American Membrane Society Annual Meeting 2019, Pittsburgh, PA. May 11-15, 2019.*

Sustainable Use of Dairy Farm Anaerobic Digestate: from Environmental Pollutant to New Source of Water, Energy and Nutrients. *ACS National Meeting, Spring 2019, Orlando, FL. March 31-April 4, 2019.*

Chapter 1: Introduction

1.1 Resource Depletion and Water Scarcity

Overpopulation occurs when a population cannot be sustained due to the rapid depletion of resources[1], which cannot be replenished in time frames meaningful to humans. Accelerated technological progress has ensured longer lifespans[2], and the population is projected to reach over nine billion by the year 2050.[3] Limited resource availability is a serious concern, as the increasing population will demand food, water and energy in larger quantities.[4] There is a fixed quantity of each resource available to us, and if we consume them at a faster rate than their replenishment, it is only a matter of time before they run out. Resource recovery is the process of selectively extracting useful resources from waste products, which can be further recycled and reused to sustain the growing population.[5]

Agricultural yields and productivity have dramatically increased with the use of fertilizers, which provide nutrients essential for crop growth. Fertilizer production is highly energy intensive, and accounts for a third of the total energy utilized in the U.S.[6] Recovering resources from waste streams that contain these nutrients could supplement traditional fertilizer production, thus reducing the energy impact of fertilizer production. Waste streams from food and dairy manure contain significant amounts of these nutrients, and selectively separating them could be an effective strategy for fertilizer production. Traditionally, these streams are disposed in landfills, which leads to a host of other environmental concerns such as groundwater contamination due to landfill leachate.[7] Agricultural waste streams also contain a significant amount of carbon, which can be extracted for use in the form of biofuel. These reactions are typically conducted at high pressures and are not economical when compared to fossil fuel production.[8] However, in the future, as fossil fuel sources are rapidly depleted, they can potentially become more important. This, combined with the possibility of reducing environmental impacts due to waste disposal, make resource recovery from agricultural wastes an attractive pathway in the future.

Water is essential for life and all human activities, and the most important of these resources. 71% of the earth's surface is covered by water. However, nearly 97% of this is present in the oceans as salty water. The remaining (little over 3%) is held by glaciers, ice caps, surface water sources (lakes, rivers, streams,

etc.), aquifers, and in air as water vapor. Traditionally, surface water and groundwater sources have been used for domestic and industrial applications, and these resources have been adequate to sustain the human population. However, due to the increase in population over the last few centuries, rapid industrialization, and the resulting climate change, the world is facing drastic water shortage and scarcity issues. Interestingly, the world is facing a problem of too much water in some places, and not enough water in others. As of 2018, fourteen of the world's twenty megacities experienced water scarcity or drought-like conditions.[9] Water demand originates from four sources- agriculture, industries, energy generation and human consumption.[10] Climate change and rising bioenergy demands further exacerbate water shortage.[11] To add to this, human activities release toxic and non-toxic pollutants, that make water unusable without treatment.

To combat these challenges, better water management practices, efficient and economical methods of obtaining clean water from non-conventional sources (seawater, geothermal brines, etc.), and improved treatment techniques for existing water sources and water treatment systems are required. Strategies to address water scarcity include water reuse from contaminated sources (groundwater, wastewater, etc.) and desalination (extracting pure water from seawater or brackish water).

There is tremendous potential for nutrient, energy and water recovery from wastewater, water recovery (treatment) of saline streams (seawater and brackish water), as well as contaminated groundwater. The common ground in resource recovery and water treatment (recovery) is the separation (and subsequent degradation in case of contaminated groundwater) of a foreign entity in a water matrix. On the molecular level, these entities interact with each other, with other surfaces, and with water molecules by intermolecular forces. A better understanding of these intermolecular forces is the first step in developing effective methods of separation, in turn resulting in more effective resource recovery and water treatment.

1.2 Intermolecular Forces

Intermolecular forces between aqueous species include attraction and repulsion; they are non-covalent interactions, and do not involve any sharing or exchange of electrons.[12] The non-covalent intermolecular forces that are of importance in separation processes are electrostatic effects, Van der Waals forces and hydrophobic effects.[13]

1.2.1. Electrostatic Forces and the Electrical Double Layer

The electrostatic potential is created by a system of nuclei and electrons. Molecules or ions that have permanent charges interact with each other according to Coulumb's Law.[14] Oppositely charged species attract, while like charged species repel.[15] In aqueous systems, surface charges come about in two ways – by the dissociation of surface groups, or by the adsorption of ions on the surface.[16] Ionic bonds are formed by the transfer of electrons between two atoms. Thus, when an ionic molecule dissociates in water, charged entities are formed, which are able to interact with each other and with other charged entities.

When a solid is immersed in a liquid, the properties at the solid-liquid interface are different from the properties of the extended solid or liquid phase. This is because the solid surface is charged, and these charges affects the charge distribution in the liquid phase. The surface attracts oppositely charged particles (counter-ions) in the fluid, while repelling similarly charged ions (co-ions). Some of these counter-ions are sorbed on the surface (Stern layer), while most others form a diffuse layer along the surface, effectively screening the surface charge. This results in a region of high concentration of counter-ions along the surface and a low concentration of co-ions. As the distance from the surface increases, the counter-ion/co-ion ratio is restored. This results in the formation of a thin double layer close to the surface, consisting of the surface charge and the diffuse layer of counter-ions (Figure 1). In the electrical double layer, there is an imbalance in the ratio of co and counter ions. As the distance from the charged surface increases, this balance is restored.[17] According to the Guoy-Chapman model, the interfacial potential is due to the presence of the charges on the surface, and an equal number of oppositely charged

ions in the solution. Thus, the double layer extends until the counter-potential restricts their tendency to diffuse.[18] The Poisson-Boltzmann equation can be used to predict the potential distribution near the surface. However, this equation assumes that ions are point charges, and is only valid at low ionic concentrations and surface charge. To account for the volume occupied by ions, the modified Poisson-Boltzmann equation was formulated. As we move away from the surface, the potential drops linearly in the Stern layer, and exponentially in the diffuse layer. This allows us to predict the concentration of ions in the electrical double layer.[19] The electrical double layer extends only up to a few nanometers, with the length inversely proportional to the ionic strength of the fluid.[20] This is because at greater ionic strengths, the potential drop is much more rapid, which neutralizes the surface charge. The double layer is thus formed to neutralize the surface charge, and results in the formation of an electrokinetic potential between the surface and any point in the liquid phase. When a charged body is influenced by an electric field, it moves with a fixed velocity. This is known as electrophoresis.[21] The plane that separates the moving particle from the bulk liquid is known as the slip plane, and the electric potential at this point is known as the zeta potential (The potential drop across the diffuse layer).[22]

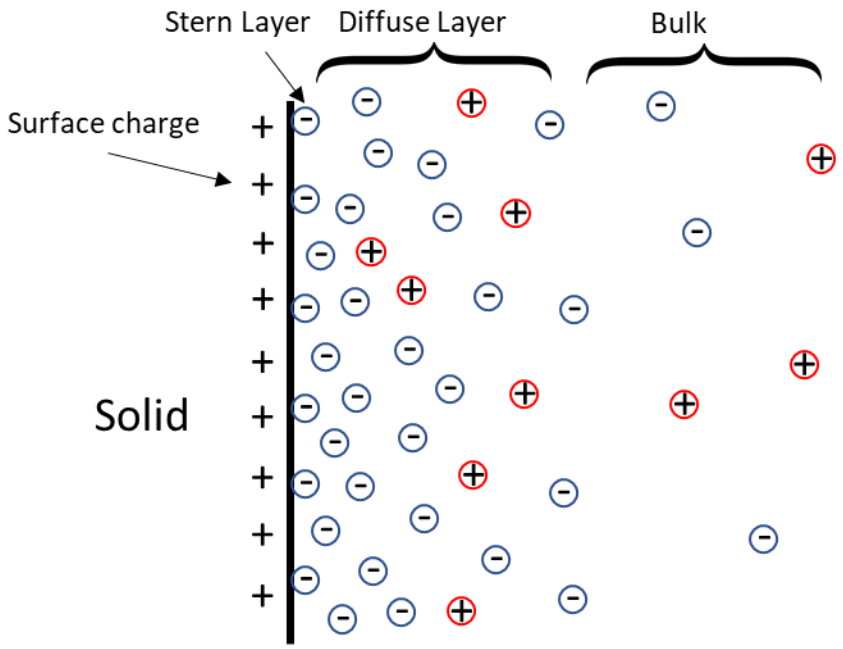

Figure 1: Electrical Double Layer Structure

1.2.2. Van der Waals Forces

Van der Waals forces are intermolecular attractive and repulsive forces, that act at short distances. They are the result of the fluctuating polarities of neighboring particles, and are manifesting in the following three forms: The London dispersive force, the Debye force, and the Keesom force. Van der Waals forces are long-range, and their effect decreases with distance, according to a power law.[23] An atom or molecule can have two kinds of dipole moments: Permanent dipole moments, and induced dipole moments. Permanent dipole moments are formed when atoms of different electronegativities form bonds, resulting in fixed regions of high electron concentration (negative charge) and low electron concentration (positive charge) that exist at a distance from one another within a molecule (Figure 2). Such molecules are known as polar molecules. When a non-polar atom or molecule is influenced by an electric field, its electron cloud is distorted as it responds to the electric field. This results in the formation of a positive and negative charge within the atom or molecule, known as an induced dipole moment.[24] The force between two molecules having permanent dipole moments is known as Keesom force. The interaction between a molecule having a permanent dipole moment and a molecule having induced dipole moment is known as Debye force, and the interaction between two atoms or molecules having induced dipole moments is known as the London dispersion force.[25]

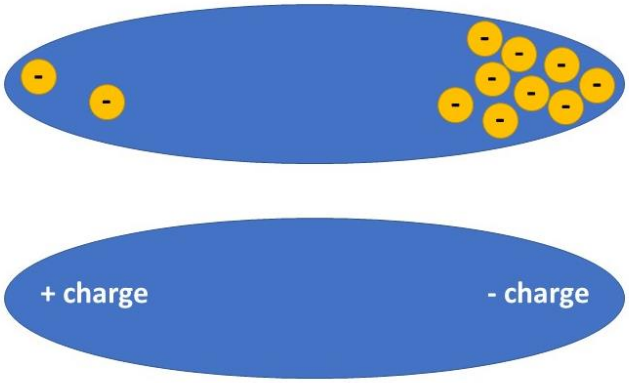

Figure 2: Formation of dipoles in an atom/molecule

1.2.3 Hydrophobic Forces

The large electronegativity difference between hydrogen and oxygen causes water to be a strongly polar molecule. In a water matrix, the electron rich oxygen atoms attract the neighboring electron poor hydrogen atoms, forming hydrogen bonds. Thus, hydrogen bonds are a kind of electrostatic interaction.[26] They are formed in compounds containing hydrogen linkages to other very electronegative atoms such as N, O or F. However, hydrogen bonding in water is particularly strong, because a single water molecule is capable of forming four hydrogen bonds – two involving their own hydrogen atoms, and two involving hydrogen atoms in neighboring water molecules. Hydrogen bonding is responsible for several of the unique properties of water, such as its strong surface tension, high boiling point considering its size, and excellent ability as a solvent for polar molecules. It is also the reason that water molecules form hydration shells around other ions and molecules. In order to accommodate a non-polar compound (hydrophobe), the following steps are necessary. (i) Creation of a cavity in the water matrix, which requires hydrogen bonds to be broken, (ii) Structuring of water molecules around the hydrophobe, which results in an orderly formation (Figure 3).[27] This is not entropically favorable, as it results in a decrease in entropy (due to a more orderly structure). When two non-polar entities are in a water matrix, the water molecules move away and the two objects have a tendency to coalesce so as to minimize the contact area between water and these non-polar solvents. This water-repelling tendency is known as the hydrophobic effect.[28] Hydrophobic forces can act at distances up to 10nm.[29, 30]

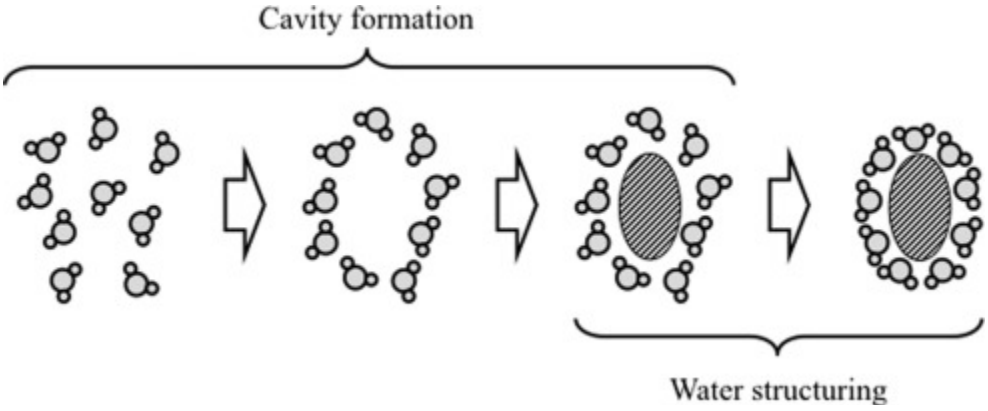

Figure 3: Effect of non-polar solutes in water

In this work, we focus on modifying surface hydrophobic and electric properties in order to improve water treatment processes. We will now discuss membrane technology, one of the primary methods of water treatment, the challenges associated, and how we can tailor surface hydrophobicity and electrical properties to address these challenges.

1.3 Membrane Technology

Membrane technology is capable of seawater and brackish water desalination, as well as purification of contaminated water sources. It is widely used in water treatment processes, and consists of a semi-permeable physical barrier (membrane) that allows the transport of certain molecules through its pores, while retaining others.[31] It can be used for liquid as well as gas separations. Selective transport through the membrane can be due to steric effects (on the basis of size), or Donnan effects (on the basis of charge). Membranes face a number of challenges such as high energy demands, thermodynamic constraints, the need for costly materials and fabrication processes, membrane fouling and scaling, pretreatment requirements, poor rejection of uncharged solutes having small sizes, etc.[32, 33]

1.3.1 Membrane Classification and Transport Mechanisms

Microfiltration (MF), ultrafiltration (UF), nanofiltration (NF), reverse osmosis (RO), electrodialysis (ED), forward osmosis (FO), pervaporation (PV) and membrane distillation (MD) are the most common membrane separation processes. Of these, MF, UF, NF, RO are pressure driven, MD and PV are partial (vapor) pressure driven, FO is osmotic pressure driven and ED is driven by an applied electric potential.

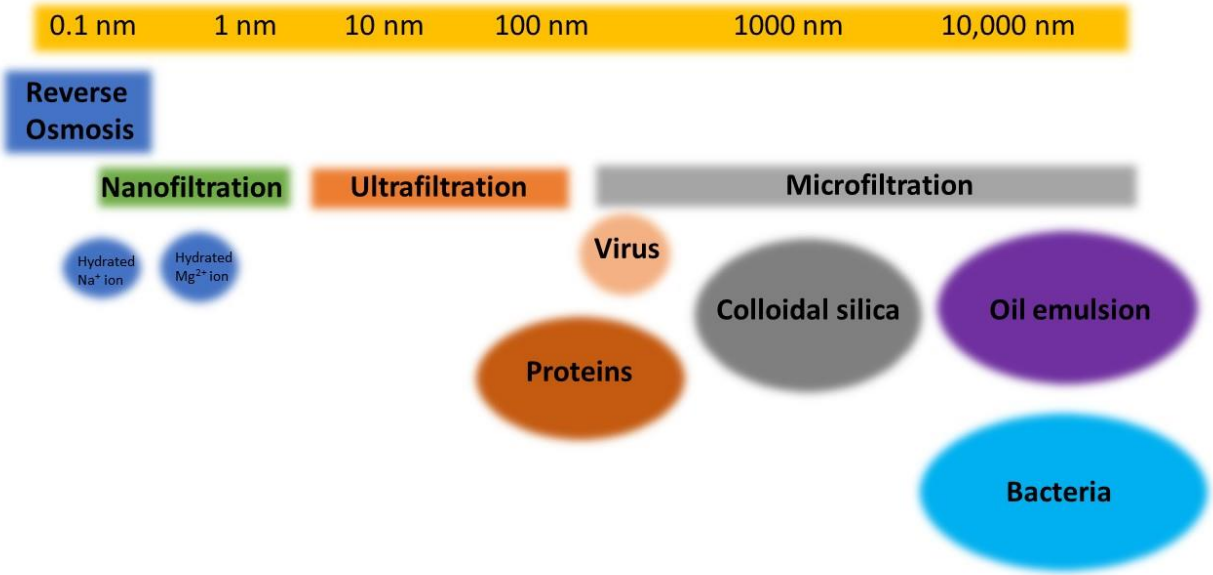

Figure 4: Membrane cut-off characteristics

Figure 4 shows the cut off characteristics for different membranes. MF membranes have pore size between 100 and 10,000 nm and are capable of removing emulsions of oil, colloidal silica and bacteria.[34, 35] UF membranes have pore sizes between 1 and 10 nm, and are capable of removing viruses and proteins.[34] UF is often used as a pretreatment for NF and RO. NF membranes have pore sizes in the sub-nanometer range (0.1 to 1 nm) and are capable of removing hydrated divalent ions.[36] RO membranes do not have pores, and the separation takes place by the solution diffusion model. RO membranes are capable of retaining monovalent ions, which make them extremely effective for seawater and brackish water desalination. They can reject > 99% of NaCl.[37] Treatment by PV membranes is a combination of

permeation and evaporation, and the separation mechanism is similar to RO (solution diffusion mechanism). PV membranes are used for separating liquid mixtures, such as organic-organic or organic-water mixtures.[38, 39] MD membranes are hydrophobic, and allow water vapor to pass through their large pores, while retaining liquid containing dissolved contaminants on the feed side.[40] The transport of solvents through pores in MF and UF membranes takes place by the pore flow model, where pores are relatively large and stable, and convective transport takes place.[41] RO and PV separation follows the solution diffusion model.[42] In this process, the solvent is selectively dissolved or adsorbed by the membrane material within the free volume of the polymer chains, while the contaminant is rejected. The concentration gradient across the membrane matrix drives the solvent movement, and the solvent is desorbed on the permeate side. Vapor transport across hydrophobic MD membranes is driven by a vapor pressure gradient due to temperature difference maintained between the feed and permeate side.[43] The generated vapor passes through the large MD pores, while the hydrophobic nature of the membrane retains liquid water, which contains dissolved contaminants.

1.3.2 Membrane Distillation

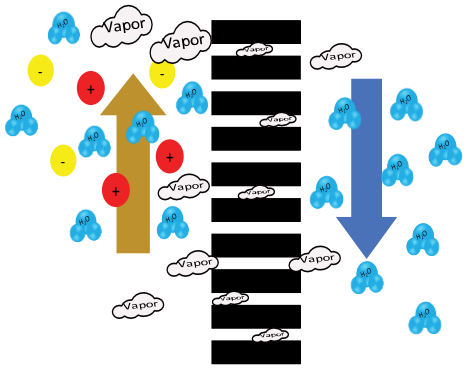

Figure 5: Membrane distillation schematic

MD is a membrane-based separation process, in which a hydrophobic polymeric membrane separates the feed (contaminated) side from the permeate (purified) side (Figure 5). A vapor pressure gradient drives the movement of water vapor and volatile compounds from the feed to the permeate side through the pores of the membrane.[40] Figure 5 depicts a flat sheet direct contact membrane distillation process (where

the feed and permeate streams are both in contact with the membrane). In figure 5, the feed side containing water and foulant molecules (flowing in the direction of the red arrow) is heated (outside the MD module). This thermal energy increases the vapor pressure of water, driving vapor molecules through the (hydrophobic) membrane pores into the permeate stream (flowing in the direction of the blue arrow). Liquid water with dissolved foulants is retained by the membrane on the feed side.[44]

Being a vapor pressure driven process, MD has certain advantages over other membrane-based separation processes that rely on externally applied pressure. For example, MD has no osmotic pressure limitations, and can be used to treat highly contaminated waste streams, resulting in high water recovery.[45] They can also be cost effective, as they are operated at atmospheric pressure, and can achieve high rejection (> 99%).[46, 47]

1.3.2.1 MD Configurations

MD can typically be operated in a number of different configurations. A few of them are discussed below:

a. Direct Contact Membrane Distillation (DCMD)

Here, the hot feed side and the cold permeate side are both in direct contact with the membrane surface.[44] Vapor from the feed side travels through the membrane pores, and condenses on the permeate side, mixing with the cool permeate stream. The temperature of the permeate stream rises as a result if this added vapor, and the permeate stream needs to be cooled to maintain the driving force. This is the most common MD configuration. However, its major drawback is heat loss by conduction through the membrane surface.[17]

b. Air Gap Membrane Distillation (AGMD)

In this mode, the hot feed side is in contact with the membrane surface. On the permeate side, a stagnant film of air separates the membrane from the condensation surface. The vapor crosses the air gap and condenses on the cool surface. A drawback in this configuration is the additional mass transfer resistance introduced by the air gap.[40, 48, 49]

c. Sweeping Gas Membrane Distillation (SGMD)

In this mode, inert gas is used to sweep the vapor on the permeate side, which is then condensed outside the module. This overcomes the mass transfer resistance encountered in AGMD, due to the movement of the gas. It also reduces losses due to heat conduction encountered in DCMD. However, a large condenser is required, as a small volume of vapor is mixed with a large volume of the inert gas.[50, 51]

d. Vacuum Membrane Distillation (VMD)

Here, a vacuum pump is used to create vacuum on the permeate side, and the vapor is condensed outside the module. However, VMD systems have a greater susceptibility to membrane wetting.[52, 53] VMD is most commonly used for the removal of volatiles from aqueous streams.[52]

1.3.2.2 Membrane Properties Governing Effective Separation

a. Liquid Entry Pressure

A membrane's liquid entry pressure is the minimum pressure that drives the liquid to enter the membrane pores, resulting in their wetting. When the transmembrane pressure (pressure difference between the feed and the permeate side) exceeds the liquid entry pressure, the membrane gets wet, allowing liquid (along with dissolved constituents) to enter the pores and mix with the permeate stream.[54] A membrane's liquid entry pressure depends on the pore size and surface properties (hydrophobic nature) of the membrane. It also depends on the feed constituents and concentration.[54]

Liquid entry pressure can be estimated using the following equation:

$$\Delta P = P_f - P_p = \frac{-2B\gamma_l cos\theta}{r_{max}} \qquad \textit{Equation 1}$$

P_f and P_p being the hydraulic pressure on the feed and permeate side; B being the geometric pore coefficient (equal to 1 for cylindrical pores); γ_l being the liquid surface tension, θ being the contact angle, and $r_{\max}$ the maximum pore size.[55]

b. Membrane Thickness

The permeability of a membrane is inversely proportional to its thickness, since a thicker membrane offers greater mass transfer resistance. An optimum thickness would provide the membrane with mechanical stability, while not offering too great a mass transfer limitation. The optimum thickness is between 30-60 µm.[56]

c. Membrane Porosity and Tortuosity.

Membrane porosity is the volume of the pores divided by the total volume of the membrane. Greater porosity results in greater permeability. Porosity can be determined by the Smolder-Franken equation

$$\varepsilon = 1 - \frac{\rho_m}{\rho_{pol}} \qquad \textit{Equation 2}$$

Where ρ_m and ρ_{pol} are the densities of the membrane and polymer material respectively. Membrane porosity usually ranges from 30-85%. The deviation of the pore structure from the cylindrical shape is defined as tortuosity (τ).[57] Membrane permeability is inversely proportional to τ. τ can successfully be correlated to ε using the following equation:

$$\tau = \frac{(2-\varepsilon)^2}{\varepsilon} \qquad \textit{Equation 3}$$

d. Mean Pore Size and Pore Size Distribution

Pore size usually lies between 100 nm and 1 µm, the permeability is directly proportional to pore size. Pore size is used to determine the mechanism of vapor transport across the pore. Since all the pores in a membrane are not uniformly sized, it is important to know the pore size distribution.[58, 59]

1.3.2.3 Transport Mechanisms:

Mass transfer in DCMD occurs by convective and diffusive transport of water vapor. The membrane structure and the air trapped within the pores provide resistance to mass transfer. In this section, we will discuss the equations governing heat and mass transfer in order to better explain temperature polarization

– a phenomenon where the driving force drops due to a temperature gradient formed between the membrane surface and bulk feed.[60-62]

a. Mass Transfer Equations:

The mass flux through the membrane is proportional to the vapor pressure difference

$$J = C_m \Delta P \qquad \textit{Equation 4}$$

Where C_m is the mass transfer coefficient, and ΔP is the vapor pressure gradient across the membrane.

Equation 4 can be written as

$$J = C_m \frac{dP}{dT}(T_{f,m} - T_{p,m}) \qquad \textit{Equation 5}$$

Where, $T_{f,m}$ and $T_{p,m}$ are temperatures at the membrane surface on the feed and permeate side respectively.

According to the Clausius-Clapeyron equation

$$\frac{dP}{dT} = \left[\frac{H_v}{RT^2}\right] P_0(T) \qquad \textit{Equation 6}$$

For more concentrated solutions, the equation was adapted to

$$J = C_m \frac{dP}{dT}[(T_{f,m} - T_{p,m}) - \Delta T_{th}](1 - X_m) \qquad \textit{Equation 7}$$

Where ΔT_{th} is the threshold temperature, given by

$$\Delta T_{th} = \frac{RT^2}{M_w \Delta H_v} \frac{X_{f,m} - X_{p,m}}{1 - X_m} \qquad \textit{Equation 8}$$

Where $X_{f,m}$, $X_{p,m}$ and X_m represent the mole fractions of dissolved species at the membrane surface on the feed side, at the membrane surface on the permeate side and inside the membrane respectively. R and ΔH_v represent the universal gas constant and latent heat of vaporization respectively.

For low concentration solutions, we can assume that vapor pressure is dependent only on temperature (negligible dependence on salt concentration) and use the Antoine's equation.

To incorporate the effect of both temperature and concentration on vapor pressure, the following equation can be used

$$P(T,x) = P_0(T)a_w(T,x) \qquad \textit{Equation 9}$$

Where $a_w(T,x)$ is the water activity as a function of both temperature and concentration, and $P_0(T)$ is the vapor pressure of pure water at a given temperature.

Raoult's law is used to estimate vapor pressure

$$P(T,x) = P_0(T)(1-x) \qquad \textit{Equation 10}$$

Mass transfer through the membrane pores can follow three different mechanisms

i. Knudsen diffusion: This kind of mass transport takes place when the pore size is small. Diffusion is dominated by collisions between the molecules and the pore walls, and collisions of molecules amongst themselves can be neglected.

ii. Molecular diffusion: This kind of movement occurs when molecular movement is driven by the concentration gradient

iii. Viscous flow (Poiseuille flow): This kind of mass transfer occurs when the movement of gas molecules is driven by a pressure gradient

The Knudsen number (Kn) is defined as the ratio of the mean free path (λ) of the molecule to the membrane pore size, and can be used to estimate the dominant mass transfer mechanism within the pore. According to the kinetic theory of gases, the mean free path is defined as

$$\lambda = \frac{k_B T}{\sqrt{2}\pi P d_e^2} \qquad \textit{Equation 11}$$

Where, k_B, T and P are Boltzmann constant, absolute temperature and average pressure respectively.

For Kn>1, Knudsen diffusion dominates, and the molecular transport is dominated by collisions between the molecules and pore walls. Mass transfer coefficient is estimated using the following equation

$$c_{kn} = \frac{2\pi}{3}\frac{1}{RT}\left(\frac{8RT}{\pi M_w}\right)^{\frac{1}{2}}\frac{r^3}{\tau\delta} \qquad \textit{Equation 12}$$

Where, τ, r, δ and M_w are tortuosity, membrane pore radius, membrane thickness and molecular weight of the water vapor respectively.

If Kn < 0.01, molecular diffusion in the air within the pores is the dominant mechanism. In this scenario, the mass transfer coefficient is estimated using the equation

$$c_D = \frac{\pi}{RT}\frac{PD}{P_{air}}\frac{r^2}{\tau\delta} \qquad \textit{Equation 13}$$

Where, P_{air} and P are the air pressure and the total pressure within the membrane pore respectively, and D is the diffusion coefficient. In addition, the flux through membrane pores when molecular diffusion dominates can be estimated using

$$J = \frac{1}{P_{air}}\frac{\varepsilon}{\tau\delta}\frac{DPM_w}{RT}\,\Delta P \qquad \textit{Equation 14}$$

Removing the stagnant air existing inside the pores by degassing the feed and permeate will reduce the molecular diffusion resistance, so the membrane permeability will increase

If the Knudsen number lies between 0.01 and 1, the vapor molecules collide with each other and also diffuse through the air film.in this case, the diffusion coefficient is calculated using equation:

$$c_c = \frac{\pi}{RT}\frac{1}{\tau\delta}\left[\left(\frac{2}{3}\left(\frac{8RT}{\pi M_w}\right)^{\frac{1}{2}}r^3\right)^{-1} + \left(\frac{PD}{P_a}r^2\right)^{-1}\right]^{-1} \qquad \textit{Equation 15}$$

The diffusivity of water vapor in the pores is given by:

$$PD = 1.895 * 10^{-5}T^{2.072} \qquad \textit{Equation 16}$$

The Fuller equation can be used to predict binary gas diffusion:

$$D = 1 * 10^{-7} \frac{T^{1.75}\left(\frac{1}{M_{wa}}+\frac{1}{M_{wb}}\right)^{\frac{1}{2}}}{P\left[(\sum v_a)^{\frac{1}{3}}+(\sum v_b)^{\frac{1}{3}}\right]^2} \qquad \text{Equation 17}$$

Where, $\sum v$ is the diffusion volume, T is the temperature in kelvin and P is the pressure in atmosphere.

b. Heat Transfer Equations

Heat transfer in DCMD occurs in three steps:

Heat transfer by convection in the feed boundary layer:

$$Q_f = h_f(T_f - T_{f,m}) \qquad \text{Equation 18}$$

Heat transfer through the membrane by conduction:

$$Q_m = \frac{k_m}{\delta}\left(T_{f,m} - T_{p,m}\right) + J\Delta H_v \qquad \text{Equation 19}$$

$$Q_m = h_m\left(T_{f,m} - T_{p,m}\right) + J\Delta H_v \qquad \text{Equation 20}$$

Where h_m represents the heat transfer coefficient of the membrane.

Heat transfer by convection in the permeate boundary layer:

$$Q_p = h_p(T_p - T_{p,m}) \qquad \text{Equation 21}$$

At steady state,

$$Q = Q_f = Q_m = Q_p \qquad \text{Equation 22}$$

Therefore,

$$Q = h_f\left(T_f - T_{f,m}\right) = Q_m = h_m\left(T_{f,m} - T_{p,m}\right) + J\Delta H_v = h_p(T_p - T_{p,m}) \qquad \text{Equation 23}$$

$$Q = U(T_f - T_p) \qquad \text{Equation 24}$$

Where U represents the overall heat transfer coefficient.

An important factor in DCMD is the phenomenon of temperature polarization. Thermal gradients developed in the boundary layer lead to a reduced driving force. The temperature at the membrane surface on the feed side is lower than the bulk, and the permeate side temperature is higher than the bulk temperature.[63] Membrane surface temperatures can be estimated using a mathematical iterative model. This results in a loss of driving force, in turn lowering flux.[64, 65]

1.3.2.4 Challenges Faced in MD

a. Membrane Fouling/Scaling and Control Techniques

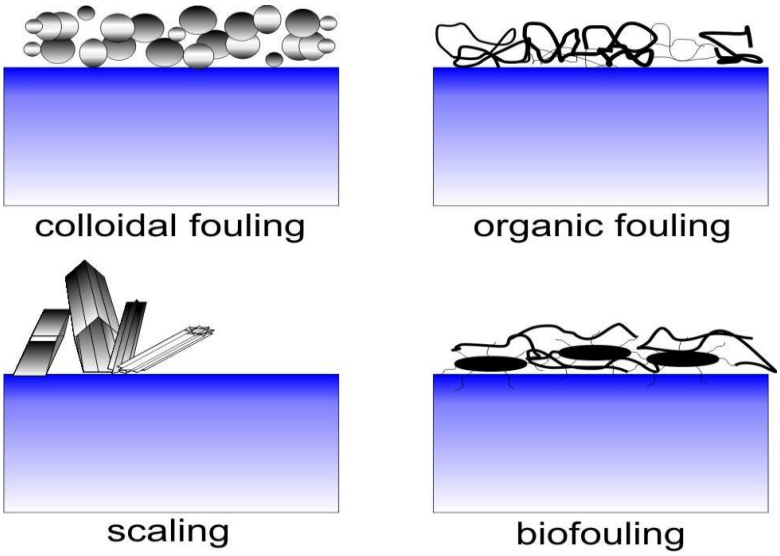

66

Figure 6: Types of membrane fouling

Membrane fouling is a major hindrance to MD operation. Fouling occurs when organic or inorganic contaminants deposit on the membrane surface or within the pores, clog the pores, and block the transport of vapor across the membrane. Once fouled, the flux through the membrane drops significantly, leading to an increase in energy consumption and operating cost. Fouling can also damage the membrane surface, thus shortening its life. Severe fouling may require intensive chemical cleaning or membrane replacement. The factors affecting fouling are operating conditions, membrane properties and the

chemistry of the feed water. There are four kinds of fouling: mineral scaling, organic fouling, colloidal fouling and biofouling (Figure 6).[67-70]

Mineral scaling occurs when ions present in the solution form nuclei, and subsequently crystals, that deposit on the membrane surface or within the pores. This is most often observed in desalination. A region of high salt concentration is formed in the vicinity of the membrane surface (due to depletion of water molecules). This layer of high salt concentration is known as the concentration polarization layer (Figure 7). Concentration polarization is detrimental to all membrane filtration processes. In pressure-driven systems, they can result in osmotic pressure limitations. An increase in solute concentration near the membrane surface increases the osmotic pressure on the feed side, and the applied pressure needs to overcome this osmotic pressure in order to force water through the membrane pores. MD processes, being vapor pressure driven, do not face these osmotic pressure limitations. However, this high salt concentration can lead to super saturated conditions, causing these salts to precipitate and deposit on the membrane surface, leading to scale formation. Scaling can be of two kinds: homogenous and heterogenous. Homogenous crystal growth occurs when nucleation occurs in the solution, and the formed crystal is then deposited on the membrane surface. On the other hand, heterogenous nucleation occurs when nuclei are formed on the membrane surface. Heterogenous nucleation is much more common in membrane systems, because of the existence of the solid/liquid interface, and is much faster than homogenous. In the initial stages of scale formation, amorphous 'pre-nucleation' clusters numbering just a few atoms are thought to be formed, which gradually grow in size and develop crystalline characteristics, before being deposited on the membrane. These pre-nucleation clusters are formed in areas with highest salt concentration, such as at the membrane-water interface. Their formation can be avoided by encouraging mixing within this region, thus preventing co-location of scale forming ions.[71] The rate of scale formation is also affected by the ratio of cations and anions in the concentration polarization layer.[72] Mineral scale formation is typically controlled by adding anti-scalants, modifying solution pH or by encouraging turbulent flow.[71, 73] Anti-scalants are surface-active materials that interrupt

with precipitation reactions in the following ways: (i) Threshold inhibitors act by sorbing on to newly formed crystals and preventing them from growing by blocking active growth sites. (ii) Crystal modification anti-scalants work by distorting crystal shapes, encouraging the formation of soft crystals that do not easily adhere to the membrane surface; and (iii) Dispersion, that causes anti-scalants to adsorb on crystal particles and impart high anionic charge, which prevents these particles from precipitating.[74] Modifying pH in the feed can inhibit scaling by preventing precipitation of compounds that have pH sensitive solubility, such as $CaCO_3$. Turbulent flow causes rapid ion movement and mixing, thus effectively reducing the possibility of their co-location at timescales required for scale formation.

Organic compounds present in wastewater can either be hydrophobic, hydrophilic or transphilic, causing them to attach to membrane surfaces. Organic fouling is poorly understood, as most of the lab studies are conducted with simulated samples using foulants such as bovine serum albumen, humic acid, etc. Several studies show that humic acid found in natural organic matter is primarily responsible for organic fouling. However, another group of studies shows that hydrophilic polysaccharides are the primary reasons for severe organic fouling. Humic acid fouling is much more rapid in the presence of salts such as NaCl. However, humic acid was not found to have penetrated membrane pores. Thus, fouling by humic acid is reversible and does not damage the membrane structure. Elimelech and group have studied organic fouling by a mixture of bovine serum albumen, sodium alginate and humic acid. A strong correlation was observed between organic fouling and molecular adhesion. Strong molecular interactions led to the formation of a cake layer. The study also showed that before the cake layer is formed, fouling is sensitive to intermolecular interactions and hydrodynamic conditions. Pretreatment, high cross-flow velocity, surface modifications and surface cleaning are the principle ways to address organic fouling.[75-77]

Lake, ground and river water, when treated by MD can lead to colloidal or particulate fouling by silica, clay, silt and humic substances. Silica is particularly challenging to remove. Silica can be present in the form of colloidal, particulate or dissolved silica. Larger particles are typically removed by MF and UF pretreatment steps. However, dissolved silica is particularly challenging, as supersaturation conditions can

result in silica polymerization, which results in a gel like layer that is particularly challenging to remove and clogs membrane capillaries. Such conditions are more likely to occur in the presence of divalent cations. Because of this, silica containing feed waters can be particularly challenging to treat.[78, 79] Silica containing water is pretreated, or the membrane is cleaned using a high pH solution.

Biofouling, particularly due to extra polymeric substances (EPS) secreted by bacteria can cause rapid fouling in MD. They are also hard to remove, as they adhere to the membrane surface. They are composed of 75-90% water, and are porous. Thus, apart from pore blocking and wetting, they also lead to diffusion limitations.[76, 78] Biofouling is usually controlled by pretreatment, and adjusting operating conditions such as cross-flow velocity and set-point flux.[80]

Thus, the main strategies to mitigate fouling and scaling are feed pretreatment, membrane surface modifications, and chemical cleaning. Pretreatment can be carried out by filtration, or by adding anti-scalants, flocculants or chemicals.[81]

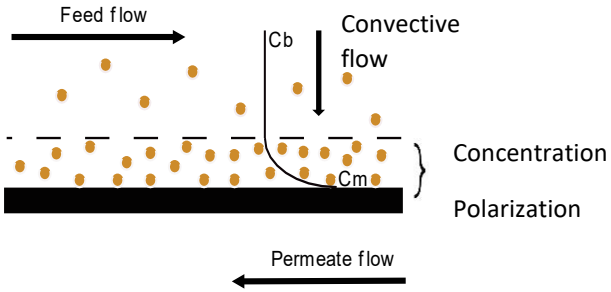

Figure 7: Concentration polarization

b. Membrane Wetting and Control Techniques

In MD processes, water transfer occurs in the form of vapor and not liquid. Sometimes, the deposition of salts or amphiphilic molecules on the surface or in the pores can create a hydrophilic pathway for liquid transfer across the membrane. This phenomenon is known as wetting and can cause a rapid decline in rejection by allowing water containing dissolved contaminants into the permeate stream.[82] Wetting also occurs when transmembrane pressure (the pressure differential between the feed and permeate sides) exceeds the liquid-entry pressure (the minimum transmembrane pressure causing the water in the feed to

enter the membrane pores).[12] membrane wetting can be distinguished into four categories: non wetted, surface wetted, partially wetted and fully wetted. Surface wetting shifts the vapor-liquid interface inwards in the membrane cross section. This causes increase in temperature polarization, resulting in lower permeate flux. In this scenario, there is a possibility of scaling within the membrane pores due to solvent evaporation. However, in some cases, surface wetting or partial wetting has shown to result in an increase in permeate flux due to the shorter pathway for vapor to diffuse into the permeate side. When solution penetrates deeper into membrane pores, partial wetting takes place. In some cases, this decreases the permeate flux due to a reduction in active surface area for mass transport. When full wetting occurs, membrane pores are flooded with solution, resulting in viscous flow of liquid through the pores and no rejection of contaminants.[82] Wetting is avoided by maintaining operating conditions such that the transmembrane pressure does not exceed membrane liquid entry pressure. Omniphobic membranes that show higher wetting resistance are also being developed by modifying surface properties. This is done by ensuring low surface energy chemistry by modifying the membrane with chemicals such as perfluorooctanyl chloride[83], by deposition of nanoparticles[84], or by modifying topographical features by changing the surface texture.

c. Energy Demands

Since the MD process relies on a thermal driving force, the process is considered highly energy intensive due to water's high heat capacity. Compared with other pressure-based membrane separation processes, MD has a high energy demand.[85] The latent heat of vaporization is in the range of 667 kW h m^{-3}.[86] The Gibb's free energy of separation in a RO process is in the range of 0.76 and 1.06 kW h m^{-3}.[87, 88] To make it commercially viable, the energy efficiency of MD process has to be increased.[89] One way of doing this by using waste heat from source water or other treatment processes.

In the following section, we will transition into looking at a class of contaminants of emerging concern that are toxic and recalcitrant, and their typical treatment processes. In this dissertation (Chapters 4 and 5), we modified surface properties to enable sorption of these contaminants to surfaces by tuning the

surface hydrophobic and electric properties. The sorption enabled electron transfer reactions which along with the action of hydrated electrons, synergistically caused contaminant degradation. We also briefly discuss electron-transfer reactions and hydrated electrons.

1.4 Contaminants of Emerging Concern-PFAS

Contaminants that were not previously detected in water samples are known as contaminants of emerging concern (CEC). They are typically manmade chemicals that are persistent, carcinogenic and cause endocrine disrupting or metabolic disorders.[90] Perfluoroalkyl substances (PFAS) are a class of compounds under CEC, which are not well researched, but have been shown to affect the immune system and cause cancer. In PFAS, hydrogen ions in long alkyl chains are replaced by fluoride (F^-). Due to the high electronegativity of F^-, the C-F bond is one of the strongest bonds in organic chemistry. Every additional F^- ion added to a C atom makes these bonds stronger and shorter. The hydrophobic chain is attached to a hydrophilic headgroup, giving these compounds amphiphilic properties that make them excellent for stain resistance and water resistance applications. Due to these properties, PFAS were widely used in water repellent fabric, non-stick cookware, electronics, etc. for over 50 years.[91] Such wide used in consumer goods has led to their elevated concentrations in water sources.[92] They were also used in aqueous fire-fighting foams. The properties that make them so attractive for industrial and commercial applications also make them very hard to degrade and cause bioaccumulation. Due to these reasons, U.S. industries voluntarily began to phase out PFOS production between 2000 and 2002. In 2007, the U.S. EPA restricted the production of PFOS and related compounds.[93] However, due to their persistence, human exposure to PFAS is expected to continue for several years, and appropriate treatment processes are necessary. The current EPA health advisory requires PFOS and PFOA concentration to be less than 70 ng/L.[94] PFAS often co-occur with chlorinated solvents and other ionic species such as Ca^{2+}, Mg^{2+}, K^+, NO_3^-, CO_3^{2-} and SO_4^{2-}.

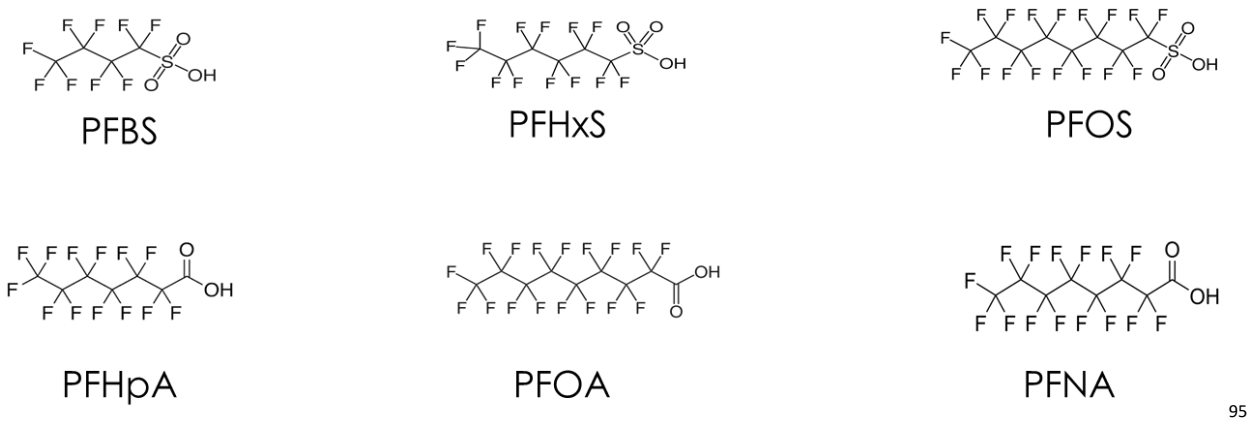

[95]

Figure 8: Major PFAs compounds

Figure 8 shows structures of some of the important linear PFAs found in the environment. Perfluorobutane sulfonate (PFBS) is a four-carbon chain completely fluorinated compound, with a sulfonate head group. Perfluorohexane sulfonate (PFHxS) and perfluorooctane sulfonate (PFOS) are completely fluorinated six and eight carbon compounds with sulfonated head groups respectively. Perfluoroheptanoic acid (PFHpA) is a completely fluorinated six-carbon chain compound with a carboxylic acid head group (contains a total of seven carbons), while perfluorooctanoic acid (PFOA) and perfluorononanoic acid (PFNA) are seven and eight carbon chain compounds (completely fluorinated) with carboxylic head groups. Studies on the sorption properties of PFAs have shown that the longer chain compounds are more likely to sorb that the shorter chain ones. This is due to their superior hydrophobic properties.[96, 97] Hence, shorter chain compounds are typically harder to treat.

1.4.1 Typical Treatment Techniques

The stable and surfactant-like nature of PFAs makes their treatment difficult. They cannot be treated by volatilization. Even thermal, chemical and electrical treatment processes require extreme conditions. Most treatments in practice are ex situ, and the type of treatment process used depends on the kind of PFAs, co-contaminants present and geochemistry. Current methods of PFOS and PFOA removal from wastewater are by adsorption on granular activated carbon or treatment with ion exchange media, and membrane-

based processes (RO and NF). Pretreatment steps such as coagulation, filtration, precipitation and pH adjustment may be required prior to ion exchange treatment. Individual PFAs have different granular activated carbon loading capacities and breakthrough times. While effective, this technique leaves us with a mass of GAC contaminated with PFOA and PFOS which is eventually destroyed by combustion, a highly energy intensive process.[98] Hence, post treatment spent media management is not trivial. RO and NF have also been used for PFAs treatment.[99] in membrane-based processes, effective pretreatment is of utmost importance. A comparative study conducted on two modes of treatment of a mixture of PFAs in a water reclamation plant showed complete removal (below detection limits) of all PFAs in a membrane-based process (NF and RO) coupled with advanced oxidation. On the other hand, a combination of adsorption, filtration and oxidation failed to remove any PFAs shorter than PFNA.[100]

Various novel techniques have been studied for the degradation of PFOA and PFOS. Sonoloysis has been shown to break down the PFOA and PFOS present in groundwater beneath a landfill. Electrochemical degradation of PFOA has been shown to take place at high voltages (above 9 V).[101] Perfluorinated compounds have also been degraded by oxidation with a boron doped diamond electrode.[102] The decomposition of PFOS in subcritical water using zerovalent iron has been carried out successfully.[103] However, the above-mentioned techniques require the addition of other chemicals, fabrication of expensive materials (such as boron doped diamond electrodes), or high energy requirements. This leads to an increase in overall cost.

1.4.2 Defluorination by reduction

The bond dissociation energy is the energy required to break a bond, and form two atomic or molecular fragments.[104] A stable bond has a large bond dissociation energy. Numerous studies have successfully been able to break apart the carbon-halogen bond in organohalogenic compounds by reduction.[105] Gas phase experiments of fluorinated alkyl compounds have shown that C-F bond dissociation occurs in the presence of excess electrons.[106] All this evidence leads to the possibility of a two-electron mechanism that could effectively cause PFAs degradation.

1.4.2.1 Electron-Transfer and Bond Destabilization

Electron transfer reactions are important in organic chemistry as well as electrochemistry. They form the basis of redox reactions. They can be of two types – inner sphere and outer sphere electron transfer. Inner sphere electron transfer usually occurs across covalent bonds and is intramolecular. In outer sphere electron transfer, there is no chemical bond between the donor and acceptor. The electron moves through space from one entity to the other. The driving force is usually a potential difference.[107] Outer sphere electron transfer reactions require the reactants to diffuse together so that they are in close proximity. The electron transfer step then leads to the formation of an activated complex, usually characterized by bond lengthening and the formation of a radical anion.[108] If the potential difference is sufficient, this electron transfer can lead to bond dissociation. However, if there is insufficient energy, the electron transfers back to the donating agent. The energy required for bond cleavage of a radical anion is lowered, and the anion is more susceptible to degradation (Figure 9).[109] This phenomenon of electron transfer can be exploited to lower the energy required to degrade complex PFAs.

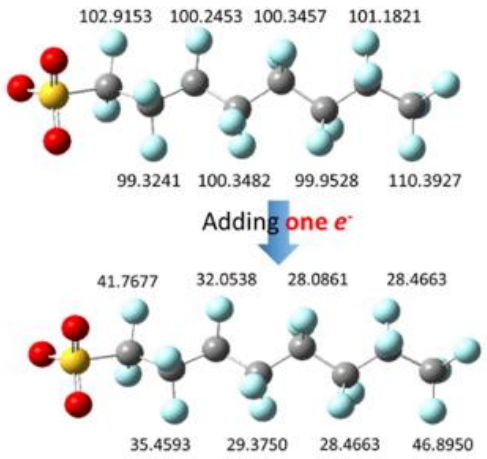

Figure 9: Formation of a radical anion after electron transfer lowers bond dissociation energy

By sorbing a PFAS molecule on to an electrically conductive surface and facilitating electron transfer by an externally applied potential difference, the bond dissociation energy can be lowered, increasing

defluorination rate. The additional energy required can be supplied by another source, such as the hydrated electron.

1.4.2.2 Hydrated Electrons

The hydrated electron is a free electron in a solution, and the smallest possible anion. They can occur in any solvent that mediates outer-sphere electron transfer. In outer sphere electron transfer, the chemical species remain intact before, during and after the electron transfer process. Hydrated electrons are extremely powerful reducing agents (reduction potential of -2.9 V), and can effectively reduce halogenic compounds.[110] They have been successful at degrading PFAs compounds with carboxyl headgroups. However, sulfonated PFAs compounds are particularly hard to degrade, and very low defluorination rates were observed in the presence of hydrated electrons alone. Hydrated electrons can be generated by medium pressure UV photolysis of water. However, they have very short lifespans and are quenched rapidly by competing species present in water, such as protons, hydroxyl radicals and dissolved oxygen. Additives such as sulfide and iodide increase the formation of hydrated electrons.[111, 112] The presence of sulfite and iodide promotes hydrated electron formation. In UV/sulfite and UV/iodide systems, PFOS degradation has been observed at much faster rates.[113, 114] However, adding sulfite or iodide is detrimental to water treatment processes, as it increases costs due to chemical addition as well as possibly requiring further treatment. The lifespan of the hydrated electron in water can potentially be increased by maintaining conditions where the concentration of hydrated electron scavengers is limited. Strategies to achieve this are by increasing the pH (thus limiting proton availability), and degassing the solution (reducing dissolved oxygen concentration).

In the next section, we introduce carbon nanotubes, whose unique properties allow for potential application in membrane anti-fouling as well as photo-electrochemical PFAs degradation.

1.5 Carbon Nanotubes

Carbon nanotubes (CNTs) are graphene sheets seamlessly rolled to form 3D tube like structures. They are exceptional in their strength, thermal conductivity and mechanical and electrical properties. Recent studies have shown that they are able to form porous, electrically conductive films on polymeric membranes, and have promising applications in membrane treatment processes. They have been successful in controlling membrane fouling and scaling. These antifouling and self-cleaning properties are due to electrostatic repulsions, redox reactions and microenvironment pH changes.[72, 115-118] CNTs have exceptional adsorption properties due to their high specific surface area. They are capable of sorbing organic contaminants by Van der Waal interactions.[119, 120] They can also be functionalized to enable sorption by electrostatic interactions. They are of two types: single wall CNTs (SWCNTs) and multi wall CNTs (MWCNTs), depending on the number of sheets rolled around the hollow core (Figure 10).[121] Multiwall carbon nanotubes (MWCNTs) have diameters of the orders of 10 nm and lengths of several microns. They form aggregates and the voids created in these aggregates form pores that are capable of adsorption. Adsorption can occur on the external walls of MWCNTs, inner walls of tubes and within the aggregate.[122]

Due to these unique adsorptive and electrical properties, there is huge potential in developing electroactive membranes for scaling mitigation, as well as developing electrodes that are capable of sorbing PFAs to facilitate electron transfer reactions.

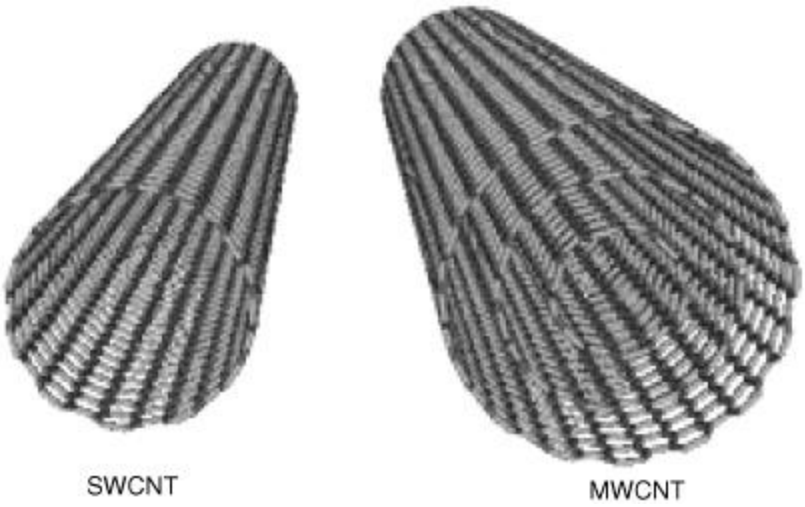

123

Figure 10: SWCNT and MWCNT structures

Carbon nanotubes can be used to synthesize electroactive membranes for fouling and wetting inhibition in membrane processes, as well as the synthesis of specialized electrodes that have favorable surface charge and adsorptive capacity.

1.5.1 Electroactive Membranes

In recent years, CNT based membranes have been fabricated for applications in membrane treatment systems. Electrofiltration has shown tremendous potential, and the fabrication of electroactive membranes has further made their application easier. These electroactive membranes, when used as an electrode in a circuit can reduce energy requirements as well as reducing surface scaling and fouling by causing phenomena such as electrostatic repulsion, electrokinetics, electrophoresis and redox reactions. The superior conductivity also allows for localized heating on the membrane surface, which reduces energy requirements in membrane distillation. A CNT suspension prepared by dispersing fixed concentrations of CNTs in water along with specific surfactants can be coated on polymeric membranes for use in membrane treatment. This is followed by a cross-linking step. In pressure-based systems, the polymeric material coated with CNTs is hydrophilic (such as polysulfone) crosslinked with polyamide, which forms a dense layer capable of rejecting salts. In membrane distillation processes, the polymeric material used is hydrophobic (such as polytetrafluoroethylene), crosslinked with hydrophilic polyvinyl alcohol. Here, the

CNT network is porous, and allows diffusion of water vapor through the pores. These materials have high electrical conductivity, in the range of 1,000-2,000 S/m.

In desalination processes, applying 1.5 V anodic potential to the membrane was successful in electrokinetically reducing $CaSO_4$ scaling. The mechanism was thought to be disruption of the concentration polarization layer due to EDL formation in response to applied potential. Ions in the solution responded to the applied electrical field, and the stoichiometric balance of scale forming ions was disturbed. In the same system, $CaCO_3$ scaling was cleaned by the application of 2.5 V anodic potential. The applied potential resulted in oxidation of water molecules, and a reduction in pH at the surface. Since $CaCO_3$ has a higher solubility at lower pH, this effectively dissolved some of the scale formed.[72] In a MD system, with membrane used as the cathode, the application of 2 V successfully dissolved silica scaling by increasing surface pH and successfully depolymerizing silica scale.[115]

Biofouling was successfully prevented by applying 1.5 V cathodic or anodic potential. Under cathodic conditions, the oxidation of O_2 to H_2O_2 was thought to prevent bacterial attachment to membrane surface. Anodic potential resulted in the oxidation of bacterial proteins.[118] An energy efficient technique for MD was developed, where localized heating was conducted by Joule heating. Joule heating is caused by the application of alternating current to the membrane surface. This technique allowed nearly 100% single-pass recovery, and dramatically reduced costs.[124]

1.5.2 CNT-based electrodes

Over the last decade, there have been significant advances in CNT based electrochemical sensors. This has been motivated by the superior electron transfer properties from the CNT electrode area to enzymes, high surface to volume ratios, and ability to be functionalized, which helps in attaching any chemical species.[125] They are usually fabricated by casting CNTs on to a glassy carbon electrode. The same properties that allow CNTs to be used as biosensing electrodes can find potential application in degradation of PFAs. Electrodes can be prepared by dispersing CNTs in a solution using a surfactant, and

depositing this dispersion on a substrate. The surfactant used will also influence the electrode sorption properties.

1.6 Research Objectives

The overall objective of this dissertation was to influence electrostatic and hydrophobic interactions between contaminants, water and the separating medium (CNT or polymeric membrane material) in order to achieve effective separation, scaling resistance, or contaminant degradation.

Chapter 2 looks at the treatment of wastewater from dairy farms using hydrophobic polymeric membrane distillation membranes. The wastewater is first treated by hydrothermal liquefaction (HTL), where organic carbon is converted into biocrude oil. HTL effluent is hot, and this waste heat can be used to drive the MD process. Effluent contains high concentrations of nutrients and volatile compounds and was treated in a MD system. The retentate and permeate streams were analyzed for nutrient concentration, carbon content and volatile organic content. While MD was effective at separating salts and inorganic compounds containing nitrogen and phosphorus, the hydrophobic membrane allowed volatile organic compounds to pass through. This treatment process demonstrates that a MD membrane can effectively separate compounds based on their volatility. Using waste heat from the HTL process can potentially make MD more economical.

Chapter 3 reported a unique method for scaling mitigation in desalination of brackish water by membrane distillation. High salinity brines, such as those generated by wastewater from oil and gas extraction and geothermal brines (which contain waste heat after being used for power generation) can have total dissolved solid (TDS) concentrations as high as 245000 mg/L.[126] when waste heat is available (as in geothermal brines), the MD process can be economical. However, due to high salinity, scaling is a major hindrance. Electrically conducting membrane distillation (ECMD) membranes were fabricated and used to mitigate scaling. Membrane scaling was studied under different applied potentials and frequencies, and silicate and calcium sulfate scaling was reduced to a large extent by the application of 2 V alternating

current of 1 Hz frequency. Electrochemical measurements were conducted to propose a mechanism for this anti-scaling phenomenon. This method of treating high salinity water could reduce or eliminate pretreatment requirements.

Chapter 4 presented a novel mechanism for the degradation of perfluorooctane sulfonic acid (PFOS), where a CNT coated membrane-electrode was used as the cathode in an electrochemical cell. This membrane-electrode was prepared using different surfactants to show the impact of surfactant and surface charge on the sorption of PFOS. PFOS sorbs onto the membrane-electrode by a combination of electrostatic and hydrophobic forces. An external applied potential weakens the C-F bond in PFOS, making it easier to breakdown. UV irradiation in the liquid phase leads to the formation of hydrated electrons which are capable of breaking down these weakened C-F bonds. The impact of various reaction conditions and applied potential on the defluorination rate of PFOS was studied.

Chapter 5 is an extension of the study conducted in chapter 4, where the two-electron degradation mechanism is tested on linear PFAs having different chain lengths and headgroups. The effect of mixtures of PFAs on defluorination rate was studied. We studied degradation of isotopically labeled and unlabeled PFOS and by the observed difference in degradation rate, confirmed the two-electron mechanism. We also looked at the dechlorination rate of chlorinated solvents. In general, longer chain compounds were more easily sorbed to the electrode due to their higher hydrophobic nature. This enabled their breakdown to be easier. Carboxylated PFAs were broken down more easily than sulfonated PFAs. We observed dechlorination primarily by hydroxyl ions generated by UV photolysis of water.

In chapter 6, we concluded the main results and discussed future research directions.

Chapter 2: Coupling Hydrothermal Liquefaction and Membrane Distillation to Treat Anaerobic Digestate from Food and Dairy Farm Waste

Abstract

Increased demand for water, energy and food requires new ways to produce fertilizers, fuels and reusable water. Recovery of resources farm wastes could lead to an additional source of energy and nutrients, and also reduce the waste to be disposed. In this work, we used hydrothermal liquefaction to produce a biocrude oil product, followed by membrane distillation of the aqueous effluents to concentrate a nutrient-rich stream that can be used as fertilizer. The motivation for this work is that residual heat from the hydrothermal liquefaction process could be utilized to drive the membrane distillation process, which would improve the efficiency and reduce the cost of the distillation process. The membrane distillation system was demonstrated to be able to recover 75% of the water. The membrane distillation retentate had very high ammonium and phosphate concentrations, making it suitable as a fertilizer. Membrane permeate contained high concentrations of volatile organics.

2.1 Introduction

Fertilizers have played a critical role in the development of agriculture by substantially improving crop yields, and their importance is growing as the population increases. Commercial fertilizers are composed primarily of nitrogen, phosphorous and potassium, with several also containing some organic species [127]. Fertilizer production is an energy intensive process, accounting for approximately a third of the energy consumption during US crop production [6].The main source of phosphorous is phosphate rock, which is mined in several locations around the globe (primarily in Morocco, China and South Africa [128]). During the fertilizer manufacturing process, phosphate rock is converted to various forms of soluble orthophosphates [129]. However, natural phosphate rock deposits are dwindling, which could have dramatic impacts on global agricultural yields [130]. Nitrogen in fertilizers is generated through the Haber-Bosch process, where atmospheric nitrogen is converted to ammonia in a process that requires hydrogen which is usually generated from steam reforming of methane [131, 132]. Given the high energy costs, and dwindling precursor materials, an attractive alternative to current fertilizer production methods is the recovery of nitrogen and phosphorous species from various waste streams [5, 133, 134]. Various resource-recovery methods have been explored, with many investigations reporting the extraction and recovery of nitrogen and phosphorous from waste such as municipal and industrial wastewater, manure lagoons, and landfill leachate [135, 136].

Due to its high reliance on dairy as a food source, the United States has a large number of dairy farms; a 2014 USDA report states that there were over 9.2 million milking cows, with this number growing steadily [137]. Each cow produces 20 to 30 tons of liquid manure every year, which translates into the production of 180 to 200 million cubic meters of manure per year. Liquid manure is rich in organic carbon, and nutrients such as nitrogen, phosphorous and potassium [138]. A common treatment strategy for this waste is anaerobic digestion, which converts approximately 50% of the biomass into biogas that is used as a source of heat and electricity [139]. Liquid effluent from anaerobic digestion (known as digestate) contains large amounts of organics and nutrients. Traditionally, anaerobic digestate is disposed of in

landfills or sent to a wastewater treatment plant [140, 141]. In addition to wasting valuable resources, this practice can result in soil and groundwater pollution, due to leaching [142]. Digestate may also be directly applied to agricultural land as fertilizer. Direct spreading of digestate on land is not recommended during winter, however, as excess precipitation can cause it to run off the land and contaminate local water sources. This need for seasonal application results in large storage requirements [143]. Further, since dairies tend to be clustered, this leads to the clustering of biogas plants and the oversupply of digestate in certain regions [144]. Thus, the digestate either needs to be transported to remote agricultural land that is nutrient deficient, or processed in a different way. Since digestate is 95% water, the transportation of this liquid product is economically and logistically complicated. Many biogas plants separate the solid and liquid fractions of digestate and then use the solid fraction as fertilizer, with the liquid fraction requiring further treatment [144]. This practice leaves two concentrated streams containing organic carbon and nutrients. However, crops do not require such large amounts of organic carbon to be provided through soil. Thus, a better utilization of the carbonaceous fraction found in digestate would be to valorize this carbon into a useful form of fuel, and in addition, recover the nutrients in a concentrated form that can be readily transported.

One way to achieve both these goals along with producing a stream of treatable water is by the integration of two energy efficient processes; hydrothermal liquefaction (HTL) and membrane distillation (MD). A brief description of both these processes follows.

HTL is an attractive technology for the production of energy products and bio-based chemicals from high-water-content biomass [145]. The main advantage of HTL is the use of water as the reaction media. This is in contrast to conventional dry thermochemical processes (i.e., pyrolysis or gasification) where water has to be removed prior to the process [146]. Therefore, HTL offers opportunities for valorization of wet-waste streams, such as food waste and manure [147, 148]. HTL typically takes place over a range of temperature (280–380º C), pressure (7–30 MPa) and reaction time (10–60 min) conditions [146]. These conditions allow the production of bio-crude oil (liquid) and hydro-char (solid) products along with some

biogas, all with higher heating values than the raw feedstock [149]. HTL has been tested with a variety of biomass feedstocks, particularly in regard to the bio-crude oil and hydro-char products [150-154]. In addition, the HTL process also produces a significant amount of an aqueous-phase product, traditionally considered a waste. One possibility of valorizing the HTL aqueous effluents is by considering it as a secondary feedstock for bioenergy production via anaerobic digestion and gasification processes [8, 155-157]. Since the HTL aqueous effluents have resulted from a thermochemical process, they are sterile and hot, and therefore may be a feasible feed for MD processes. In this configuration, the residual heat present in the HTL aqueous effluent is used to drive the MD process, which uses thermal energy to separate volatiles (water, volatile organics) from non-volatiles (nutrients) [40].

MD is a membrane-based water treatment method that uses a vapor-pressure gradient across a hydrophobic membrane as the driving force for the transport of water vapor (and other volatiles) across the membrane, while preventing liquid water (which contains the contaminants) from passing through the membrane [40, 47]. In MD, the vapor-pressure gradient is induced by a temperature gradient between the feed stream and the permeate stream, which are separated by the membrane itself. Because the process blocks liquid water from passing through the membrane, and because the driving force is not a pressure differential, MD is typically used for treating highly contaminated waste streams with low concentrations of volatile species [45]. Membrane distillation faces several challenges such as membrane fouling, wetting, high energy requirements and the inability to separate volatile compounds [43, 45]. Fouling occurs when organic and inorganic materials in the feed deposit on the membrane surface, partially or completely blocking the passage of water vapor, which causes a decrease in the permeate flux [117, 158]. Because MD relies on the prevention of liquid water from passing through the membrane, it is essential that the membrane is not wetted (i.e., allow the passage of liquid water through the pores) [55, 60]. Thus, operating conditions in the MD module have to be maintained such that transmembrane pressure does not exceed the liquid-entry pressure, defined as the minimum transmembrane pressure causing the water in the feed to enter the membrane pores [68]. However, membrane wetting can also occur as a result of the deposition

and accumulation of organic and inorganic species within the membrane's pores [54]. For example, amphiphilic organic molecules can sorb onto the hydrophobic pores of the membranes, which creates a hydrophilic surface that can be readily accessed by contaminated liquid water [54]. Once the membrane is wetted and contaminated liquid water passes into the permeate, the performance of the membrane rapidly plummets [68]. Since the MD process relies on a thermal driving force, the process is considered highly energy intensive due to water's high heat capacity [47]. Thus, for MD to be economically feasible, it needs to be applied to either high-salinity brines or a waste (i.e., free) heat source needs to be available [40].

Here, we report on the performance of an integrated energy-efficient process, which aims to convert the organic carbon contained in anaerobic digestate into bio-crude oil, while concentrating nutrients to produce a high-strength fertilizer and generating a stream of water that can be readily disposed. The integrated approach is based on a two-step process, where first the digestate is processed using hydrothermal liquefaction (HTL) to produce valuable hydrocarbons, and then the aqueous effluent from the HTL process is treated using membrane distillation (MD) to concentrate nutrients (nitrogen and phosphorous) and produce a high-quality fertilizer. While the motivation for this work is the potential use of residual waste heat from the HTL process to drive MD, in this work, we did not use residual heat, instead using traditional heating methods to provide the driving force for separation.

The integrated approach described in this paper is based on a two-step process, where first the digestate is processed using hydrothermal liquefaction (HTL) to produce valuable hydrocarbons (energy), and then the aqueous effluent from the HTL process is treated using membrane distillation (MD) produce two streams: (1) a concentrate nutrient stream (nitrogen and phosphorous) that can be used as high quality fertilizer, and (2)a stream of water devoid of organic matter and nutrients (ideally) In this paper, we focus on the performance of the MD part of the system. Heated HTL aqueous effluent is used as a feed stream for MD, with vapor from the feed passing through a hydrophobic membrane, while nutrients and organic carbon are retained on the feed side. This process integration produces two distinct streams: a retentate stream rich in organics and nutrients, and a permeate stream of water containing any residual volatile

organic compounds (VOCs) found in the HTL aqueous effluent. MD performance was followed in terms of flux and wetting, while all system streams (feed, permeate and retentate) were extensively characterized in terms of water quality characteristics, with a particular emphasis on the concentration and speciation of nutrients and carbon. HTL effluent derived from food waste and dairy manure was used as the feed for the MD process, and we investigated how these two feedstocks impact membrane performance and the water quality of feed and two membrane product streams. Because the aqueous HTL product streams contain large amounts of volatile organic compounds (VOCs), we expect a fraction of the VOCs present in the feed to pass through to the permeate [8]. To characterize the VOCs within each stream, volatiles were collected and then analyzed by two-dimensional gas chromatography with detection by time-of-flight mass spectrometry (GC×GC-TOFMS system). While the motivation for this work is the potential use of residual waste heat from the HTL process to drive MD, in this work, we did not use residual heat, instead using traditional heating methods to provide the driving force for separation.

2.2 Materials and Methods

2.2.1 Hydrothermal Liquefaction and Phase Separation

The HTL batch reactor used in this study has been previously described in detail [152]. Briefly, a 500 mL stainless steel vessel (Model 4575 Parr Instruments Co., Moline, IL) was loaded with 200 mL of biomass and water mixture. Carbohydrate-rich food waste (herein referred to as 'food waste') and anaerobically digested cattle manure (herein referred to as 'manure') were used as biomass feedstocks. Food waste was collected from Cornell University dining halls (Ithaca, NY) and characterized in the lab (fruits 15 wt%, vegetables, 47 wt%, grains and breads, 38 wt%). Digested cattle manure was taken from an anaerobic digester located on a dairy farm (Sunnyside farm, Scipio Center, NY). The food waste and manure had average solids contents of 10 and 8 wt%, respectively. The initial solids concentrations loaded to the reactor for all experiments were 5 wt% for food waste and 4 wt% for manure, using Milli-Q water as reaction medium. Some pretreatment was required to ensure that the feed was well mixed and with

relatively small particle sizes. After loading the feed mixture, the HTL reactor was closed and the system was purged with nitrogen and pressurized to an initial pressure of 2.5 MPa. The reaction mixture was stirred (100 rpm) using a magnetic agitator. The temperature was set to 300 °C and the reaction time was set to 60 min. The reaction period started when the temperature reached 80º C, followed by a heating ramp (from 80 to 300 °C) of approximately 20 min and was completed after an additional 40 min of heating at 300 °C, when the product was collected.

The liquid product from the reactor was collected through a tube-in-tube heat exchanger connected to the reactor's outlet to rapidly quench the liquid effluent and to avoid the cooling ramp. After collecting the liquid product, the heater was turned off and the reactor was cooled down, following cleaning and removal of any solid residue. Phase separation was conducted using a multi-stage procedure: 1) gravimetric filtration using a Whatman #1 filter paper to separate the solids; 2) separation of the polar and non-polar liquids using solid-phase extraction (SPE) tubes (Sigma Aldrich, St. Louis, MO); and 3) filtration of the aqueous phase via 0.45 µm membrane filter.

Based on preliminary results, the amount of energy that can be obtained from the heated HTL effluent with a reaction temperature of 300^0C is 1229.1KJ/kg. Assuming the heat capacity of water, that results in a ΔT of 293K. This is more than sufficient to carry out membrane distillation process.

2.2.2 Membrane Distillation System Design and Procedure

A flat sheet flow cell setup was used in this study, where the flow cell was made out of nylon 66 (McMaster-Carr). Channel dimensions were 8 cm × 5 cm, with a channel height of 4 mm. The feed and permeate channels were identical. Teflon tubing was used for all process streams. In our setup, the feed was heated by an external source because HTL was carried out at a different location (Cornell University, Ithaca, NY). The feed reservoir was immersed in a bath of silicon oil and heated using an immersion heater. A proportional-integral-derivative (PID) controller maintained the feed inlet temperature at a steady value. Gear pumps (Cole Palmer) were used on the feed and permeate side. A hydrophobic

polypropylene membrane (3M; with a pore diameter of 0.59 µm and a thickness: 110 µm) was used for separation. The weight of the permeate tank was continuously measured using a precision balance (Scientific Industries). The system was designed using open-source hardware (Arduino) and open-source software (Python) [159].

A 300 mL glass jar was used as the feed reservoir. Three holes were drilled through the cap to allow for the inlet, outlet and temperature probe, with 250 mL of HTL effluent measured into the jar. After the sample reached the desired temperature (60º C), the pumps were started with flow rates of 1 L/min, resulting in a crossflow velocity of 8 cm/s. The feed solution was continuously passed through the flow cell and allowed to concentrate and reduce in volume, as vapor from the feed passed into the permeate stream through the membrane. A 2-L glass bottle was used as the permeate reservoir with two holes drilled through its cap for inlet and outlet. The reservoir was initially filled with 600 mL of deionized water (DIW). This was flowed through the permeate side of the flow cell, collecting vapor from the feed side, causing the permeate reservoir to increase in volume. The permeate stream was cooled using two miniature fan cooled heat sinks (McMaster-Carr) to maintain permeate side temperature at 21º C. The experiment was continued for approximately 2.5 hr, until the feed volume reached 62 mL, corresponding to 75% water recovery, and the permeate volume reached 788 mL. 10 mL of permeate was extracted in 30 min intervals to monitor the conductivity and chemical oxygen demand (COD) of the liquid. A new membrane was used for each experimental run.

2.2.3 Fouling Experimental Procedure

Fouling was evaluated by monitoring changes in membrane flux, which was measured by continuously recording the weight of the permeate tank. MD runs were conducted using consistent hydrodynamic conditions, temperature gradients, and membrane materials to ensure that only the feed content impacted membrane fouling [160]. Scanning Electron Microscope (SEM) images and Energy Dispersive Spectroscopy (EDAX)/X-ray photoelectron spectroscopy (XPS) analyses were carried out to further study membrane fouling.

2.2.4 Membrane Wetting Evaluation

The conductivity and COD of the permeate were measured every 30 min. To determine whether membrane wetting occurred as a result of the treatment of the HTL effluent, the feed solution was switched to a 1 M NaCl solution, and the permeate conductivity was monitored for 30 min, with measurements taken every 5 min. It was expected that if membrane wetting did occur, Na^+ and Cl^- ions would pass through the membrane, which would dramatically increase the conductivity of the permeate.

2.2.5 Volatiles Analysis

To characterize the VOCs within each sample stream (feed, permeate and retentate), a custom-built purge-and-trap apparatus was used (Figure 11). N_2 gas was bubbled through 1 mL of sample in a round bottom flask for 30 min at a flow rate of 14 mL/min. An additional dry purge flow of 36 mL/min was mixed with the purge flow to reduce the humidity of the gas sample. The purged VOCs were trapped on a dual-bed sorbent tube containing Tenax TA and Carbograph 1 (Camsco, Houston, TX). Background samples were collected to eliminate any compounds present in the setup. Each sample was collected and run in duplicate. However, one sample of manure-retentate was lost due to technical difficulties during analysis. Flasks were cleaned thoroughly with DIW and methanol and then baked at ~140 °C between sample collections. The sorbent-tube samples were thermally desorbed at 300º C using a TurboMatrix 650 automated thermal desorber (ATD, Perkin Elmer, Waltham, MA). Internal standards (1,2-dichlorobenzene-d4 and 1-bromo-4-fluorobenzene) were added to each tube immediately prior to analysis. A fraction (4.6 %) of the desorbed material was injected into a two-dimensional gas chromatograph with detection by time-of-flight mass spectrometry (GC×GC-TOFMS, Pegasus 4D, Leco Corp., St. Joseph, MI). The column set included a DB-VRX primary column (30 m, 0.25 mm ID, 1.4 µm film, Agilent Technologies, Santa Clara, CA) and Stabilwax secondary column (1.5 m, 0.25 mm ID, 0.5 µm film, Restek Corp., Bellefonte, PA). The primary oven was held at 40º C for 6 min, followed by a ramp at 4º C/min to 210º C with a final hold of 5 min. The secondary oven temperature was offset +15º C

relative to the primary oven and the modulator temperature was +20º C relative to the secondary oven. The modulation period was 5s. The column flow rate was 1.3 mL/min with helium carrier gas. GC×GC-TOFMS data were processed using GasPedal (Decodon GmbH, Greifswald, Germany), an image-based GC×GC data analysis package [161]. Tentative compound identifications were determined, where possible, based on NIST mass spectral library matches and retention behavior. The abundance of each observed peak within a given sample was normalized by the sum of the peak abundances for the two internal standards to account for any run-to-run variability. The mean and standard deviation for each analyte were then determined for each set of duplicate samples.

2.2.6 Nutrients Analysis Procedure

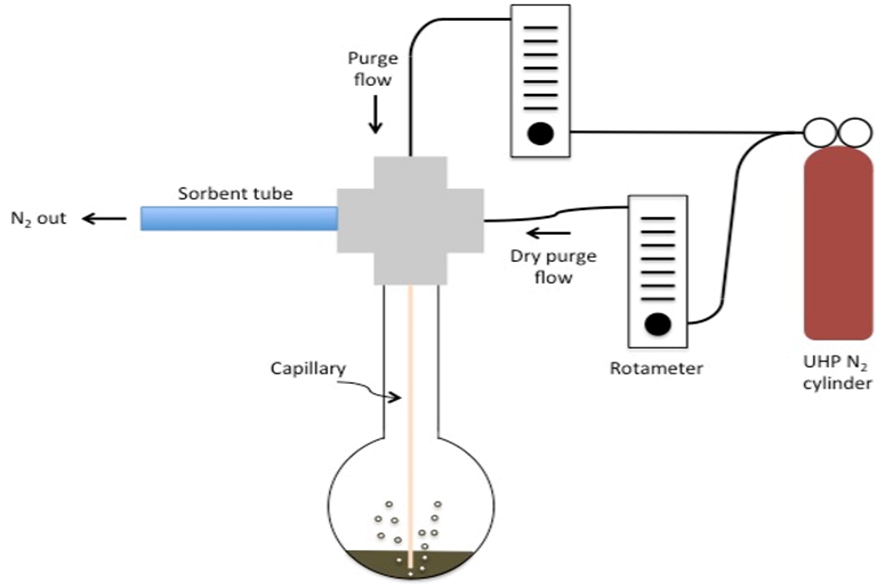

Figure 11: Experimental set-up of volatile organic compounds analysis

COD, VOCs, and different forms of nitrogen and phosphorus were measured in every stream of the process. Mass-balance calculations were performed to determine the presence and form of these nutrients in each stream. Samples were diluted with DIW to fit in the appropriate measurement ranges. Nitrate was tested using the NitraVer X Nitrogen-Nitrate Reagent Set, HR (Hach, Loveland, CO), which is capable of detecting nitrate in the range 0.2–30 mg N/L. Ammonium was measured using the HACH TNT 831

testing kit, which can measure ammonium in the range 1–12 mg N/L. HACH TNT 845 was used for testing orthophosphate and total phosphorous in the range of 6–60 mg P/L. COD was measured using the high-range COD kit from HACH which is capable of measuring in the range of 3–150 mg/L. Total nitrogen (TN) measurements were done using the Total bound Nitrogen (TNb) module of the Aurora 1030C Combustion Total Organic Carbon (TOC) analyzer.

2.3 Results and Discussions

2.3.1 Membrane Distillation Performance

HTL effluent (either from food waste or manure, maintained at 60º C) was used as feed for the MD system, with the MD process operating in a cross-flow configuration. In these experiments, MD permeate was not returned to the feed tank, and the feed was allowed to concentrate with time. For both feedstocks, the initial flux was approximately 20 Liters/m^2 hr (LMH) (Figure 12). When food-waste-derived HTL effluent was used in the MD system, the flux was relatively stable (with mild fluctuations) until water recovery reached 60% (Figure 12a), at which point flux dropped by 40%, stabilizing at an average of 12 LMH for the duration of the experiment (until water recovery reached 75%). When manure-derived feed was treated by the MD system, membrane flux experienced a slow decline (from 19 to 17 LMH) until recovery reached approximately 40%, at which point flux dropped at a faster rate, reaching a value of 12 LMH when recovery reached 75% (Figure 12b). The decline in membrane flux can be attributed to membrane fouling, mainly by organic compounds and minerals. As the feed becomes more concentrated, due to continuing water recovery, membrane fouling becomes more pronounced; this is caused by accelerated deposition of foulants, such as organic molecules and particulate matter onto the membrane surface, which blocks the flow of water [69, 115, 162]. Considering that the fouling behavior of the MD membrane was similar when treating food waste or manure derived HTL effluent, we speculate that there was no significant difference between fouling species present in these effluents. This is also supported by SEM images (figure 13) which show similar fouling constituents (organic fouling and some mineral

scaling). XPS results show that C, O and N are the main fouling agents. Although the flux declined as water recovery increased, it never dropped to levels that were unsustainably low, indicating that MD is a viable method to treat HTL effluent, likely not requiring excessively large membrane areas to compensate for very low fluxes.

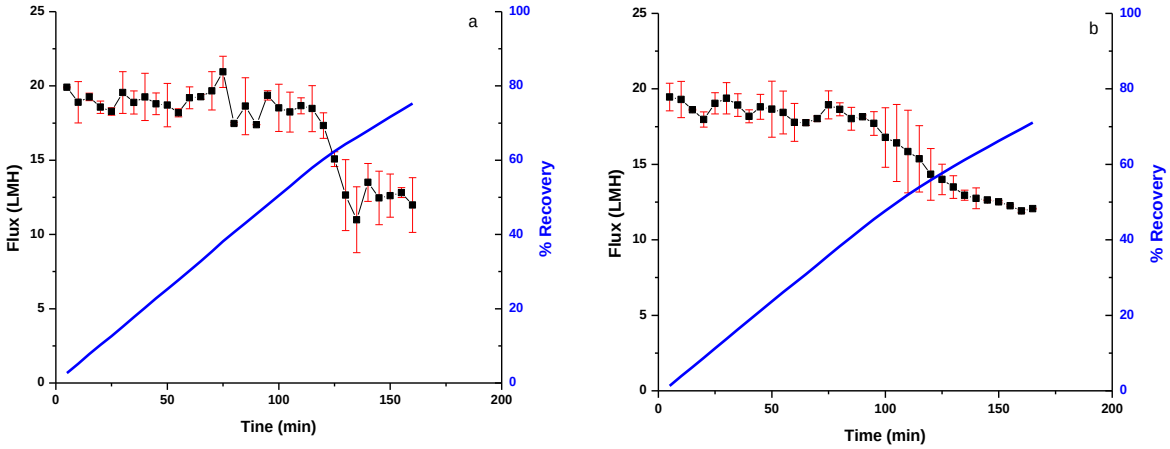

Figure 12: Membrane flux (in black) and water recovery (in blue) of MD system treating HTL effluents derived from (a) food waste, and (b) manure. Values represent the average two replicates ± 95% confidence intervals.

2.3.2 Membrane Wetting Results

A critical aspect of MD performance is whether the membrane becomes wetted by dissolved species from the feed stream, leading to catastrophic failure of the separation process. Membrane wetting can result in the transport of non-volatile species into the permeate stream, and defeats the purpose of the MD process, which is designed to allow the passage of volatile compounds (ideally, only water). Membrane wetting was evaluated by measuring the conductivity and COD concentrations in the permeate for both food waste and manure feed HTL effluent (Figure 14). An increase in conductivity or COD in the permeate

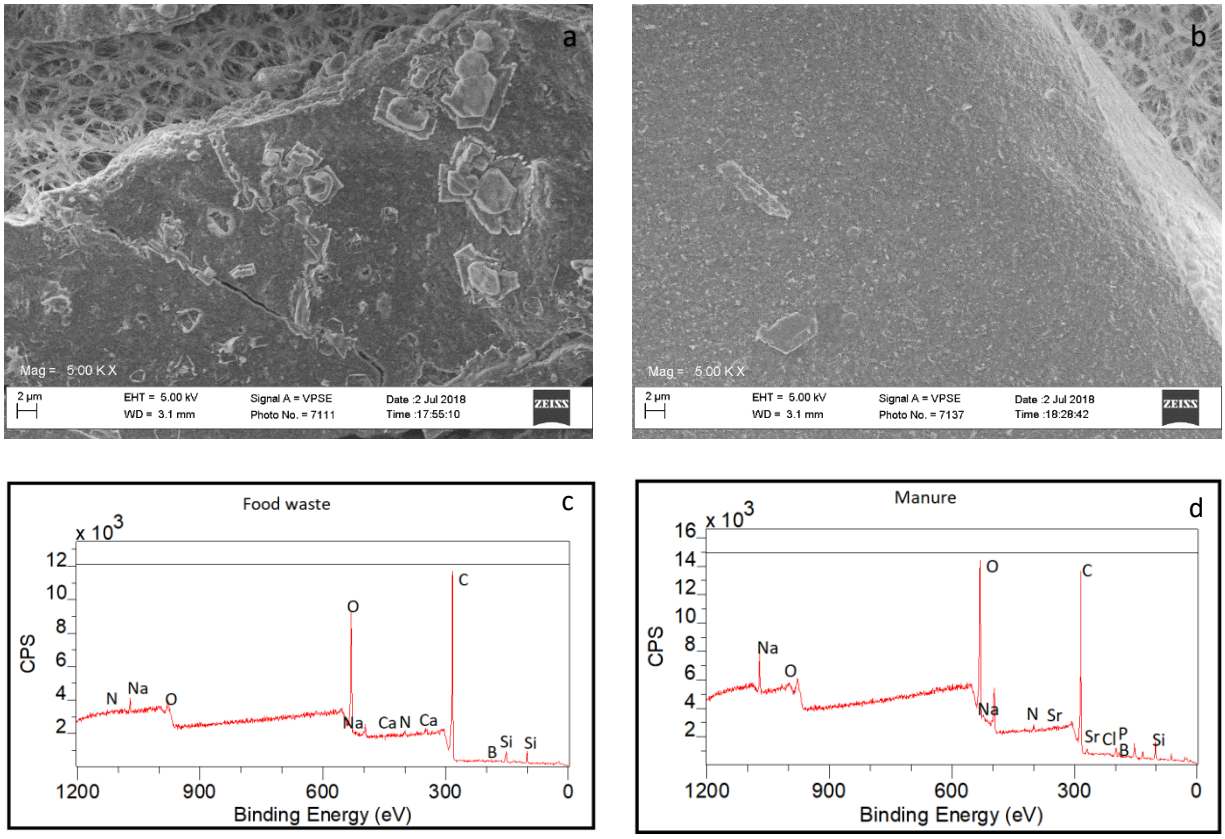

Figure 13: SEM and XPS results of fouled membrane with food waste (a and c) and manure (b and d)

could be caused by membrane wetting or by volatile compounds being transferred across the membrane. Both conductivity and COD levels increased over time in the MD permeate when treating food waste-derived HTL effluent (Figure 14a). Conductivity reached a level of 18 µS/cm after 165 min (75%

recovery), while COD concentrations reached a level of 148 ppm at the end of the experiment. For the manure-derived HTL effluent (Figure 14b), conductivity increased linearly, with an endpoint of 63 μS/cm; COD also increased steadily, reaching 1,042 ppm at the end of the experiment (160 min), at which point water recovery was 75%. Interestingly, the conductivity and COD concentrations behaved similarly, indicating that conductivity potentially increased as a result of VOCs passing through the membrane into the permeate, rather than non-volatile salt species (which would indicate membrane wetting).

Given the elevated COD and conductivity measurements in the permeate, an additional test was performed to verify whether membrane wetting did indeed occur. In this test, the feed stream was switched to a 1 M NaCl solution after the sample processing run (treating manure-derived HTL effluent) using the same membrane; if the membrane was indeed wetted by species in the HTL effluent, then it would be expected that Na^+ and Cl^- ions would readily pass through the membrane and dramatically increase the permeate conductivity. In this case, NaCl solution would pass through the membrane pores which would increase the permeate conductivity. However, no increase in the conductivity of the permeate was observed over 30 minutes, indicating that membrane wetting did not occur. Thus, the observed increase in the conductivity of the permeate streams from HTL effluents being treated by MD can be attributed to VOCs passing through the membrane, and not to membrane wetting; some of these volatiles, such as organic acids, can contribute to the increase in conductivity. Critically, the increase in conductivity, while measurable, was very small (<70 μS/cm) indicating that relatively few ionic species crossed the membrane. For reference, the conductivity of drinking water ranges between 50–500 μS/cm. These results demonstrate that MD using a polypropylene membrane is a feasible treatment method for HTL effluent, as these membranes are resistant to wetting (up to 75% water recovery in our experiments).

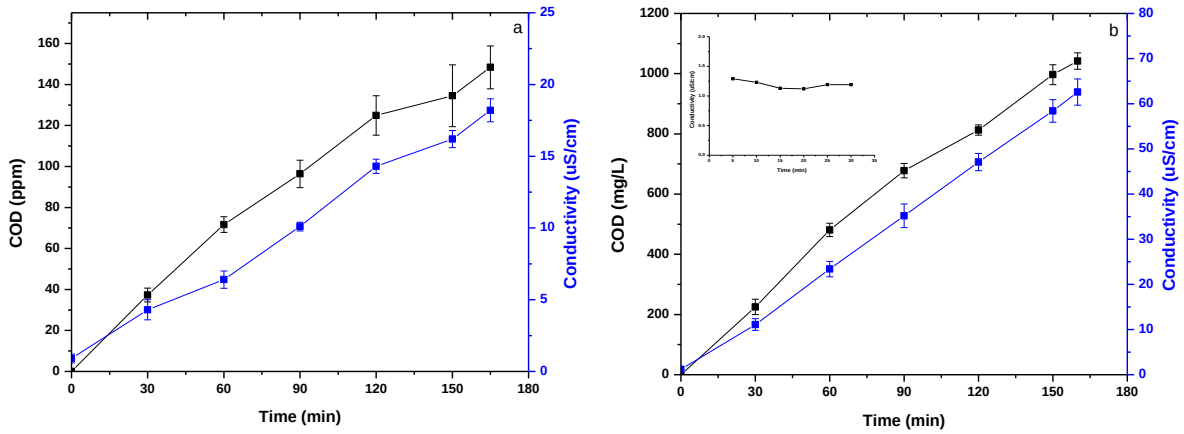

Figure 12: COD (in black) and conductivity (in blue) of MD permeate over time when treating HTL effluent generated from (a) food waste and (b) manure. Values represent an average of two replicates ± 95% confidence intervals. Inset: Permeate conductivity with 1 M NaCl solution used as feed, following the manure experiment

2.3.3 Analysis of Volatile Compounds in the Three Process Streams

High concentrations of organics were measured in the MD permeate; therefore, a detailed compositional analysis was performed on feed, retentate, and permeate samples using GC×GC-TOF-MS. A total of 103 compounds were identified in these streams (Table 1), which accounted for 96% of the total normalized abundance. We limit our focus to the top 10 compounds based on the peak-normalized volume detected in the feed samples, which account for 55% and 70% of the total species in the food waste and manure HTL effluents, respectively (Figure 15). The results from running DIW water through the MD system showed negligible volatile content; these samples were averaged along with purge-and-trap samples to determine background. The background-normalized volume was subtracted from the samples before plotting them.

Because the HTL effluent, retentate and permeate samples spanned such a wide range of concentrations, accurate quantitative measurements could not be made for these compounds; specifically, the most abundant compounds in the HTL effluent and retentate streams exceeded the linear range of the instrument and thus their relative abundances should be considered as lower limits. Figure 15 shows the relative concentration of the top 10 compounds in each stream.

A major portion of the volatiles detected were aldehydes and ketones, with butanone, acetone, cyclopentanone and 2-Methyl-2-cyclopenten-1-one being the most abundant ketones detected. Butanone previously has been reported as one of the major volatiles in HTL effluent derived from algae. A significant amount of acetone was observed in both samples; it was the third most common volatile in the manure-derived HTL effluent and the ninth most common in the food-waste-derived HTL effluent. Large ketone concentrations (>240,000 mg/L) can inhibit fermentative microorganisms [163, 164]. Thus, MD permeate generated from HTL effluent is not anticipated to be a valuable feed stream for fermentation processes [164]. Acetic acid methyl ester was the 9th most abundant compound observed in all the manure-derived streams, however, the amount observed in the food-derived streams was not significant. A number of aldehydes (2-Methylpropanal, 3-Methylbutanal, 2-Methylbutanal, 2-Methyl-2-butenal, butanal) were also detected in these samples. Aldehydes are commonly observed in the aqueous fraction resulting from HTL processing of biomass [165-167]. Ethyl acetate was found in significant amounts in both samples. It is fairly volatile, having a boiling point of 77.1°C [168]. This would explain why a significant amount passed through the membrane and was detected in the permeate and retentate streams.

Pyrazine ($C_4H_4N_2$), a nitrogen-containing compound, was observed in the manure derived HTL effluent. It can be produced by the degradation of proteins present in the wastes during HTL [166]. Although very little pyrazine was detected in the permeate stream of the manure sample, it is possible that it is

responsible for the observed total nitrogen detected there, although the GC×GC method was not able to detect other potentially important forms of organic nitrogen such as amines.

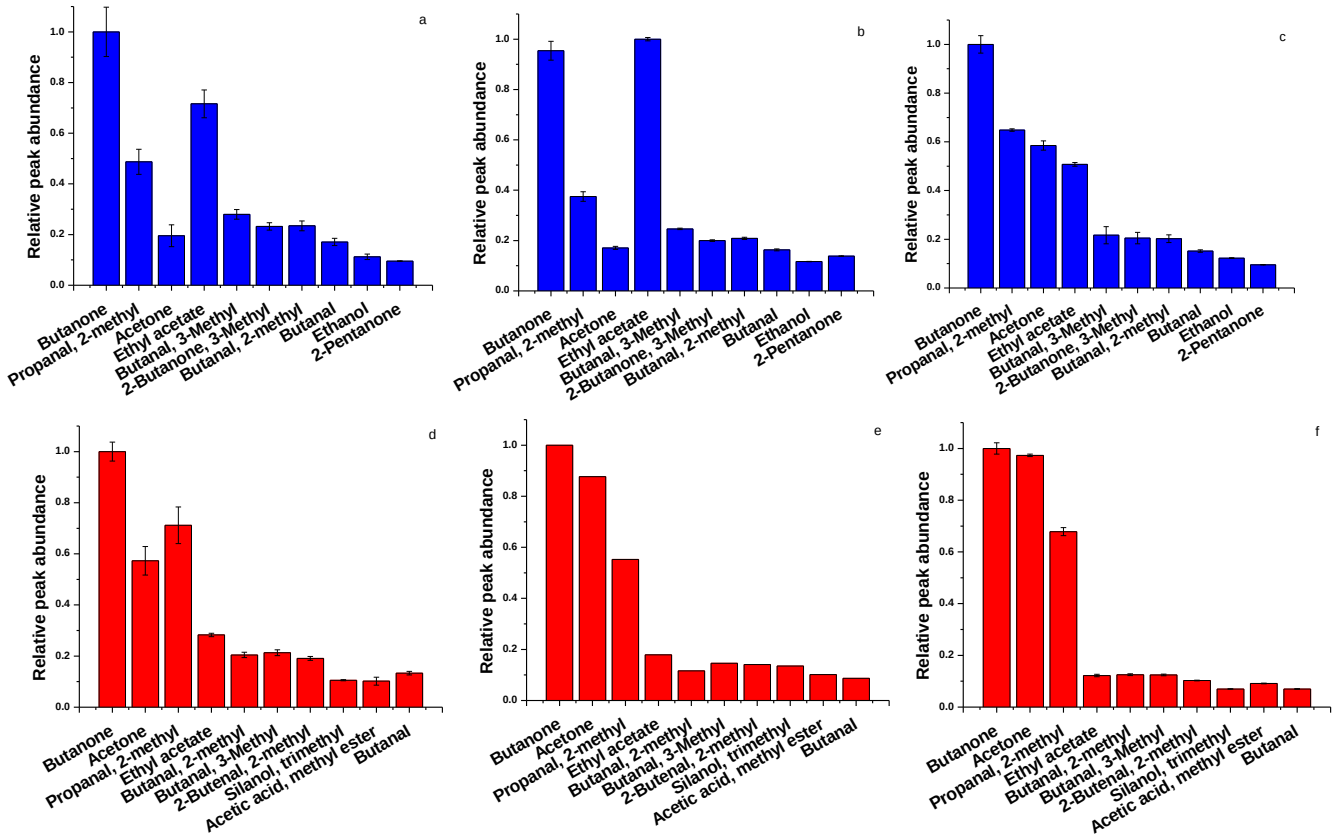

Figure 13: Relative peak abundances for the top ten compounds based on their presence in the permeate stream in the (a) HTL effluent, (b) retentate, and (c) permeate streams of the food waste sample, and (d) HTL effluent, (b) retentate, and (c) permeate streams of the manure sample. Values represent an average of two replicates ± 95% confidence intervals.

Table 1: List of compounds identified in volatiles analysis of the feed, permeate and retentate from food waste and manure MD processing

Alcohols	Ketones
Ethanol	Acetone
1-Propanol	Methylthio-2-propanone
Isopropanol	Butanone
1-Butanol	2,3-Butanedione
2-Butanol	3-Methyl-2-butanone
2-Methyl-2-propanol	3-Methyl-3-buten-2-one
3-Methyl-1-butanol	3-Hydroxybutanone
3-Methyl-2-butanol	3-Hydroxy-3-methyl-2-butanone
2-Pentanol	2-Pentanone

2-Methyl-2-pentanol	3-Pentanone
Amylene hydrate	Cyclopentanone
2-Trimethylsilyloxyethanol	3-Methyl Cyclopentanone
	3-Penten-2-one
Esters	2-Cyclopenten-1-one
Methyl acetate	2-Methyl-cyclopentenone
Ethyl acetate	3-Methyl-2-cyclopenten-1-one
Methyl propionate	2-Methyl-2-cyclopenten-1-one
Ethyl propionate	2,3-Pentanedione
Ethyl butyrate	3-Methyl-1,2-Cyclopentenedione
Ethyl isobutyrate	2,3-Hexanedione
Ethyl-2-methylbutyrate	3,4-Hexanedione
Ethyl isopentanoate	Cyclohexanone
Ethyl isovalerate	2-Cyclohexen-1-one
Ethyl-4-methylpentanoate	Acetyl furan
2-Hydroxyethylpentanoate	
Pentanoic acid,4-oxo ethyl ester	**Aldehydes**
	2-Methhylpropanal
Ethers	Methacrolein
Ethyl ether	Butanal
Ethene ethoxy	2-Methylbutanal
Ethyl-1-propenyl ether	3-Methylbutanal
1-Ethoxy-1-butene	2-Butenal
Tetrahydrofuran	2-Methyl-2-butenal
	2-Ethyl-2-butenal
Acids	2-Methyl-2-pentenal
Acetic acid	2-Ethyl-2-pentenal
4-Methyl-3-pentanoic acid	Hexenal
	2-Methyl-2-hexenal
Miscellaneous: Aliphatic	2,4-Hexadienal
2-Pentene	Benzaldehdye
Trimethyl Silanol	Benzene acetaldehyde
1-Propanol, TMS derivative	Furfural
1-Butanol, TMS derivative	
Pyridine	**Miscellaneous: Aromatic**
2-Methylpyridine	Phenol
Propanenitrile	Guaiacol
3-Methylbutanenitrile	Pyrazine
Dimethyl disulfide	Methyl pyrazine
Dimethyl trisulfide	2-Isopropyl-4-ethyl-5-methyl thiazole
Butyrolactone	2-Isopropyl-4,5-dimethyl thiazole

2.4 Conclusions

Here we investigated the combination of HTL and MD. Aqueous HTL effluent was further treated using MD, generating liquid fertilizer containing high concentrations of nitrogen and phosphorous as the retentate stream, and high concentrations of VOCs in the permeate stream, making further treatment necessary. We demonstrated that polypropylene membranes could be effectively used up to a water recovery of 75%, While membrane fouling did occur, flux was maintained at high levels (>10 LMH). Residual waste heat from HTL could be used to drive MD, which would dramatically reduce the cost of the MD process and increase overall process sustainability.

Acknowledgements:

We would like to thank the BARD program (Project No. US-5051-17) and The United States Department of Agriculture (GRANT NO: 2017-67022-26135) for their generous support.

Chapter 3: Mineral Scale Prevention on Electrically Conducting Membrane Distillation Membranes using Induced Electrophoretic Mixing

Abstract

The growth of mineral crystals on surfaces is a challenge across multiple industrial processes. Membrane-based desalination processes, in particular, are plagued by crystal growth (known as scaling), which restricts the flow of water through the membrane, can cause membrane wetting in membrane distillation, and can lead to physical destruction of the membrane material. Scaling occurs when super-saturated conditions develop along the membrane surface due to the passage of water through the membrane, a process known as concentration polarization. To reduce scaling, concentration polarization is minimized by encouraging turbulent conditions and by reducing the amount of water recovered from the saline feed. In addition, anti-scaling chemicals can be used to reduce the availability of cations. Here, we report on an energy efficient electrophoretic mixing method capable of nearly eliminating CaSO4 and silicate scaling on electrically conducting membrane distillation (ECMD) membranes. The ECMD membrane material is composed of a percolating layer of carbon nanotubes deposited on a porous polypropylene support and cross-linked by poly (vinyl alcohol). The application of low alternating potentials (2 Vpp, 1 Hz) had a dramatic impact on scale formation, with the impact highly dependent on the frequency of the applied signal, and in the case of silicate, on the pH of the solution.

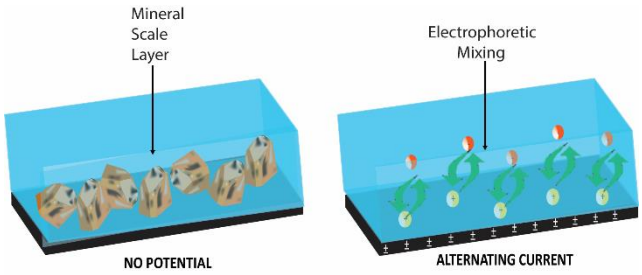

Figure 14: Graphical representation of the process

3.1 Introduction

Membrane-based desalination technologies have been demonstrated to be the most energy efficient methods to produce fresh water from saltwater. Membrane distillation (MD) is a membrane-based thermal desalination technology that has the potential to become a mainstream process for the treatment of high-salinity brines (e.g., oil and gas wastewater), particularly when free thermal energy is available (e.g., from geothermal brines).[115, 169] While nanofiltration (NF) and reverse osmosis (RO) are by far the most common membrane-based desalination methods, these membranes are not capable of effectively treating high-salinity brines (>70 g L^{-1}), due to the excessive hydraulic pressure needed to overcome the solution's osmotic pressure. In fact, the treatment of high-salinity brines is a growing challenge across multiple regions and industries, and MD has shown great treatment potential due to its high efficiency, excellent performance, and low capital costs.[40, 45]

In the MD process, a high salinity feed stream is heated and passed along the surface of a microporous hydrophobic membrane that separates the hot liquid feed from the desalinated cool permeate. A partial vapor pressure difference (generated by the temperature difference between the feed and permeate) leads to water vapor diffusing across the membrane's hydrophobic pores, which then condense in the permeate channel, leaving concentrated dissolved constituents (e.g., ions, particles, pathogens) on the feed side of the membrane.[40, 60] Operating the MD system below the membrane's liquid entry pressure ensures that liquid feed water (carrying salt and other contaminants) does not penetrate into the permeate stream.[49, 70] MD systems can be operated using different configurations, including "direct contact" (DCMD), "air gap", "sweeping gas", and "vacuum". Electrically conducting MD membranes (ECMD), fabricated through the deposition of a percolating network of carbon nanotubes (CNTs) onto a hydrophobic porous substrate, have higher water flux, self-heating capability, and self-cleaning properties.[115, 117] In addition, other electrically conducting membranes have been shown to have multiple anti-fouling properties[40, 48, 49] and have the potential of substantially improving many membrane-based treatment processes.

All membrane-based desalination technologies (and indeed, many other industrially important surfaces, such as heat exchangers) experience multiple forms of surface fouling. In desalination membranes, the passage of pure water through the membrane leads to the formation of a stagnant concentration polarization (CP) layer along the membrane surface.[72, 117] In this layer, the concentration of ions can exceed the solubility limit of certain sparingly-soluble salts, which can form a deposit layer on the membrane surface, known as mineral scale.[170-172] Mineral scaling blocks the membrane's pores, which restricts the passage of water (either liquid or vapor), and can physically damage the membrane's fragile structure.[173] Due to the porous structure of MD membranes, mineral scale can grow inside the membrane's pores, which can lead to membrane wetting (i.e., the formation of hydrophilic pathways through the hydrophobic structure of the membrane) and process failure.[54] The conditions controlling the formation of mineral scale vary widely, and depend on feed water chemistry (pH, dissolved species), feed physical conditions (temperature, mixing), and membrane surface properties (roughness, charge, hydrophilicity).[73, 174] The degree of water recovery (i.e., % of the feed water volume that becomes product water) in desalination is largely controlled by fouling, with mineral scaling being the primary limitation of achieving high recoveries in groundwater desalination, because groundwater contains many multivalent ions that tend to form sparingly soluble minerals (e.g., $CaSO_4$, $CaCO_3$, and $(SiO^{(4-2x)-}_{4-x})_n$).[175] There is a strong environmental and economic incentive to increase water recovery during desalination, as this reduces the volume of waste brine that requires disposal.[176] In fact, mineral scaling impacts other industrial processes, notably heat exchangers, which reduces their efficiency due to the buildup of poorly conducting layers on the exchanger surface.[177, 178] Thus, there is a need to develop new materials and processes that minimize the formation or deposition of mineral scale at the solid/liquid interface.

The precipitation of minerals from solution can occur via a homogeneous (slow) or heterogenous (fast) precipitation process.[179, 180] The conditions inside a membrane desalination system favor heterogenous precipitation, due to the presence of a solid/liquid interface (i.e., the membrane/feed stream), which can lead to rapid membrane scaling.[181] During the heterogeneous precipitation process, it is thought that amorphous mineral "pre-nucleation clusters", numbering just a few atoms, rapidly (within seconds) form

in the bulk in areas with the highest concentration (e.g., at the membrane/water interface).[182] These clusters can aggregate and attach to a surface and serve as induction sites (nuclei) for crystal growth on the surface, where the nuclei grow due to the addition of dissolved ions from the liquid phase, assuming a crystalline structure as their size increases.[183, 184] This results in surface scale formation due to heterogenous crystallization. Thus, to prevent the formation of mineral scale, an ideal system would minimize the formation of these pre-nucleation clusters, prevent any of these clusters from reaching the membrane surface, and limit subsequent growth of a surface crystal structure. Many studies have investigated the kinetics of mineral scale formation during membrane desalination.[185, 186] These studies determined that the rate of scale formation is highly dependent on the degree of supersaturation, with the period of time between the onset of supersaturation and the formation of mineral scaling defined as the "induction period."[187, 188]

The surface charge on a membrane surface has been demonstrated to impact the formation of mineral scale, with negatively charged surfaces (e.g., rich in -COOH groups) being more scaling resistant than positively charged surfaces (e.g., rich in quaternary amine groups).[189, 190] However, when a direct current (DC) external anodic potential (1.5 V cell potential) was applied to the surface of an electrically conducting RO membrane, $CaSO_4$ scaling was significantly delayed. The anti-scaling phenomena was explained through the formation of a thick electrical double layer (EDL), which developed in response to the applied potential.[191] In the EDL, the concentrations of co-ions are depleted relative to those of counter-ions, which reduces the formation of crystal nuclei by locally lowering the saturation index, and slows down mineral scaling. Importantly, these results suggest that external control of ion concentrations along a surface can substantially impact the rate of nucleation, and potentially prevent mineral scaling.

In this study, we report on an efficient anti-scaling method employing alternating currents (AC) applied to the surface of ECMD membranes. The method is applied to prevent both gypsum ($CaSO_4$) and silicate scaling, which are common scaling species encountered during groundwater desalination. We hypothesize that the application of an AC potential at an appropriate frequency induces electrophoretic mixing of the stagnant CP layer, which minimizes the formation of pre-nucleation clusters, and prevents the formation of mineral scale. The results presented in this study are relevant to other membrane-based desalination

processes, and potentially to other surfaces experiencing mineral scaling, such as heat exchangers. These findings can be potentially applicable towards other common scaling species, such as $CaCO_3$ and iron oxide.

3.2 Materials and Methods

3.2.1 Chemicals

Sodium sulfate (Na_2SO_4), magnesium sulfate ($MgSO_4$), sodium metasilicate pentahydrate ($Na_2SiO_3,5H_2O$), aluminum chloride hexahydrate ($AlCl_3,6H_2O$), barium chloride dihydrate ($BaCl_2,2H_2O$), ferric chloride hexahydrate ($FeCl_3,6H_2O$), calcium chloride dihyrate ($CaCl_2$), potassium chloride (KCl), and magnesium chloride hexahydrate ($MgCl_2,6H_2O$) were purchased from Sigma Aldrich and used as received to prepare the feed solutions. Sodium dodecylbenzene sulfonate (Na-DDBS), polyvinyl alcohol (PVA), glutaraldehyde (GA), and hydrochloric acid (HCl) were purchased from Sigma Aldrich and used as received to prepare the membrane materials. COOH-functionalized multi-walled CNTs were purchased from Cheaptubes (Cheaptubes inc., Brattleboro, VT). The CNTs are reported to have an outer diameter of 13-18 nm, a length of 1-12 μm, and purity ≥ 99% with a functional group content of 7.0 ± 1.5%.

3.1.1 Scaling Solution

Table 2: Calcium sulfate scaling solution recipe

Salt	Concentration (mM)
Na_2SO_4	10.500
$MgSO_4$	14.500
$CaCl_2$	16.400
pH	6.9
Ionic strength	139

Table 3: Silicate scaling solution recipe

Salt	Concentration (mM)
$Na_2SiO_3,5H_2O$	8.985
$AlCl_3,6H_2O$	0.051
$BaCl_2,2H_2O$	0.010
$FeCl_3,6H_2O$	0.026
$CaCl_2,2H_2O$	1.439
KCl	1.372
$MgCl_2,6H_2O$	0.605
Na_2SO_4	0.774
pH	10
Ionic strength	37.3

Two different feed water solutions were used to evaluate membrane scaling. The first solution simulates brackish groundwater from the California Buena Vista Water Storage District (Table 2), and was unsaturated with respect to all the ions at a temperature of 90 °C (water temperature in feed tank during the MD process). The saturation index *(SI)* (calculated using visual MINTEQ version 3.1) with respect to

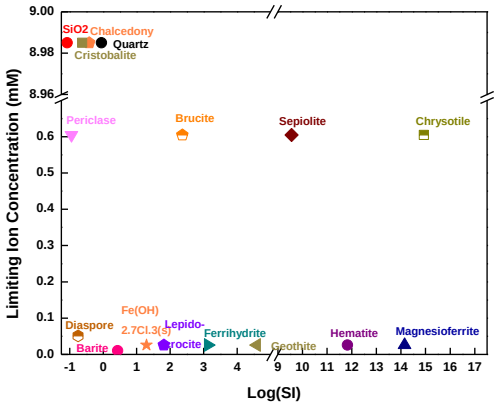

Figure 15: Saturation indices of minerals that could potentially precipitate in the feed during the desalination of silicate solution.

$CaSO_4$ (gypsum) was determined to be 0.59, suggesting that $CaSO_4$ formation is not thermodynamically preferable in the bulk solution[192]. The *SI* was calculated using Equation 25:

$$SI = \left(\frac{[Ca^{2+}][SO4^{2-}]}{Ksp_{CaSO_4}}\right) \qquad \textit{Equation 25}$$

A feed solution prone to silicate scaling, simulating a geothermal brine from Nevada, was used as the second feed (Table 3). However, to speed up the scaling process, the concentration of salts was increased by a factor of 6. The saturation indices of the different potential insoluble salt species in this solution are presented in Figure 17. While the feed solution has multiple potential insoluble species (SI > 0), the most likely species to form sufficient deposits to obstruct flow (and reduce flux) are dominated by silicate species due to their far higher concentrations (Figure 17). The SI of silicate species in the feed was just below 0, indicating that precipitation of these species in the feed solution was not likely.

3.2.2 Fabrication of ECMD Membranes

Polypropylene (PP) membranes with a nominal pore size of 0.59 µm and thickness of 110 µm (3M, Charlotte, NC) were used as the substrate for the fabrication of ECMD membranes. These substrates were coated with a CNT ink via a spray-coating process.[124] To prepare the CNT ink, a 1 g L^{-1} CNT solution was prepared by dispersing the CNTs (1 g) in water (1000 ml) along with the surfactant Na-DDBS (10 g) using an ultrasonic horn sonicator (Branson, Danbury, CT).[193] The suspension was sonicated for 30 minutes, followed by centrifuging (Beckman Coulter, Brea, CA) for 20 minutes at a speed of 11,000 rpm. A 0.1% solution of PVA was prepared by stirring and heating a solution of PVA (1 ml) in water (100 ml) to 95-100 °C for 1 hour, and then diluting it by a factor of 10. CNT ink (200 ml) followed by PVA solution (2 ml) were spray-coated in a layer-by-layer manner using a custom-built spray coater on to a 16 cm X 30 cm piece of PP substrate. The surfactant was then washed away by rinsing the membrane with a steady flow of deionized water for 2 hours. The CNT/PVA network was cross-linked by soaking the material in the crosslinking solution at 70 °C for 1 hour. Crosslinking solution was prepared by dissolving HCl (10 ml)

and GA (10 ml) in water (1000 ml). Following this, the membrane was rinsed in deionized water and air dried. The membrane was then used for testing without any further modification.

3.2.3 System design and operation

Membrane performance was tested using a polycarbonate flow cell housing an MD membrane in a flat-sheet configuration, and operated in DCMD mode (Figure 18). The flow channels on either side of the membrane (feed and permeate) were 8 cm X 5 cm, with a height of 4 mm. Temperature resistant tubing, insulated using ultra-high-temperature mineral wool insulation (McMaster-Carr, Santa Fe Springs, CA), was used to circulate the feed and permeate solutions. The feed was placed in a 10 L tank (McMaster-Carr, Santa Fe Springs, CA) placed on a stir plate (Fisher Scientific, Hampton, NH) and heated with an immersion heater (Process Technology, VXIIII, Mentor, OH) while stirring at 250 rpm. Five temperature sensors (Vtech, DS18b20) were placed throughout the system: one in the feed tank, and one at each of the flow cell inlets and outlets (Figure 18). The temperature sensors were connected to a temperature control unit and the temperature of the hot feed solution could be maintained at a constant value using a PID cascade loop. A vertically mounted level float switch (Madison, M8000, Branford, CT) was used to maintain the liquid level in the feed tank by recirculating it from a permeate buffer tank – this ensured the feed solution was kept at a constant concentration and SI. This was done to ensure no bulk precipitation occurred in the feed tank, which could deposit on the membrane and lead to flux decline. A peristaltic pump (Cole Parmer, Pump Drive Model 7553-70, Pump Head Model 77200-50, Vernon Hills, IL) was used to circulate the feed solution, and gear pumps (Greylor, PQ-12/24, Cape Coral, FL) were used for the permeate and buffer tank. The permeate was collected in a plastic tank placed on a balance (Fisher Scientific Education Precision Balance, Hampton, NH), with cold water continuously circulated on the permeate side; permeate temperature was maintained at 20^0C using a chiller (6500 Series, 1/2 HP, Polyscience, Niles, IL). A conductivity meter (Thermo Scientific, Orion Star A322, Waltham, MA) was placed in the permeate tank to monitor changes in salt concentration (and thus salt rejection and membrane wetting). The system was operated and controlled using open source hardware (Arduino) and software (Python).[159] Flux through the

membrane was measured by the change in weight of the permeate tank. The crossflow velocity of the feed and permeate solutions were maintained at 8 cm s^{-1}, resulting in a Reynold's number of 215. While the temperature in the feed tank was maintained at 90 °C, there was a 12 °C temperature drop from the feed tank to the flow cell inlet, resulting in an inlet temperature of 78 °C. A plastic mesh was used as a spacer on the permeate side, but no spacer was used on the feed side (to encourage scaling). All experiments were conducted in triplicate, with averages and 95% confidence intervals reported.

To connect the membrane to an external potential source, the membrane surface was coupled to an electrode (a stainless-steel machine key stock placed outside of the O-ring, so the electrode does not come in contact with the feed stream), and a Pt-coated Ti sheet served as the counter electrode and placed 3 mm above the membrane surface inside the feed channel. An arbitrary waveform generator (Rigol, Beijing, China) was used to provide the electrical potential to the membrane/counter electrode. During the experiments, different electrical conditions were imposed on the membrane/counter electrodes while maintaining all other operating conditions constant (feed and permeate flow rates and temperatures). To modify the pH during one set of experiments, HCl was added to the feed solution until a pH of 6 was reached.

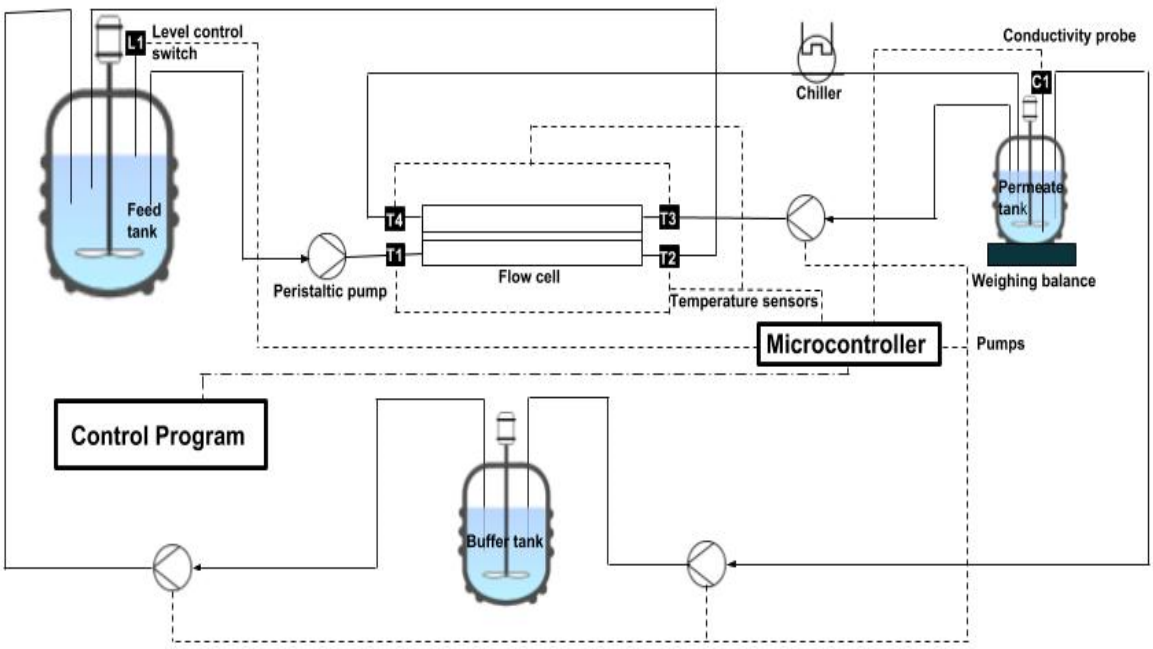

Figure 16: System process diagram

3.2.4 Membrane characterization

Membrane surfaces were analyzed using scanning electron microscopy (SEM) (Zeiss Supra 40VP, Carl Zeiss Microscopy, LLC, NY). Samples were secured on SEM stubs using double sided carbon tape and sputter coated (Ion beam sputtering/etching system, South Bay Technology, San Clemente, CA) with iridium before imaging. Quantitative analysis and surface elemental mapping were carried out using energy dispersive X-ray spectroscopy (EDAX), which is a module included with the Zeiss Supra SEM. Crystal structures deposited on the membrane surface were studied using X-ray diffraction (XRD: Panalytical X'Pert Pro). The scaled membrane was placed in the sample holder for analysis. The ordinary method for XRD analysis is by scraping off the powder and putting it in the sample holder. However, we could not recover sufficient (2g) powder for this and had to use the scaled membrane directly in the sample holder. Current was measured using a digital multimeter (Mastech, MS8268, Pittsburgh, PA). Surface roughness

was determined using a Bruker Dimension FastScan Scanning Probe Microscope (Bruker, Billerica, MA). Membrane sheet resistance was measured using a 4-point conductivity probe (Mitsubishi, MCP-T610, Tokyo, Japan). Contact angle measurements were conducted using a contact angle goniometer (Rame-Hart, Model 250, Netcong, NJ). Electrochemical impedance spectroscopy (EIS), cyclic voltammetry (CV), open circuit potential (OCP) and current response measurements were carried out using a potentiostat (CH Instruments, Austin, TX) with an Ag/AgCl reference electrode. In these experiments, the feed solution was placed in a stirred (250 rpm) beaker with the two electrodes (ECMD membrane as the working electrode, and Pt-coated Ti as the counter electrode) separated by 4 cm to allow for the placement of the Ag/AgCl reference electrode. EIS tests were carried out over a frequency range between 0.1 Hz and 100 Hz with an amplitude of 5mV (10 mV_{pp}). Cyclic voltammetry measurements were conducted over a range of -2 V to +2 V. open circuit potential measurements were conducted at -2 V, and current response measurements were carried out under conditions of 2 V_{DC} and 2 $V_{AC, 1Hz}$.

3.3 Results and discussion

3.3.1 Membrane characterization

The pure water flux for an uncoated PP membrane with feed temperature of 78 ^{0}C and cross flow velocity of 8 cm s^{-1} was determined to be 39.2±3.3 L m^{-2} hr^{-1} (LMH). However, the flux for the CNT/PVA membrane composite was 51.7±2.9 LMH, a 32% increase. This increased flux is consistent with previous reports that describe a significant flux enhancement when a hydrophobic support is coated with a hydrophilic CNT layer, although the mechanism behind this enhancement is unclear. When 2 V_{DC} was applied, the steady state pure water flux was similar (49.1±1.3 LMH), indicating that applied potential has no significant effect on pure water flux through the CNT coated membrane. SEM micrographs of the membrane surface (both the bare PP substrate and CNT/PVA coated substrate) can be seen in Figures 19a and 19b. While the addition of the CNT/PVA layer added an additional barrier to water transport, formed by the non-woven mesh-like structure of the deposited CNTs with an average pore size of 100 nm, the

membrane's performance was still enhanced (in terms of flux). Analysis of a cross sectional image of the CNT/PVA-coated membrane shows that the thickness of this layer was 2 μm (not shown). AFM was used to determine the surface roughness of the bare PP and CNT/PVA composite material, with the root mean square of roughness found to be 390±68 nm and 121±20 nm, respectively (Figures 19c and 19d). The membrane's sheet resistance was determined to be 228±14ohm/square, which translates into a conductivity of approximately 2,200 S m^{-1}. The contact angles of the bare PP membrane and the CNT/PVA coated membrane were determined to be 135.5±0.8°, and 39.7±0.3°, respectively (Figures 19e and 19f). CV curves show the onset of water electrolysis at 0.9 V and -0.7 V vs. Ag/AgCl, for anodic and cathodic conditions respectively, in $CaSO_4$ scaling solution (Figure 19g). In the silicate solution, water electrolysis occurred at 1 V and -0.55 V vs. Ag/AgCl for anodic and cathodic conditions, respectively (Figure 19h). The OCP vs. Ag/AgCl was measured as -0.16 V in the $CaSO_4$ and -0.21 V in the silicate feed streams. The OCP of an oil-water emulsion using a CNT coated membrane and Pt-coated Ti as the electrode pair was -0.13 V in a 0.1 M NaCl solution.[194] The OCP observed in our system is slightly higher for $CaSO_4$ (-0.16 V), and significantly higher for silicate (-0.21 V). Another study comparing the OCP of DI water to a 0.15 M KCl solution showed that solutions with higher ionic strength typically have lower OCPs (0.3 V for 0.15 M KCl and 0.38 V for DI water respectively).[195] The $CaSO_4$ solution, with an ionic strength of 0.139 M had a lower OCP (-0.16 V), while the silicate solution, with an ionic strength of 0.037 M had a higher OCP (-0.21 V), in agreement with previous reports. The current response measurements showed that under 2 V_{DC} conditions, steady state current decreased to 354±17 μA and 313±9 μA from an initial value of 873±30 μA and 814±51 μA (for $CaSO_4$ and silicate respectively). This resulted in a current density (normalized to membrane surface area) of 0.09A/m^2. Under 2 $V_{AC,1Hz}$ conditions (Figure 20), the peak current was identical in each cycle during charging and discharging phases, after reaching steady state, for both feed solutions (880 μA for $CaSO_4$ and 810 μA for silicate). The salt rejection achieved by the membrane exceeded 99% in all experiments.

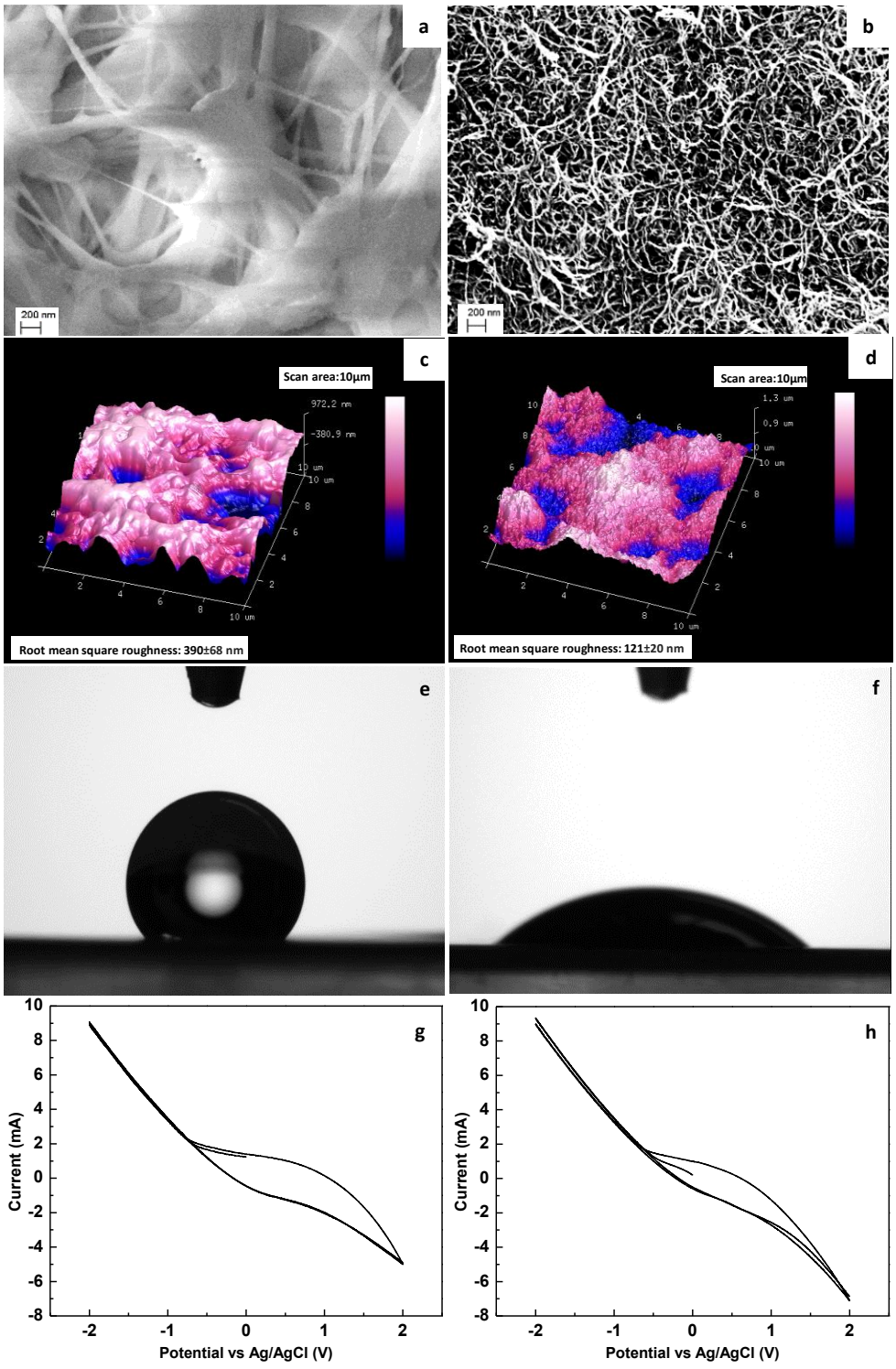

Figure 17: Surface and electrochemical properties: SEM micrographs of (a) bare PP membrane, and (b) ECMD membrane; AFM micrographs of (c) bare PP membrane, and (d) ECMD membrane; water contact angle of (e) bare PP membrane, and (f) ECMD membrane; CV curves of ECMD membrane; CV curves of ECMD membrane as working electrode in (g) $CaSO_4$ feed solution, and in (h) silicate feed solution

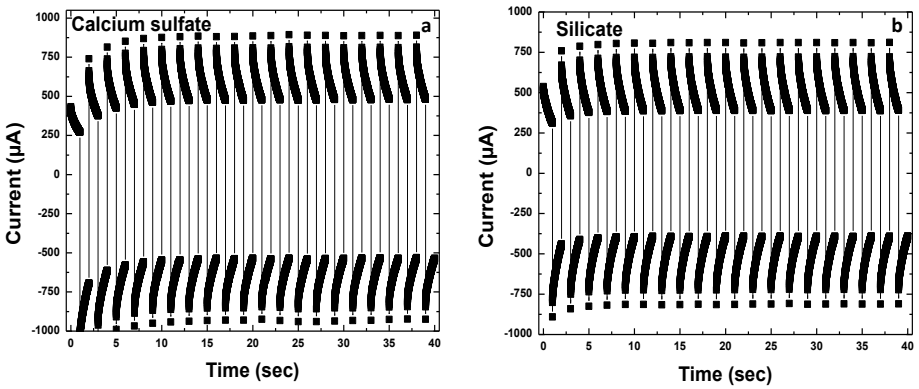

Figure 18: Chronoamperometry curves with CNT membrane and metal plate (Pt-Ti) as electrodes for (a) $CaSO_4$, and (b) silicate solution.

3.3.2 Calculation of temperature and saturation index along the membrane surface[62]

The following equations were used to calculated surface temperature and saturation index.

$$c_m = c_b * exp\,(J/\rho K) \qquad \textit{Equation 26}$$

Where, c_m is the salt concentration at the membrane surface, c_b the salt concentration in the bulk, J the flux of water across the membrane (kg m^{-2} s^{-1}), ρ the density of water (kg m^{-3}), and *K* the solute mass transfer coefficient (m s^{-1}). The solute mass transfer coefficient can be calculated using the Graetz-Leveque mass transfer analogy:

$$Sh = 1.86(Re * Sc * \frac{d_h}{L})^{0.33} \qquad \textit{Equation 27}$$

where L is the length of the channel, d_h is the hydraulic diameter, and Sh and Sc are Sherwood and Schmidt numbers respectively, which can be calculated using:

$$Sh = \frac{K*d_h}{D} \qquad \textit{Equation 28}$$

$$Sc = \frac{\mu}{\rho*D} \qquad \textit{Equation 29}$$

where μ is the viscosity of water, and D the diffusion coefficient of the solute.

The flux (J) in Equation 26 is calculated by iteratively solving for the membrane surface temperatures on the feed and permeate side using eq. 30-39. Temperature difference in MD system leads to heat transfer from the hot feed to cold permeate. In addition to heat transfer, vaporization of water at the feed side leads to a further decline in temperature due to loss of latent heat. To account for the polarization effect, we assume steady state conditions with heat transfer (Q) in the bulk of the feed and permeate to be equal to the heat transferred across the membrane:

$$Q = h_f(T_{bf} - T_c) = h_c(T_c - T_{mp}) + J\lambda = h_m(T_{mf} - T_{mp}) = h_p(T_{mp} - T_{bp}) \quad \textit{Equation 30}$$

$$T_{mp} = T_{bp} + \frac{(T_{bf} - T_{bp})}{h_p}\left[\frac{1}{(1/h_m)+(1/(h_c+h_v))+(1/h_f)+(1/h_p)}\right] \quad \textit{Equation 31}$$

$$T_c = T_{bf} - \frac{(T_{bf} - T_{bp})}{h_f}\left[\frac{1}{(1/h_m)+(1/(h_c+h_v))+(1/h_f)+(1/h_p)}\right] \quad \textit{Equation 32}$$

where T_{bp} and T_{bf} are the bulk permeate and feed temperatures respectively, T_c, T_{mf}, T_{mp} are the temperatures of the CNT surface, PP membrane surface, and PP back side (i.e., permeate side), and h_f, h_p, $h_m, h_v,$ and h_c are the heat transfer coefficients on the feed side, permeate side, membrane, vapor and the CNT layer respectively (calculated from equations 34-39). h_f and h_p are calculated using the Nusselt equation:

$$h_x = \frac{Nu_x k_x}{d_h} \quad \textit{Equation 33}$$

where, k_x is the fluid thermal conductivity.

Nu_x in Equation 30 is the Nusselt number, obtained using the equation:

$$Nu = 1.86(Re\ Pr \frac{d_h}{L})^{0.33} \quad \textit{Equation 34}$$

$$\textit{Where, Reynolds number, } Re = \frac{d_h\, v\, \rho}{\mu} \quad \textit{Equation 35}$$

$$\textit{And Prandtl number, } Pr = \frac{c_p\, \mu}{k} \quad \textit{Equation 36}$$

where ν is the velocity, c_p is the specific heat capacity, and k is the thermal conductivity of the fluid.

$h_m, h_v,\ and\ h_c$ are determined as:

$$h_m = \frac{k_m}{\delta_m} \qquad \textit{Equation 37}$$

$$h_v = \frac{J\lambda}{T_c - T_{mp}} \qquad \textit{Equation 38}$$

$$h_c = \frac{k_c}{\delta_c} \qquad \textit{Equation 39}$$

Where, $k_m, k_c\ and\ \delta_m, \delta_c$ are the thermal conductivity and thickness of membrane and the CNT layer respectively, and λ is the latent heat of vaporization.

3.3.3 Modeling surface pH under the influence of applied potential

Equation 40 was solved to estimate surface pH which was found to be 6.9 for $CaSO_4$, and 10.02 for silicate

$$j = \frac{F}{\delta} * [D_H^+ * \left(C_H^{+s} - C_H^{+b}\right) - D_{OH}^- * K_{OW} * (\frac{1}{C_H^{+s}} - \frac{1}{C_H^{+b}})] \qquad \textit{Equation 40}$$

Here, j signifies current density, D_H^+ is proton diffusion coefficient, C_H^{+s} is the surface proton concentration to be calculated, C_H^{+b} is the bulk proton concentration, D_{OH}^- is the diffusion coefficient of the hydroxide ion, K_{OW} is the ionic product of water, F is Faraday's constant and δ is the boundary layer thickness.

3.3.4 Membrane distillation performance

During all experiments, the initial water flux (time zero) through all membranes ranged between 38 LMH and 43 LMH when salt solution was used as the feed. These values were similar to the pure water flux measured through the uncoated PP membrane (39.2 LMH), but were lower than the pure water flux through the CNT/PVA membrane composite (51.7 LMH). The presence of solute in the feed alters the vapor pressure, density and viscosity and also affects heat transfer due to change in heat capacity and thermal conductivity. Typically, salts present in feed water lower the flux.[160] It is not clear why the presence of salt

lowered flux through the CNT/PVA membrane, but did not impact the flux through the uncoated PP membrane.

Scaling occurs when ions accumulate in the CP layer with the highest concentrations at the membrane surface and decaying from there out into the bulk.[196] Supersaturation conditions are likely to develop in the CP layer first, leading to heterogenous crystal nucleation and growth on the membrane surface, resulting in flux decline.[197] Because our experiments were operated using constant feed conditions (i.e., not in concentration mode), the ion concentrations along the membrane surface (i.e., inside the CP layer) could be calculated using Equations 26-39. Based on these equations, and visual MINTEQ, the SI values along the membrane surface were determined to be 2.28 and 3.18 for $CaSO_4$ and silicate, respectively. These values indicate that supersaturated conditions did indeed develop along the membrane surface, and mineral scaling would likely occur given sufficient time. Importantly, an SI of 2.3 is considered the highest SI where anti-scalant chemicals are capable of minimizing $CaSO_4$ scaling, emphasizing the difficult nature of the operating conditions employed herein.[198] We estimated membrane surface temperature (using Equations 26-39) to be 70^0C on the feed side and 27^0C on the permeate side (with a bulk temperature of 78^0C and 20^0C, respectively), resulting in a temperature polarization coefficient of 0.74. While electrothermal heating of the membrane is possible, the required electrical power needed to significantly raise the surface temperature are far higher than what was applied here (0.0008 W). Therefore, it is unlikely that the application of the surface potentials in this study would lead to any significant surface temperature increase.

The normalized (to time zero) flux during the treatment of solutions prone to $CaSO_4$ and silicate scaling can be seen in Figures 21a and 21b, respectively; the average flux decline rate (LMH hr^{-1}), determined by fitting a linear function through the data points can be seen in Figures 21c and 21d, along with the associated R^2 values. Figures 21c and 21d also show induction time for flux decline under different applied potentials. Based on the SI calculated for the two feed solutions, we anticipated that the time scales for scaling would be significantly different. As expected, the silicate solution, having a higher SI, scaled the membrane in a much shorter time span. In addition to the high SI of the silicate solution, previous studies have

demonstrated that the presence of certain cations, such as calcium and magnesium, promote silicate nucleation and polymerization during the fouling of MD membranes.[199]

During the scaling experiments, some of the runs exhibited two distinct flux regimes: an initial period of no flux decline (i.e., the induction period), and a period where flux decline occurred (Figure 21). However, these two regimes were not obvious in all experiments. For example, during the experiments with the uncoated membrane, rapid flux decline was immediately observed (Figures 21a and 21b. We fitted linear functions through the region where flux decline did occur for each experimental condition tested (Figures 21a and 21b). Nghiem and Cath (2011) reported that the induction period of $CaSO_4$ and silicate scaling manifested as a period with no flux decline, followed by a period of rapid flux decline and scaling. Similar observations were made during the scaling of NaCl.[200] In our most successful experimental runs, there was a long induction time, with only slow flux decline observed later on during the experiments (e.g., when 2 $V_{AC,1\ Hz}$ were applied, Figures 21a and 21b).

Because the trends in flux decline as a function of the applied surface potential were similar, we will discuss the results of $CaSO_4$ and silicate scaling together. In both cases, the uncoated PP membrane exhibited rapid flux decline, with a flux decline rate of 10 LMH hr^{-1} and 25 LMH hr^{-1}, respectively (Figures 21c and 21d). These rates are in-line with the higher SI of the silicate solution, which would lead to more rapid precipitation relative to $CaSO_4$. The higher SI increases the probability of reaching supersaturation conditions in the CP layer. This rapid flux decline is also in agreement with prior studies where flux decline for silicate solutions begins instantly, while scaling by $CaSO_4$ has a non-zero induction period.[201] Several striking observations emerge when viewing the scaling results on the CNT/PVA membranes. Simply coating the PP support with the CNT/PVA composite increased the induction period for $CaSO_4$ from 40 to 60 minutes, and lowered the rate of both $CaSO_4$ and silicate scaling, reducing the rate of flux decline from 10 LMH hr^{-1} to 3.75 LMH hr^{-1} for $CaSO_4$ (a 62.5% decline) and from 25 LMH hr^{-1} to 18 LMH hr^{-1} for silicate (a 28% decline) (Figure 21c and 21d). This is in line with previous reports that indicate that the addition of a hydrophilic layer (i.e., CNT/PVA) onto the hydrophobic MD membrane reduces the degree of scaling. In general, hydrophilic surfaces are more resistant to scaling due to the presence of a tightly-

bound water layer at the membrane/water interface, which minimizes the attachment of foulants, including mineral scale.[202] The surface roughness of the CNT/PVA coated membrane is less than that of the bare PP support (390±68 nm versus 121±20 nm). This could also be a contributing factor to the reduced flux decline rate in the tests with CNT/PVA coated membrane, since surface roughness has been shown to impact mineral scaling, with more rough surfaces being more prone to scaling.[203]

For the case of $CaSO_4$ scaling, the application of a 2 V_{DC} cell potential did not increase the induction time, but did result in a drop in the rate of flux decline (compared to the 0 V), from 3.75 LMH hr^{-1} to 1.35 LMH hr^{-1} (a 64% decline). For the silicate system, 2 V_{DC} cell potential increased the induction time to 40 minutes and reduced the rate of flux decline from 18 LMH hr^{-1} to 12.5 LMH hr^{-1} (a 30% decline) (Figures 21a-d). There is a possibility that the enhanced performance due to the applied potential may have been caused by a change in pH at the membrane surface. Under 2 V_{DC} potential, we used Equation 40 to estimate the pH at the surface, and obtained a surface pH of 10 for silicate and 6.9 for calcium sulfate. This represents a negligible change in surface pH conditions. The reason for decrease in the rate of flux decline under 2 V_{DC} cell potential is unclear. When AC conditions were used, the net change in pH is likely zero. Therefore, changing pH conditions are not likely to contribute to the observed phenomena. When an AC potential was applied to the membrane, the results were significantly different than the DC conditions. During $CaSO_4$ scaling, when 2 $V_{AC,\ 10\ Hz}$ were applied, the flux decline was faster than the 2 V_{DC} case (with a rate of 2.82 LMH hr^{-1} vs. 1.35 LMH hr^{-1}), and no induction period was apparent (Figures 21a and 21c). However, when the silicate solution was treated during the application of 2 $V_{AC,\ 10\ Hz,}$ the flux decline rate decreased to 8 LMH hr^{-1}, down from 12.5 LMH hr^{-1} under 2 V_{DC}. It is unclear why the silicate solution exhibited better performance under these conditions (2 $V_{AC,\ 10\ Hz}$), while the $CaSO_4$ performed worse.

For both scaling solutions, the best performance was observed when 2 $V_{AC,\ 1\ Hz}$ cell potential was applied to the membrane surface. For the $CaSO_4$ case, the induction period increased dramatically to 200 minutes, and the flux decline rate declined to 0.7 LMH hr^{-1} (81% smaller than at 0 V). For silicate, the induction time increased to 100 minutes, and the rate of flux decline rate decreased to 3.8 LMH hr^{-1} (79% decrease vs. 0 V). However, when the pH of the silicate-rich feed solution was decreased to 6, the rate of

flux decline increased to 4.2 LMH hr^{-1} (when 2 $V_{AC,\ 1\ Hz}$ were applied) and the induction period decreased to 20 minutes (Figure 21b). At lower pH conditions, silicate solutions are less soluble, which could cause silicates to precipitate at pH 6, resulting in increased flux decline. To evaluate this possibility, we conducted a control experiment with the CNT coated membrane and no potential applied (0 V), and a silicate solution at a pH of 6 (Figure 21b). Under these conditions, the flux decline rate was 18.44 LMH hr^{-1}(Figure 21d). This was very similar to the flux decline rate under 0 V at pH 10 (18.08 LMH hr^{-1}). Based on this, the increased membrane scaling observed under the lower pH conditions (at 2 $V_{AC,1Hz}$ conditions) cannot be attributed to enhanced precipitation of silicate in the solution. Hence, we can rule out bulk precipitation as the cause for increased flux decline rate under 2 $V_{AC,1Hz}$ conditions for the silicate solution at pH 6.

Since the exact speciation of the silicates in our feed solutions are impossible to predict (and is likely a mix of several species), it is likely that reducing the pH of the feed solution will transform some (or all) of the silicates to their non-charged forms, which will not respond (or respond to a lesser extent) to the applied

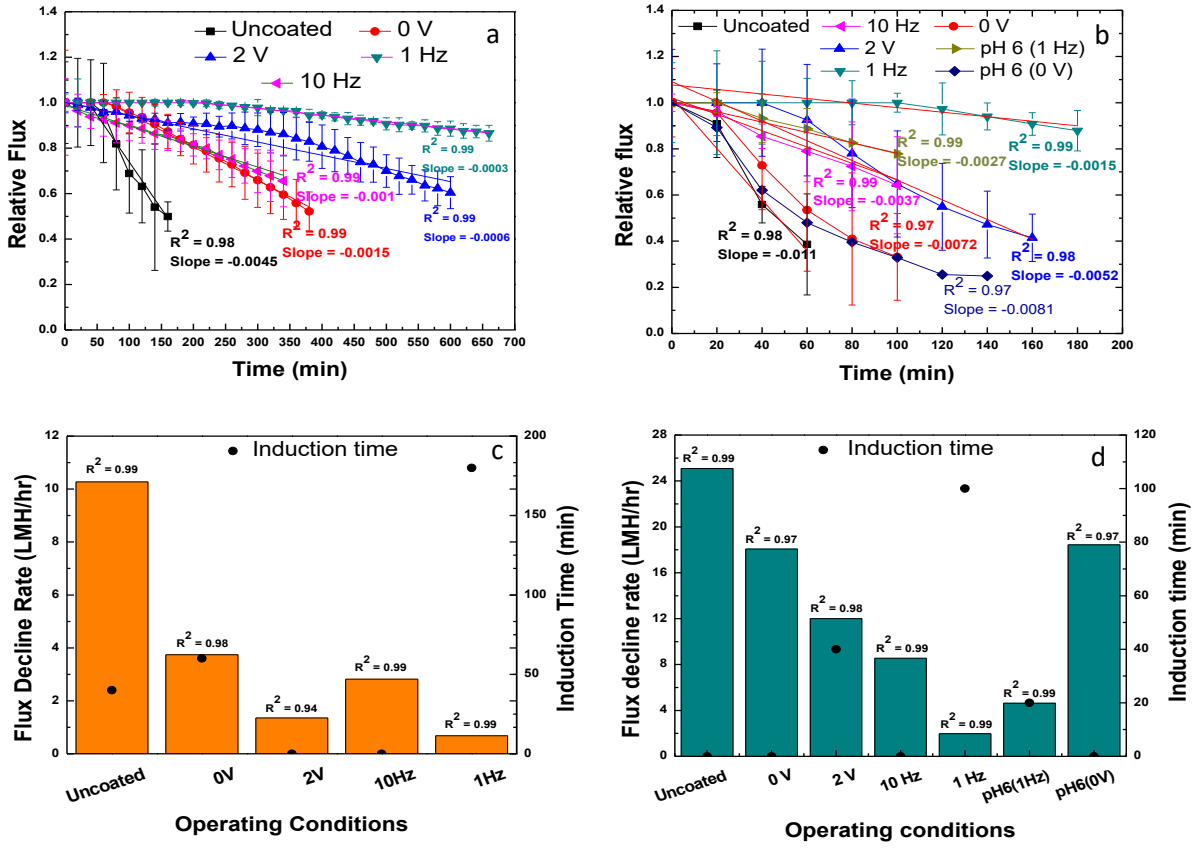

Figure 19: Flux decline under different applied electrical conditions with (a) $CaSO_4$ and (b) Silicate solutions as feed. Rate of flux decline under different conditions for (c) $CaSO_4$ and (d) silicate solutions.

electrical potential.[204] Thus, it is not surprising that membrane flux started declining after a shorter time and the rate of flux decline was faster, as silicate scaling was not effectively prevented through the application of potential. Since $CaSO_4$ is insensitive to pH changes, we do not expect the scaling behavior of the $CaSO_4$ solution to change at a reduced pH. From the above results and from figures 21c and 21d, it is evident that the membrane surface properties, applied electric potential and solution pH (in the case of silicate) had a significant impact on the rate of flux decline and induction time.

3.3.5 Membrane surface characterization after scaling

We have provided pictures of the scaled membrane surface for visual inspection of the scaling layer (Figure 22). A dense scaling layer is observed under 0 V conditions for both feed solutions. In the test with $CaSO_4$, the rate of flux decline was faster under conditions of 2 $V_{AC,\ 10Hz}$ than 2 V_{DC}. (2.82 LMH hr^{-1} vs 1.35 LMH hr^{-1}), and we expected to see a more densely scaled layer on the membrane scaled under 2 $V_{AC,\ 10Hz}$ conditions. However, the surface of the membrane scaled under 2 V_{DC} conditions appeared to be more densely coated with $CaSO_4$ scale. The reason for this is not clear. They were both less densely coated than the membrane scaled under 0 V conditions. For the silicate scaled membrane, the surface coverage appeared to be similar for 2 V_{DC} and 2 $V_{AC,\ 10Hz}$ (both less dense than 0 V conditions). The surface of the membrane scaled under conditions of 2 $V_{AC,\ 1Hz}$ was sparsely covered by a scaling layer for membranes scaled by both solutions. This agrees with our experimental results that 2 $V_{AC,1Hz}$ conditions provide the best scaling resistance. SEM images were used to qualitatively assess membrane scaling. An SEM micrograph of a $CaSO_4$-scaled CNT/PVA coated membrane with no potential revealed a mixture of needle-like and plate-like crystals (Figure 23a). Past investigations have shown that the morphology of crystals depends on the SI and crystallization kinetics.[73, 205] Needle-like crystallization is observed when crystals formed in the bulk phase (due to formation of nuclei in the bulk phase and subsequent attachment on dissolved ions) attach to the membrane surface (bulk crystallization), while plate-like formations are observed when crystal growth occurs on the membrane surface (due to the formation of nuclei on the membrane surface and subsequent deposition of dissolved ions) (surface crystallization).[206] EDAX analysis showed that the membrane was

primarily covered by a thick layer of calcium and sulfur (Figure 23a). XRD analysis of the membrane scaled under 0 V (Figure 24a) showed a diffractogram that can be associated with the presence of gypsum, with peaks at 2θ values of 11.6, 20.5, 23.4 and 29.07.[207]

On the silicate scaled membrane, a uniform colloidal layer was observed covering the surface (Figure 23b). This is consistent with past studies that show the polymerization of silicate monomers in the presence of divalent cations results in a colloidal, gel-like scaling layer.[208] Some structures were observed deposited on top of this silicate scaling layer. EDAX analysis of the deposits indicated that the surface was covered by silicon and magnesium containing minerals (Figure 23b). XRD analysis of silicate scaled membrane (Figure 24b) did not reveal diffraction patterns that could be associated with any major silica containing crystals. This is likely due to the amorphous gel-like layer of silicates on the fouled membrane surface.

An SEM micrograph of the CNT/PVA membrane surface after 2 V_{DC} cell potential was applied while treating the $CaSO_4$ solution shows a large number of needle-like crystals that are characteristic of bulk crystallization[186, 209], suggesting that bulk crystallization dominates scaling under 2 V_{DC} conditions (Figure 23c). SEM and EDAX analysis of the silicate scaled membrane after the application of 2 V_{DC} showed a similar colloidal layer interspersed with a larger number of plate-like structures (Figure 23d), indicating more scaling on the surface. SEM micrographs of the membrane surface after the application of 2 $V_{AC,10\ Hz}$ showed uniform crystal deposition throughout the membrane surface for both the $CaSO_4$ and silicate scaled membranes (Figure 23e). SEM micrographs of the $CasO_4$ scaled membrane after 2 $V_{AC,1\ Hz}$ was applied to the membrane surface revealed a very sparse cover of sharp needle-like crystals, similar to those formed by the crystallization of gypsum in bulk liquid.[73] A zoomed- in micrograph revealed the presence of smaller crystals (150 nm) on the surface (Figure 23g). In Figure 23h, the silicate scaled membrane was not as thoroughly covered by silicon. For both $CaSO_4$ and silicate scaled membranes, the CNT network was visible in the SEM micrographs, indicating poor surface coverage when 2 $V_{AC,1\ Hz}$ was applied. These observations

match our flux decline observations, where under the 2 $V_{AC,1Hz}$ conditions, the membrane experienced dramatically less flux decline.

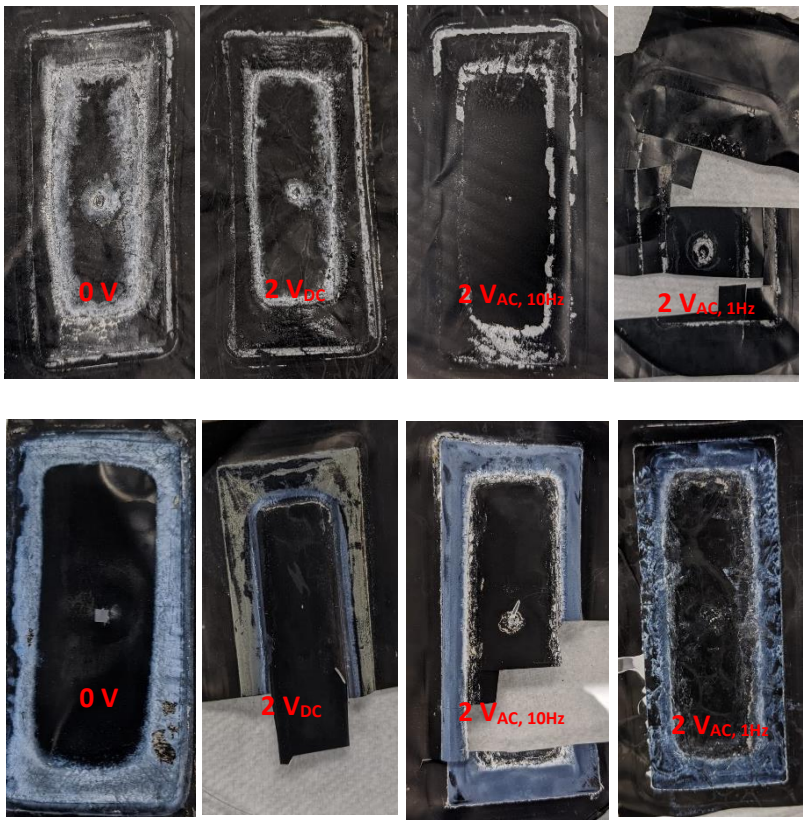

Figure 20: Pictures of the (a) CaSO4 and (b) silicate scaled membranes under different operating conditions

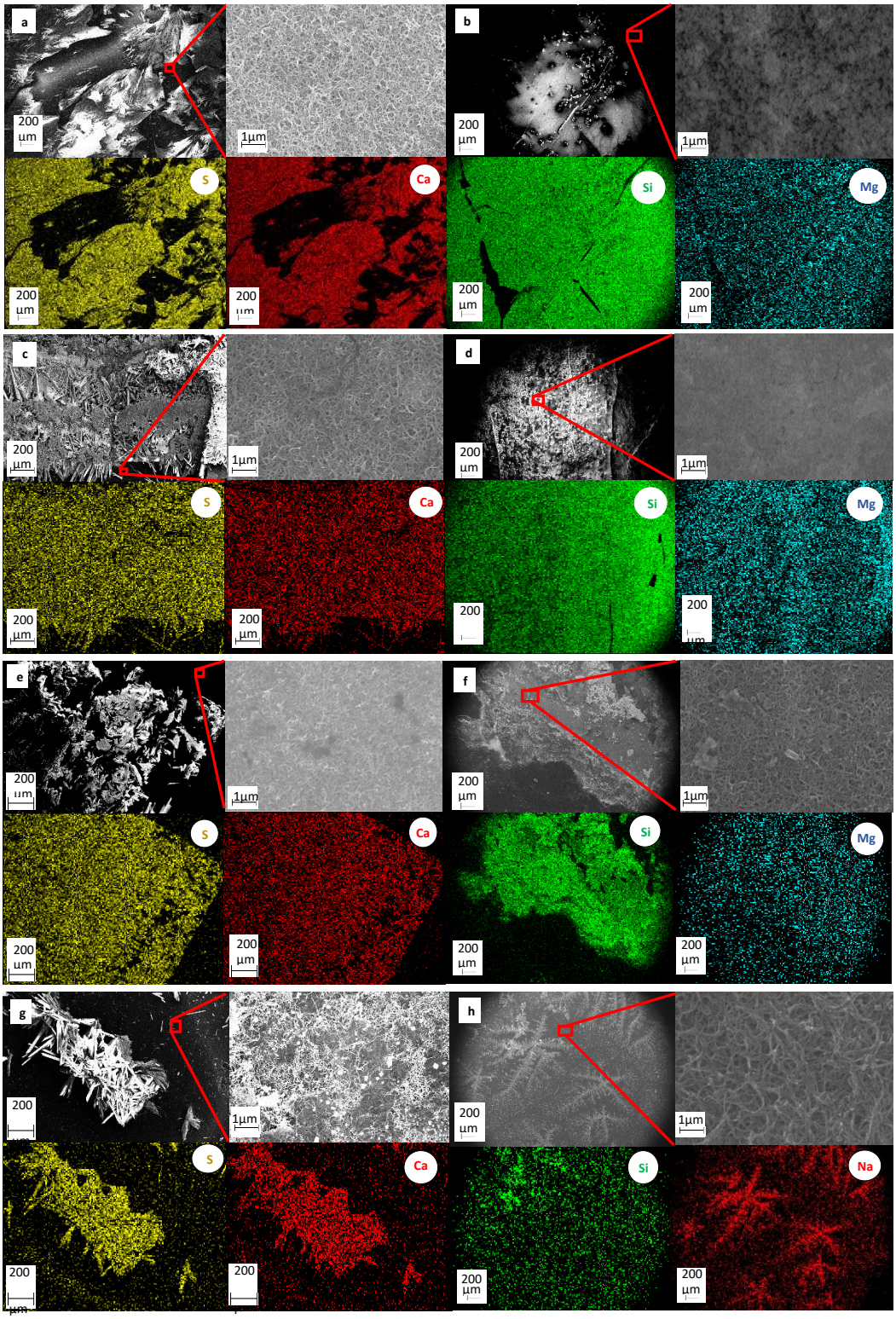

Figure 21: SEM and EDAX micrographs of membrane surface post scaling experiments under different applied electrical conditions (a) $CaSO_4$, 0 V; (b) silicate, 0 V; (c) $CaSO_4$,$2V_{DC}$; (d) silicate, $2V_{DC}$; (e) $CaSO_4$, $2V_{AC,10Hz}$; (f) silicate, $2V_{AC,10Hz}$; (g) $CaSO_4$, $2V_{AC,1Hz}$; and, (h) silicate $2V_{AC,1Hz}$

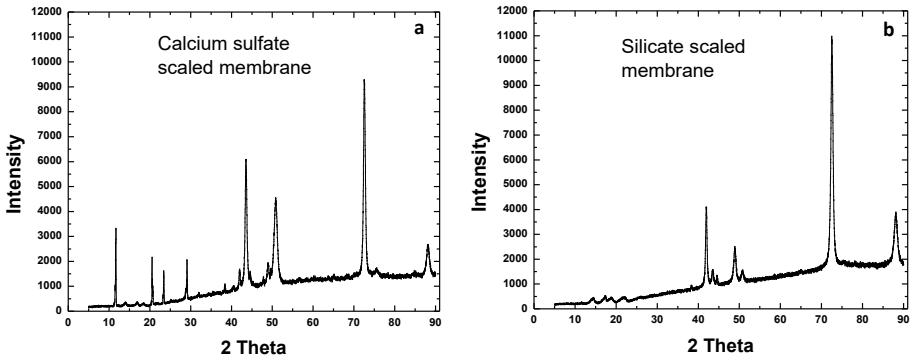

Figure 22: X-ray diffractogram of the (a) $CaSO_4$ and (b) silicate scaled membranes.

3.3.6 Proposed mechanism of scaling inhibition

Mineral scaling is induced by super-saturated conditions, which in our system can rapidly develop due to concentration polarization adjacent to the membrane (Figure 25a). It has been shown, using $CaCO_3$, that nano-scale amorphous pre-nucleation clusters rapidly form on the time scale of seconds in areas where super-saturation conditions exist in the bulk liquid phase. These clusters then attach to a surface, and serve as a template for further (and rapid) crystal growth due to deposition of ions from the solution.[182, 210] A similar phenomenon has been observed with hemihydrate $CaSO_4$.[211] In our previous work, we observed that the application of a 1.5 V_{DC} cell potential to the surface of an electrically-conducting RO membrane slowed the rate of $CaSO_4$ scaling.[72] The mechanism responsible for the observed anti-scaling phenomena was hypothesized to be the formation of a thick EDL along the membrane surface. When a DC potential is applied, counter ions from the bulk solution are attracted to the membrane surface (forming the EDL structure within the CP layer), which creates an imbalance in the concentration of anions and cations (Figure 25b). It has been demonstrated that the rate of nucleation is impacted by the degree of saturation and by the availability of both anions and cations to come together and form the crystal structure, with the highest rates occurring when the ratio between anions and cations is stoichiometric.[212, 213] Thus, in the EDL, where there is an imbalance between anion and cation concentrations (pushing the ratio away from stoichiometry), the

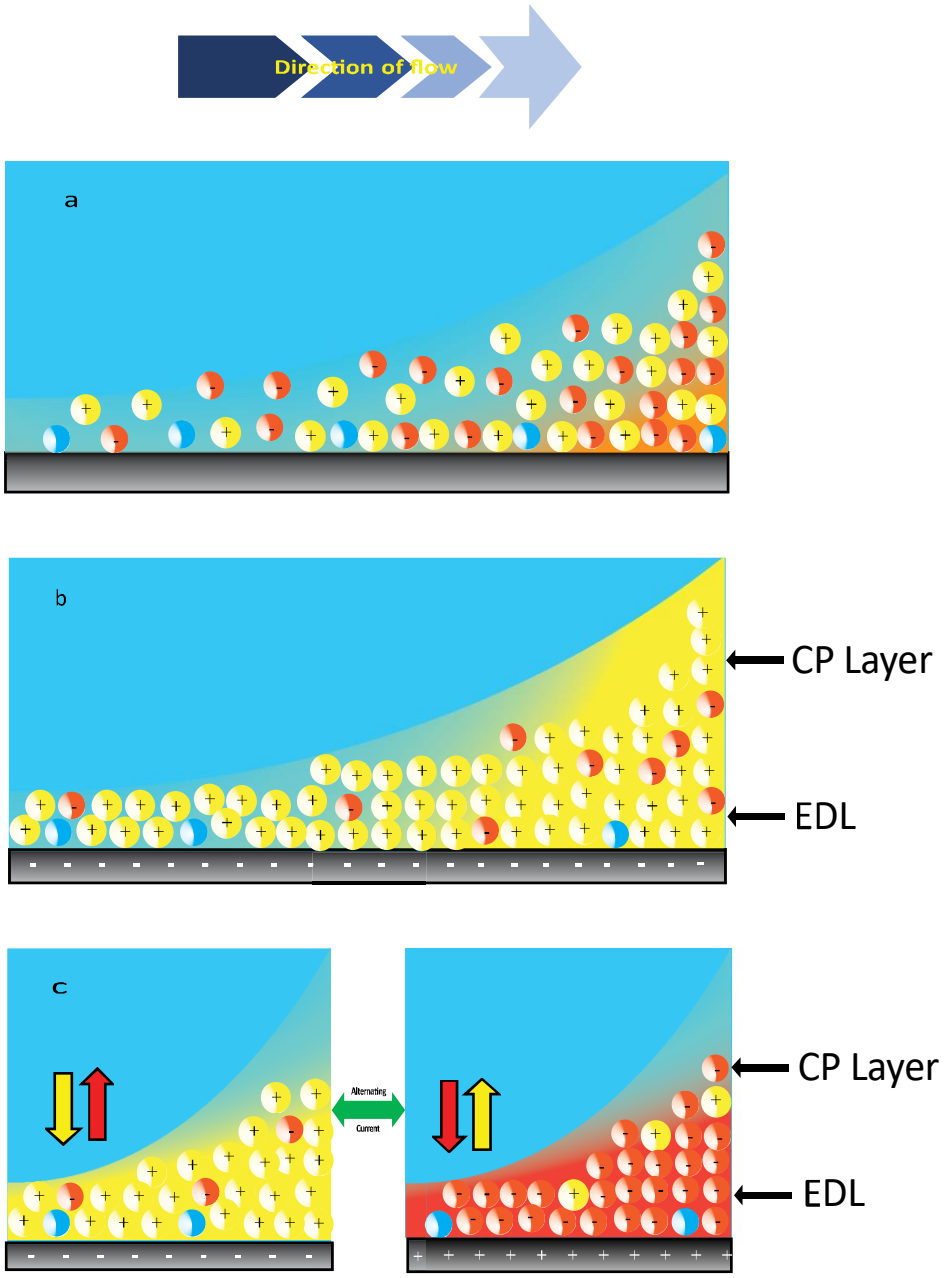

Figure 23: Graphical representation of scaling mitigation by electrophoretic mixing. (a) Formation of CP layer near the surface of an uncharged membrane; (b) formation of EDL near the membrane surface through the application of 2 VDC potential (membrane as cathode); (c) electrophoretic mixing within the CP layer due to EDL disruption and reformation caused by switching the polarity of the membrane.

nucleation rate is lower. The EDL thickness was calculated using the Debye-Huckel theory (Equation 41) and found to be 1.46 nm for $CaSO_4$ scaling solution and 2.64 nm for silicate scaling solution, while the CP layer can vary in thickness from a few microns to a few hundred microns.[214]

$$\lambda_D = \left(\frac{\varepsilon k_B T}{e^2 \sum n_i z_i^2}\right)^{0.5} \qquad \textit{Equation 41}$$

Where, λ_D is the Debye length which is a measure of EDL thickness, $\varepsilon,\ k_{B,}\ and\ T$ are the permittivity, Boltzmann constant and temperature respectively, e is the charge on one electron, n_i and z_i are the ionic concentration and charge of individual ions in the solution.

Therefore, this imbalance does not extend throughout the CP layer, and as a result, the nucleation zone is only pushed a short distance away from the membrane surface (Figure 25b).[184, 215] Thus, just a few nm away from the membrane surface (i.e., outside of the EDL), the ratio between anions and cations returns to that which enables rapid scale formation and prenucleation clusters can be formed under these conditions. That being said, the newly formed pre-nucleation clusters have to transport over a longer distance to reach the membrane surface, and once there, the imbalance between the anions and cations slows further crystal growth. When considering membrane roughness and the thinness of the EDL relative to the CP layer, it becomes clear that a DC potential, while capable of slowing down nucleation, cannot completely prevent scaling, which is evident by our experimental results presented in Figure 21. Furthermore, since applying DC potential pushes the nucleation zone away from the membrane surface, bulk crystallization is expected to dominate the scaling process. Our SEM micrographs of the 2 V_{DC} condition (figures 23c and d) show needle-like deposits, which are characteristic of bulk crystallization.

In contrast to the steady EDL formed in response to a DC potential, the application of an AC potential periodically forms and disrupts the EDL, with the periodicity of this disruption dependent on the frequency of the applied electrical potential[216]. When the field direction is changed, anions and cations move in opposite directions in response to the field, potentially leading to electrophoretic 'mixing' within the CP layer (Figure 25c). Studies on the current response during the charging and discharging of the EDL show that the current is highest at the instance when a potential is applied and exponentially decreases as the EDL is formed, reaching a constant value after complete formation of the EDL. Thus, if the polarity of the electrode is switched at a sufficiently rapid rate, this ion flux (current) can be maintained at a higher rate to encourage better mixing. In our current response curves (Figure 20), for $CaSO_4$, the initial peak current of

880 µA decreases to 480 µA before changing direction (when the polarity is changed) and immediately surging to 880 µA in the opposite direction. For silicate (Figure 20b), the initial peak current is 810 µA, which decreases to 390 µA before changing direction and immediately surging to 810 µA (when the polarity is switched). Thus, switching polarity at a rapid rate will induce movement of ions, encourage mixing, and prevent the formation of prenucleation clusters by preventing co-location of scale forming ions. We hypothesize that this mixing may extend beyond the boundaries of the EDL, thus promoting longer-range disruption of ion concentrations along the membrane surface. This disruption limits the time anions and cations spend in close proximity in the near-membrane region, which limits the formation of pre-nucleation clusters critical for heterogeneous nucleation.[217] Importantly, it is unlikely that the ion migration will result in significant water movement, as the applied fields (500 V/m) are relatively weak.[218] We hypothesize that the periodic switching of the membrane's polarity will induce long-distance (i.e., beyond the EDL boundaries) disruption of ion concentrations within the CP layer, and that this mixing is due only to the movement of ions, and does not result in any bulk liquid motion.

When we reduced the pH of the silicate solution to 6, which transformed silicate monomers primarily to their uncharged state, scaling prevention was curtailed. This strengthens our hypothesis that ion migration in response to the changing electrical field is responsible for the observed anti-scaling phenomenon.

We explored the role of electrosorption in the CNT network by measuring the specific capacitance of the membranes, which was determined to be 0.54 F/g. This value is significantly lower than values associated with capacitive deionization CDI electrodes composed of activated carbon(143 F/g).[219] In addition, CV curves typically observed during CDI are rectangular in shape, indicating consistent ionic loading during the charging step, while the CV curves associated with our membranes show limited charging behavior, indicating a limited role of electrosorption in our system (Figure 19g and h).[220, 221]

In order to assess the dynamics of the EDL under a periodically applied potential, we consider the time scale required for 'charging' an EDL - the so-called 'RC' time scale, $t_{RC} \sim \lambda_D L/D$, in which λ_D is the Debye length, characterizing the distance over which the EDL is formed, L is the distance between the electrodes and D is the diffusivity of the ionic species.[222] Comparing this time scale with that of the applied

oscillations, the inverse of the frequency, produces a dimensionless parameter - $\tau = \omega\lambda_D L/D$. When $\tau >$ 1,

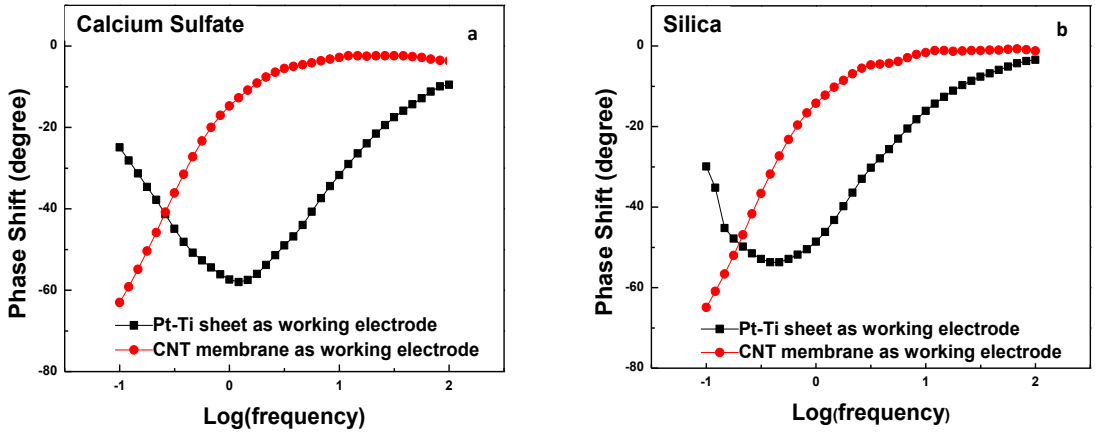

Figure 24: Phase shift versus frequency with a highly conductive metal plate (Pt-Ti) as the working electrode (black) and CNT membrane as the working electrode (red) for (a) CaSO4, and (b) silicate solution.

phase-lags are observed between different regions of the EDL as it responds to the oscillating force.[223] Furthermore, it has been recently shown that if there is a diffusivity mis-match between ionic species, the symmetry breaks down and a long-range, time-averaged electric field is established.[224]

Under the conditions prevailing in our experiments, $\tau \ll 1$, meaning that the EDL is quasi-static and responds instantaneously to the change in potential. In this case, the disruption to the scale formation process is unlikely to be caused by a reduction of the concentrations below supersaturation. Rather, we hypothesize that the shift in local ionic composition during the polarity switch reduces the co-location of anions and cations to a time scale small enough to minimize the formation of the pre-nucleation clusters. These ideas are motivated by our experimental data that show a dramatic decline in scaling when an AC potential is applied to the membrane, as well as SEM micrographs that show far less crystal formation on the membrane surface under AC conditions. This is further supported by experimental evidence showing that pre-nucleation clusters form over a time-scale in the order of seconds under supersaturated conditions; hence, when the electrophoretic motion is sufficiently frequent (i.e., the membrane polarity is switched at a high enough frequency), anions and cations will not be co-located for the amount of time necessary to induce the formation of these pre-nucleation clusters.

Based on this hypothesized mechanism, and the diffusivity mis-match present in our system, it would seem that higher frequencies would lead to better performance (moving away from the quasi-static regime). Higher frequency would cause more rapid mixing of ions and should be more effective at preventing colocation of scale forming ions. However, in our experiments, we clearly observed increased fouling when operating at 10 Hz vs. 1 Hz (Figures 21 and 23). In an attempt to understand this discrepancy, we conducted EIS measurements to determine the capacitive behavior of the conducting membranes under different applied frequencies (Figure 26). In Figure 26, the phase shift vs. the applied frequency (i.e., a Bode plot) is displayed for the ECMD and a Pt-coated Ti sheet as working electrodes in both the $CaSO_4$ and silicate feed solutions. In EIS measurements, a negative phase shift indicates capacitive charging of the EDL.[225] When no phase shift is measured, this typically means the system is acting more like a resistor. When the ECMD membrane was used as the working electrode in the $CaSO_4$ solution, the phase shift was -2.8° and -3.6° at 10 Hz and 100 Hz, respectively; in the silicate solution, the phase shift was -1.6° and -1.2° at 10 Hz and 100 Hz, respectively. These values are very low and indicate that at these frequencies, little capacitive charging is taking place, and the ECMD material is functioning primarily as a resistor, with little EDL formation. However, at 1 Hz, the phase shift was measured to be -14.7° and -14.2° for the $CaSO_4$ and silicate solutions, respectively. These larger phase shift values indicate that the material is indeed acting more like a capacitor with an EDL associated with it. This could possibly be due to the relatively high electrical resistance of the ECMD (228±14 ohm/square), which was preventing effective charge distribution across the membrane surface, which prevented the formation of a robust EDL when high frequencies were applied. To test this hypothesis, we performed identical EIS measurements using a Pt-coated Ti sheet as a working electrode (Figure 26); the Pt-coated Ti had a very low sheet resistance ($8X10^{-4} \pm 9.6X10^{-5}$ ohm/square), and thus, we anticipated that this material would express capacitive charging at higher frequencies. Indeed, when the highly conducting material was used, a large phase shift (-31.7°) was observed at 10 Hz (in the $CaSO_4$ solution), with a larger shift (-57.4°) at 1 Hz. Similar behavior was observed in the silicate solution. While not a perfect comparison (the solid metal sheet is not identical to a porous CNT electrode, which can impact the way ions interact with the surface, and would require different circuit elements when constructing

equivalent circuits to describe these systems), this comparison is meant to illustrate the impact of conductivity on capacitive charging. Therefore, we conclude that the poor anti-scaling performance observed at 10 Hz using the ECMD material is a result of the material's inability to effectively distribute charge throughout its surface at this frequency (due to the short period of time before polarity is switched). This ineffective charge distribution will prevent the EDL from fully forming and be unable to influence the ions to move within the CP layer. This results in poor electrophoretic mixing. However, if a membrane material with a lower resistance could be fabricated, we anticipate that higher operating frequencies would yield better anti-scaling performance due to the fact that a more conductive membrane material would enable faster charge distribution through the surface, allowing the EDL to fully form before the potential is switched. In our system, due to poor conductivity and charge distribution, there is a reduced driving force for the ions in solution to respond to the applied potential, due to the incomplete formation of the electric field (as a result of inefficient charge distribution).

3.3.7 Economic analysis

The proposed ECMD system has the potential to enhance membrane lifetime (by scaling mitigation), reduce membrane cleaning frequency, minimize pretreatment requirements, and reduce the volume of brine that requires disposal (by enhancing water recovery). The additional costs of this process (over conventional MD processes) are associated with fabricating the conductive CNT/PVA composite (cost of materials and fabrication), and energy requirements for the application of the electrical potential. In this section, we consider only the additional capital and operating costs incurred, and potential savings offered, by our process, without considering costs associated with membrane system design, heating of the feed solution, or pumping and cooling of the permeate stream, as these are expected to be comparable with conventional MD processes.

The cost of COOH-functionalized multi-wall CNTs used here is \$0.6 g^{-1}. A single piece of membrane being coated (16 cm X 30 cm or 0.048 m^2) requires 0.2 g (200 ml of 1 g L^{-1} CNT solution), resulting in a

requirement of 4.17 g CNT m^{-2}, which translates to a cost of \$2.5 m^{-2}. A mathematical model for the design and fabrication of polymer solar cells by spray coating has been used to estimate the thermal cost of spray coating a CNT solution on to the membrane.[226] With an assumed substrate speed of 0.15 m s^{-1} and a nozzle-substrate distance of 0.3 m, for a 1 g L^{-1} solution of CNT, the thermal cost of spray coating (which dominates over other electric costs) was \$2 m^{-2} per layer. The total additional cost of membrane fabrication is therefore \$2 + \$2.5 = \$4.5 m^{-2}. Assuming a flux of 30 LMH and an operation time of 20 hours a day and 360 days a year, the water treated over this five-year period is 1080 m^3 m^{-2}. This results in an additional cost of \$0.004 m^{-3}.

The power required to apply 2 $V_{AC,\ 1\ Hz}$ was calculated using Equation 42:

$$P = \frac{V\text{^}2}{Z} cos\theta \qquad \textit{Equation 42}$$

where V is the voltage applied (2 V), Z is the impedance measured from EIS data and θ is the phase shift. The impedance of the system was determined to be 191 Ω for the $CaSO_4$ solution and 182 Ω for the silicate solution. Using Equation 2, it was determined that the power requirements were 0.02 W for both solutions (for the 0.004 m^2 piece of membrane). This results in a power requirement of 5 W m^{-2}. Over the five-year period being considered, power requirements are 180 kWh m^{-2}. Assuming electricity to cost \$0.12 per kWh, the resulting cost is \$21.6 per m^2, which for 1080 m^3 of treated water results in \$0.02 per m^3. Thus, the total additional costs incurred are \$0.004 per m^3 (membrane fabrication) + \$0.02 per m^3 (electrical potential applied) = \$0.024 per m^3 water produced. In terms of savings, these costs need to be compared to the cost of anti-scalants and brine disposal, which vary depending on the physical location and the chemical composition of the water requiring treatment.

3.4 Conclusion

In summary, an effective anti-scaling method was developed, which significantly reduced the occurrence of $CaSO_4$ and silicate scaling on ECMD membrane surfaces. When an electrical potential was applied to the membrane surface, the occurrence of mineral scaling could be greatly reduced, with the

frequency of the applied potential having a dramatic impact on the scaling rate. In our experiments, AC conditions performed better than DC conditions due to the mixing within the EDL. We hypothesize that this reduces the opportunity for anions and cations to co-exist in the same space under supersaturated conditions, and prevents them from forming pre-nucleation clusters needed to form larger crystals. We identified 2 $V_{AC,1Hz}$ as the optimal electrical condition that minimized both $CaSO_4$ and silicate scaling to the largest extent. While we expect that higher frequencies will improve the performance of the system, the relatively poor electrical properties of our conducting membrane limited the capacitive charging behavior to relatively lower frequencies. Improving the membrane's conductivity is expected to allow higher operating frequencies, which should improve anti-scaling performance. Over a five-year period, power requirements are 180 kWh m^{-2} for this treatment process. An economic analysis (details in the SI) indicated that the additional costs associated with the optimal anti-scaling performance are \$0.024 per m^3 of water produced. In terms of savings, these costs need to be compared to the cost of anti-scalants and brine disposal, which vary depending on the physical location and the chemical composition of the water requiring treatment.

Acknowledgements:

This work was undertaken in collaboration with the U.S. Department of Energy's National Renewable Energy Laboratory (NREL) with funding under subcontract AEJ-9-82309-01, and prime contract DE-AC36-08GO28308. In addition, the work was supported by the National Science Foundation CAREER Award (1553756). We would like to thank Steven Bustillos and Gaurav Sant for their help with XRD measurements.

Chapter 4: Lowering the Activation Energy of the C-F bond by Potential-Driven Direct Electron Transfer Facilitates the Reductive Defluorination of Perfluorooctane Sulfonate (PFOS)

Abstract

The wide-spread environmental occurrence of per- and polyfluoroalkyl substances (PFAS) has attracted significant regulatory, research, and media attention because of their toxicity, recalcitrance, and ability to bioaccumulate. Perfluorooctane sulfonate (PFOS) is a particularly troublesome member of the PFAS family due to its immunity to biological remediation and radical-based oxidation. In the present study, we present a heterogeneous reductive degradation process that couples direct electron transfer (ET) from surface-modified carbon nanotube electrodes (under low potential conditions) to sorbed PFOS molecules using UV-generated hydrated electrons without any further chemical addition. We demonstrate that the ET process dramatically increases the PFOS defluorination rate while yielding shorter chain (C_3-C_7) perfluorinated acids, and present both experimental and ab-initio evidence of the synergistic relationship between electron addition to sorbed molecules and their ability to react with reductive hydrated electrons. Because of the low energy consumption associated with the ET process, the use of standard medium-pressure UV lamps, and no further chemical addition, this reductive degradation process is a promising method for the destruction of persistent organic pollutants, including PFAS and other recalcitrant halogenated organic compounds.

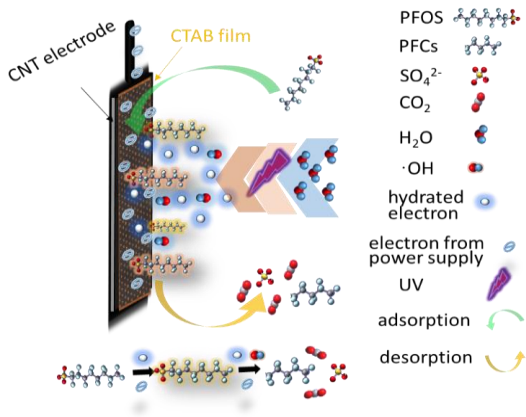

Figure 25: Graphical representation of the process

4.1 Introduction

Perfluorooctane sulfonate (PFOS), which was widely used in fire-suppressing foams and in the manufacturing of water repellent fabrics and stain repellents, has been demonstrated to be a human carcinogen and having adverse effects on the immune system.[227] Because of its widespread use, it has entered the environment through multiple routes: airborne dust[228], landfill leachate[229], and wastewater.[230] In addition to its toxicity, the extreme recalcitrance of this compound (e.g., it is virtually immune to microbial degradation), coupled with its rapid transport through the environment, and tendency to bioaccumulate[231], has led to the detection of PFOS in air[232, 233], soil[234], surface water[235-237], groundwater[235, 238], as well as in multiple animal species[239, 240], and humans.[241] PFOS is part of the larger per- and polyfluoroalkyl substances (PFAS) family, which contains many fluorinated surfactants.[242] Chemical oxidation methods, including hydroxyl radicals, are not effective at degrading PFOS, making it particularly challenging to remove.[243] The elevated stability of PFOS stems from its weak polarization, thermal stability (C_2H_5–H of 101 kcal/mol vs. C_2F_5–F of 127 kcal/mol, and CF_3–CF_3 of 99 kcal/mol vs. CH_3–CH_3 of 89 kcal/mol) and oxidative resistance ($F + e^- \rightarrow F^-$, $E^0 = 3.6$ V).[113, 244, 245] To date, very few methods have been identified that can destroy this molecule; these methods include electrooxidation at high current densities[101] using specialized electrodes[246], incineration[247], sonolysis[229], and reduction via hydrated electrons.[248, 249] The standard method of treatment used to remove PFOS from water is adsorption on activated carbon[250]; in addition, it has been shown that nanofiltration membranes can remove this molecule.[98, 251] However, these removal methods do not destroy PFOS, and subsequent treatment is still needed.[252]

UV-based degradation methods are widely used to destroy organic contaminants in water.[253] However, the destruction of PFOS by UV alone (with low- or medium- pressure mercury lamps) at room temperature is very slow (10 days, 48% defluorination).[254] The mechanism responsible for PFOS

degradation under UV irradiation is believed to involve the generation of hydrated electrons (h_e), produced from the ionization of water by sufficiently energetic photons (Equation A)[255]. The high reduction potential of h_e allows them to reduce the C-F bond ($E^{\theta}_{e} = -2.87$ V; $E^{\theta}_{C\text{-}F} \leq -2.7$ V).[245] However, the high reactivity of the h_e (coupled to the low number of sufficiently energetic photons generated from medium pressure UV lamps) leads to many competing side reactions (e.g., Equations B and C), which lead to the slow defluorination rates observed in pure UV systems[256]. Studies have indicated that the lifetime of h_e in solution is approximately 10^{-7} sec, with a diffusion pathway < 2 nm. Thus, strategies to increase the effectiveness of h_e include the elimination of competing side reactions, increasing the number of h_e, and increasing the probability of reaction between h_e and target molecules. Increasing the h_e yield has been demonstrated by adding compounds such as sulfite[249] and iodide[113], while competing reactions can be eliminated through the addition of hydroxyl radical scavengers, increasing pH, or eliminating dissolved O_2.[112, 255] However, the addition of chemicals to water usually requires further treatment to remove these impurities, depending on the water's intended use.[257]

$$2H_2O + h\nu \rightarrow OH\cdot + H_3O^+ + h_e \qquad \text{(A)}$$

$$OH\cdot + h_e \rightarrow OH^- \qquad k=3.0\times10^{10}\ M^{-1}s^{-1} \qquad \text{(B)}$$

$$H^+ + h_e \rightarrow H\cdot + H_2O \qquad k=2.3\times10^{10}\ M^{-1}s^{-1} \qquad \text{(C)}$$

To the best of our knowledge, strategies to increase the reaction rate of hydrated electrons with target molecules (without changing environmental conditions, such as temperature), have not been explored. Developing such strategies could enable the effective degradation of recalcitrant compounds without the need for chemical additives or energy intensive degradation processes. One such strategy for PFAS involves the lowering of the activation energy of the C-F bond. While there have been reports on catalytic processes capable of facilitating the defluorination of aromatic fluorinated compounds[258], no such catalysts have been identified for aliphatic species. An alternative method to lower the activation energy of these bonds involves the "priming" of target molecules through direct electron transfer (ET); in this

method, an electron is forced onto the target molecule, without leading to the dissociation of any chemical bonds.[109] The driving force for this ET can be provided through a potential difference between the surface of a cathode and a sorbed target molecule (such as PFOS).[259] If the potential difference is large enough, and there is sufficient energy in the system, the receiving entity can dissociate, leading to bond cleavage.[109] However, if there is insufficient energy in the system, the electron can return to the "donating" entity (i.e., the system relaxes).[260] When the electron transfers to the "receiving" entity, the entity assumes excess charge and forms a transient radical anion; in this state, chemical bonds in the receiving entity destabilize due to a perturbation of the entity's electron density.[261] Thus, in this state, additional external energy input, e.g., from a hydrated electron, can lead to bond dissociation. ET between molecules sorbed onto a conductive surface can be initiated through the application of an electrical potential to this surface.[262]

Here, we show that potential-induced ET processes can dramatically increase the defluorination rate of PFOS molecules by UV-generated h_e in an additive-free system. Importantly, the ET reaction is performed at low cell potentials, which reduces energy consumption in the system. The defluorination reactions are explored under different electrode surface chemistries, aqueous constituents, and applied potentials. The degradation products, defluorination, and desulfonation rates are characterized, and density functional theory (DFT) is used to explore the impact of electron addition to the PFOS molecule in terms of bond lengths and the C-F and C-S bond activation energies. Our results demonstrate how the specific adsorption of PFOS onto electrodes with tailored chemical properties can facilitate ET between the electrode and the adsorbed PFOS, which enables UV-generated h_e to rapidly defluorinate PFOS. To the best of our knowledge, this is the first study to demonstrate the coupling of electrochemically-induced ET to photo-assisted degradation reactions, which increases the degradation rate of aqueous recalcitrant organic contaminants. The results of this study open the door to a new, energy efficient degradation pathway that is expected to simplify the destruction of PFAS and other halogenated and recalcitrant organic contaminants.

4.2 Materials and methods

PFOS, sodium perchlorate, cetyl trimethylammonium bromide (CTAB), tetradecyl trimethylammonium bromide (TDTAB), benzethonium chloride (BZT), sodium dodecylbenzene sulfonate (DDBS), and Triton X-100 were purchased from Fisher Scientific. Perfluorooctanoic acid (PFOA) (96%, Sigma Aldrich), heptafluorobutyric acid (98%, Sigma Aldrich), perfluoroheptanoic acid (98+%, Alfa Aesar), perfluorohexanoic acid (97%, Oakwood Chemical), n-perfluoropentanoic acid (97%, Matrix Scientific), and pentafluoropropionic acid (98%, Matrix Scientific) were used for degradate identification and analysis.

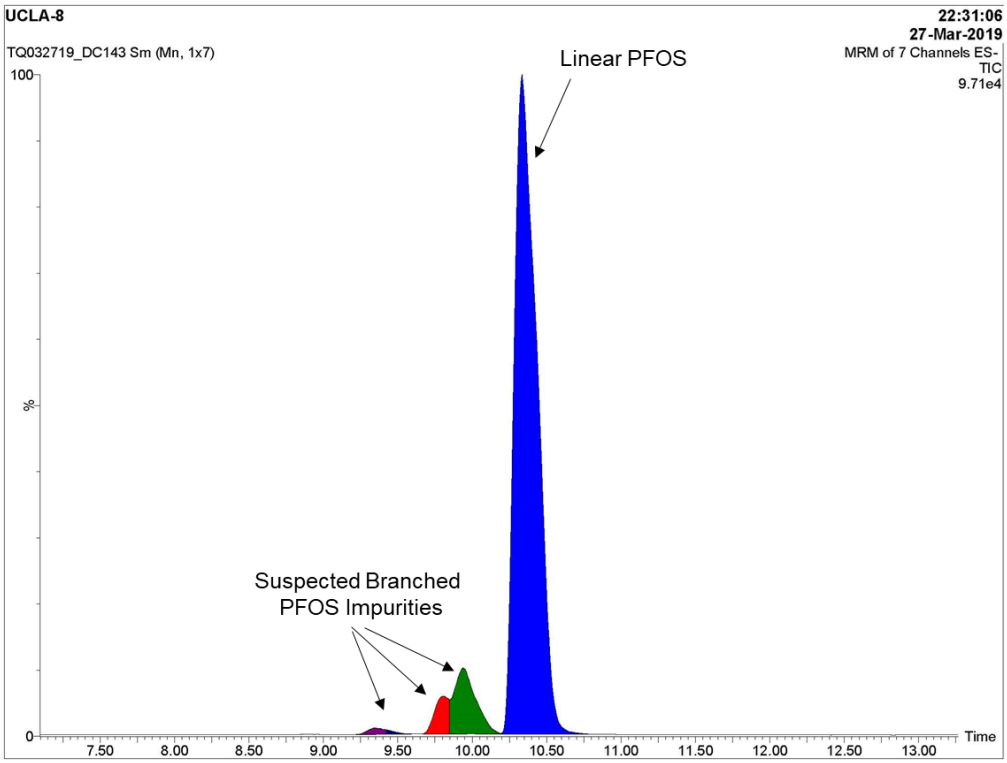

Figure 26: Total Ion Chromatogram (TIC) revealing species with the same mass of linear chain PFOS. The analytical method used to obtain this chromatogram is that described in the main text for analysis of PFOS degradation products, all of which eluted at earlier retention times. No other impurities were observed in our analysis of PFOS stock solutions.

COOH-functionalized carbon nanotubes (CNTs) with a purity of >99% (by weight) were purchased from Cheap

Tubes Inc. (Vermont, US). Total ionic strength adjustment buffer II (TISAB II) solution for F^- ion measurement was purchased from Sigma-Aldrich (Missouri, US).

Despite assurances from the supplier, LCMS analysis (described below) of PFOS stock solutions revealed the presence of minor impurities with the same mass of PFOS (Figure 28). Based on prior reports, we assumed these to be branched chain variations of PFOS. From our analysis and assuming the LCMS response of these impurities was equivalent to PFOS, we estimate these impurities comprise ~13% (by mass) of total organofluorine mass in our initial PFOS stock solutions.

The electrode materials used in this study were graphite plates, Pt-coated titanium shims, and CNT stabilized with different surfactants and deposited on a porous polymeric substrate. For CNT-based electrodes, 0.1 g of COOH-functionalized CNTs were suspended in 1 L of deionized water along with 0.5 g of the surfactant as a dispersion agent. This solution was sonicated with a probe sonicator for 30 minutes, followed by centrifugation for 20 minutes at 11,000 rpm, to produce a dispersed CNT solution. 450 ml of this solution was pressure deposited on a porous polysulfone support (PS 35; Solecta, Oceanside, CA) at 50 psi. The material was then washed with 1 L of deionized water to remove non-attached surfactant and dried at 90 ^{0}C for 10 minutes. This material had a CNT layer with an average thickness of 6 μm (typical resistance of 50～100 Ω/cm), and was cut to the required electrode surface area.

Stock solutions of 500 ppm of PFOS and 1 M of sodium perchlorate in DI water were prepared to make the experimental solution, which contained 5 ppm PFOS in 50 mM sodium perchlorate in deionized water. A medium pressure UV lamp (450 W, Hanovia), UV enclosure, power supply and quartz glass water jacket were purchased from ACE glass Inc. (New Jersey, US). 600 ml of solution was placed in a customized glass beaker (glass shop at University of California, Los Angeles) with a stir bar. This beaker was placed on a stir plate and the UV lamp, sitting in the quartz water-jacket (cooling water flow rate of 240 ml/min), was immersed into the beaker with PFOS solution. Electrodes were suspended in the

solution using alligator clips, and 0, 1, 2 and 3 V cell potential (corresponding relative potentials of +0.03, -0.19, -0.58 and -1.25 V *vs.* Ag/AgCl) were applied using a DC power source. After allowing a 15-minute warmup time for UV light, 5 ml samples were collected every 30 minutes. All experiments were carried out in open air conditions.

Fluoride measurements were done using an ion selective electrode purchased from Thermo Fisher. 2 ml of the sample was added to 2 ml of the TISAB II solution and the probe was immersed into this solution to measure fluoride concentrations. 0, 0.019, 0.095, 0.19, 1.9, 19, and 190 ppm F^- standard solutions were used to calibrate the probe before sample analysis at every time point to verify probe accuracy. pH was measured using a pH probe (Thermo Fisher). Ion chromatography (Dionex, Thermo Scientific, MA, US) was used to measure sulfate concentrations. XPS analysis (Kratos AXIS Ultra DLD, Manchester, UK) of the electrode surface was used to determine the presence of sorbed species, where the electrodes were soaked in the PFOS solution for 30 minutes and then gently rinsed with DI water prior to analysis.

PFOS and PFOS degradation products were quantified by using a Waters Acquity TQD, which is a triple quadrupole mass spectrometer with ultra-high-pressure liquid chromatograph (UPLC) (Waters Acquity UPLC H Class). The UPLC was performed using a Water Acquity BEH C18 column (2.1 x 50 mm, 1.7 µm). The mobile phases used for the UPLC separation were 10 mM Ammonium Acetate, pH 5 (Solvent A) and 10 mM ammonium acetate in 80:20 Methanol/Water (Solvent B). The gradient initially started at 50% B and held for 1 minute, then increased to 85% B over 8 minutes and held there for 3 minutes. The flow rate used was 0.3 mL/min and the injection volume was 10 µL. Negative electrospray ionization with a cone voltage of 20 V was used to form (M-H)- ions of each compound. Multiple reaction monitoring (MRM) scanning was used on the TQD to detect each degradation product. Waters MassLynx 4.1 software was used for data collection and QuanLynx for quantitative analysis.

Commercial standards were used to identify PFOS degradate retention times from product mixtures and to generate the MRM transitions that were used in degradate analysis. PFAS standards for LCMS were

prepared by first dissolving about 6.25 mg of the PFAS chemical in DI water to get around 250,000 ppb solutions, then diluting from those stocks to get 1,000 ppb solutions. Appropriate volumes of each 1,000 ppb solution of each PFAS chemical were then mixed and diluted to obtain a range of mixed chemical standard solutions across the calibration range from 5 to 100 ppb.

4.3 Results

4.3.1 Defluorination of PFOS under oxic conditions

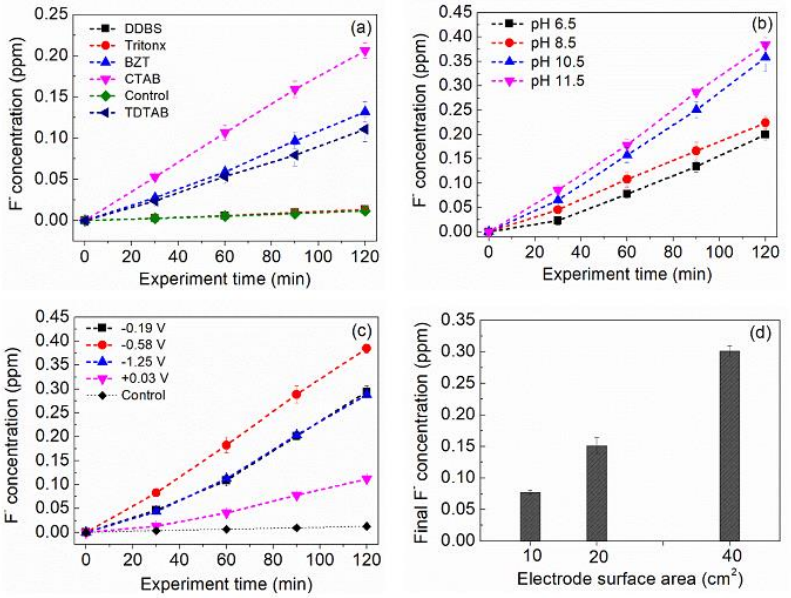

Figure 27: (a) Impact of different CNT surfactant stabilizers on defluorination of PFOS (UV + -0.58 V vs. Ag/AgCl at pH 6.5 with 50 cm2 electrode surface area; Control = no electrode); (b) impact of initial pH on defluorination (CNT/CTAB cathode with 50 cm² electrode surface area, -0.58 V vs. Ag/AgCl, UV); (c) impact of applied potential on PFOS defluorination (CNT/CTAB cathode with 50 cm² electrode surface area, UV, pH 11.5; Control = no electrode); (d) impact of CNT/CTAB cathode surface area on PFOS defluorination (UV, -0.58 V vs. Ag/AgCl, pH 11.5).

While UV-generated h_e alone are able to defluorinate PFOS, the defluorination rate is very slow, with only 0.012 ppm (0.63 μM) F^- (0.4% defluorination) generated after 2 hours of exposure (control experiment in Figure 29a). To test the UV-electrochemical system, we tested a Pt-coated titanium (Ti) plate and a graphite sheet as cathodes (with a Pt-coated Ti plate as anode), and found that the defluorination rate showed no clear improvement after applying 2 V. Since CNTs are excellent current collectors, as well as capable of sorbing contaminants, we used percolating networks of CNTs, deposited

on a polymeric support, and functionalized them with different surfactants as sorption sites/electrodes with the goal of facilitating ET between the current collector and sorbed contaminants.[191] Here, surfactants with different structure and functional groups were used to stabilize aqueous suspensions of CNTs, which were subsequently deposited on the support; the hydrophobic tail of the surfactant tethers these molecules to the CNT backbone through hydrophobic interactions, with the charged hydrophilic head capable of potentially functioning as ion exchange sites for the target molecules.[193] These electrodes were immersed in a PFOS solution and a -0.58 V *vs.* Ag/AgCl (2 V cell potential) was applied to the CNT electrode (functioning as a cathode against a Pt-coated Ti anode). A marked increase in F^- concentration was observed when the cationic surfactant CTAB was used as the CNT stabilizer [F^- of 0.21 ppm (11.05 μM) after 2 hours, or 7.33% defluorination at a defluorination rate of 0.10 ppm/h (5.26 μM/h)] (Figure 29a). Similarly, when the cationic surfactants TDTAB and BZT were used to stabilize the CNTs, enhanced defluorination was observed, but to a lesser extent [F^- of 0.11 ppm (5.79 μM) and 0.13 ppm (6.84 μM) after 2 hours, representing 3.67% and 4.33% defluorination, respectively] (Figure 29a). However, CNTs stabilized with the anionic surfactant DDBS or the non-ionic surfactant Triton X-100 did not show any accelerated defluorination (Figure 29a).

Protons are effective scavengers of h_e (Equation C). Thus, it is expected that a drop in proton concentrations will reduce competition for h_e, increasing their availability to react with the sorbed PFOS on the cathode. We investigated the impact of initial solution pH on PFOS degradation on a CNT/CTAB cathode with -0.58 V vs. Ag/AgCl applied to its surface (Figure 29b). As expected, increasing the pH of the solution from 6.5 to 11.5 increased the final F^- concentration from 0.21 ppm to 0.38 ppm (Figure 29b), and the defluorination rate rose from 0.10 ppm/h (5.26 μM/h) to 0.19 ppm/h (10.27 μM/h). Even though the change in proton concentrations explored in these experiments was exponential, the increase in defluorination rate was not. Thus, while the solution pH is important, it is not the governing factor in determining defluorination rates.

The impact of the applied potential on PFOS defluorination rates using CTAB-functionalized CNT electrodes was also investigated (Figure 29c). By applying 0 V, 1 V, 2 V, and 3 V cell potentials (with CNT electrode as cathode), the relative potential (*vs.* Ag/AgCl) of the CNT/CTAB electrode was +0.03 V, -0.19 V, -0.58 V, and -1.25 V. The current density under these conditions was 0.0166 μA/cm^2, 0.0038 ± 0.0002 mA/cm^2, 0.056 ± 0.002 mA/cm^2 and 0.1152 ± 0.004 mA/cm^2, respectively. At cell potential ≥ -0.58 V vs. Ag/AgCl, increasing the cell potential (and current density) enhanced the defluorination rate from 0.15 ppm/h (7.83 μM/h) to 0.19 ppm/h (10.27 μM/h). Critically, at 0 V (i.e., CNT/CTAB electrode immersed in the solution with no external potential applied), the CNT/CTAB had a potential of +0.03 V *vs.* Ag/AgCl, and we observed an increased defluorination rate from 0.006 ppm/h (0.30 μM/h) (the control with no electrode present) to 0.057 ppm/h (3.02 μM/h). However, when -1.25 V *vs.* Ag/AgCl (3 V cell potential) were applied to the CNT/CTAB electrode, the defluorination rate declined from 0.19 ppm/h (10.27 μM/h) to 0.15 ppm/h (7.75 μM/h) while the final F^- concentrations declined from 0.39 ppm (20.52 μM) to 0.29 ppm (15.26 μM) (Figure 29c). Cyclic voltammetry (CV) measurements using the CNT/CTAB as a working electrode showed that the onset of electrolysis occurs at -0.30 V *vs*. an Ag/AgCl reference. At -1.25 V *vs*. Ag/AgCl (3 V cell potential), water electrolysis was occurring, which competed with PFOS for electrons. Also, we cannot rule out electrostatic repulsion between the negatively charged PFOS and CNT/CTAB cathode surface since the final F^- concentration after a 2 hour reaction declined from 0.087 ppm (4.58 μM) (CNT/CTAB surface not connected to a counter Pt-Ti counter electrode, UV, pH 6.5) to 0.076 ppm (4.00 μM) when the CNT/CTAB electrode was used as an anode (cell potential of 2 V, UV, pH 6.5). Thus, both the cathodic potential on the CNT/CTAB electrode and the sorption of PFOS on the surface of the electrode are necessary to increase PFOS susceptibility to the h_e attack, which increases the overall defluorination rate.

To determine whether the PFOS defluorination reaction is indeed a surface reaction taking place on the CNT/CTAB electrode, we varied the surface area of the electrode immersed into the PFOS solution (10, 20, and 40 cm^2) (Figure 29d). After 2 hours reaction (UV, -0.58 V *vs*. Ag/AgCl), the final F^-

concentration was 0.08 ppm (4.21 μM), 0.15 ppm (7.89 μM), and 0.30 ppm (15.79 μM), for the 10, 20, and 40 cm^2 electrode, respectively, with concentrations doubling with each doubling of surface area.

4.3.2 Defluorination driven by hydrated electrons

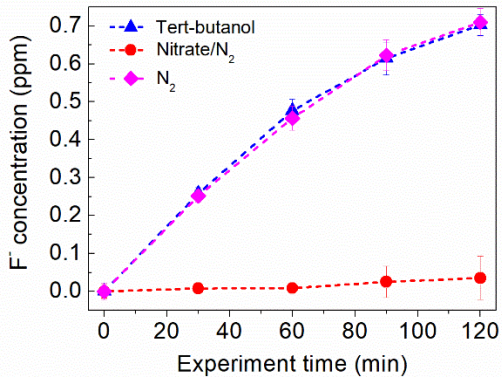

Figure 28: PFOS defluorination in the presence of TB, nitrate, or N2 (UV, -0.58 V vs. Ag/AgCl, pH 11.5)

To explore the role of h_e in PFOS defluorination reactions, we carried out defluorination experiments (CNT/CTAB cathode, UV, -0.58 V *vs*. Ag/AgCl, pH 11.5) with different solution additives (Figure 30). Nitrate is an effective h_e scavenger (1×10^{10} $M^{-1}s^{-1}$)[52]; when 15 mM of nitrate were added, very little fluoride was liberated, which confirms the importance of h_e to the defluorination process. Dissolved oxygen (DO) acts as a highly effective h_e scavenger (Equations E and F). By continuously purging N_2 through the system, DO concentrations were reduced to below 0.1 ppm; once the experiment commenced, defluorination was greatly enhanced , with a final F^- concentration (after 2 hours) of 0.71 ppm (37.37 μM), a nearly two-fold increase over concentrations measured under oxygenated conditions (Figure 30 vs. Figure 29b), with defluorination rates greatly enhanced to 0.46 ppm/h (24.03 μM F^-/h, a 2.34-fold increase over oxygenated conditions). Hydroxyl radicals formed during the UV-induced h_e generation process (Equation A) can scavenge h_e, albeit at a relatively slow rate (1×10^5 $M^{-1}s^{-1}$)[53]. However, since both of these species are co-located during generation, hydroxyl radicals act as potent scavengers. When we added 15 mM of tert-butanol, a known hydroxyl radical scavenger, to the solution, the defluorination rate increased to 0.48 ppm/h (25.08 μM F^-/h) (83 times higher than that in the UV-only system), a result

very similar to the N_2 purging (Figure 30). Together, these results demonstrate the critical part that h_e play in PFOS defluorination.

$e_{aq}^- + O_2 \rightarrow \cdot O_2^-$ k=1.9×10^{10} M^{-1}s^{-1} (Equation D)

$e_{aq}^- + \cdot O_2^- \rightarrow O_2^{2-}$ k=1.3×10^{10} M^{-1}s^{-1} (Equation E)

4.3.3 PFOS removal, desulfonation, and defluorination

The presence of branched chain PFOS impurities complicate our analysis (Table 4) of the rate and extent of defluorination in our experimental systems. Based on the abundance of impurities initially present, and the expectation that these branched species are more easily degraded than linear PFOS, any extent of defluorination less than ~13% may be due to the presence of these impurities. However, there are conditions where we can confidently conclude that defluorination is attributable to the decay of linear chain PFOS. For example, under our most reactive conditions (e.g., UV/2 V, N_2, pH 11.5), analysis of both the linear and branched PFOS over time shows a roughly three-fold greater rate of branched PFOS decay relative to linear chain PFAS (Figure 31). However, because these impurities are not entirely degraded over the 2 h reaction, at most only 11% of the defluorination (when a total of 24% defluorination was observed) observed in these systems can be attributed to the branched chained impurities. Because we were only able to measure decay of the impurities in select experimental systems, we have elected to report rates and extent of defluorination in Table 4 that are unadjusted and do not take into the account the contribution from branched chained impurities. Thus, the defluorination rates reported here should be considered as an upper bound of the rates, reflecting the defluorination of both linear and branched PFOS.

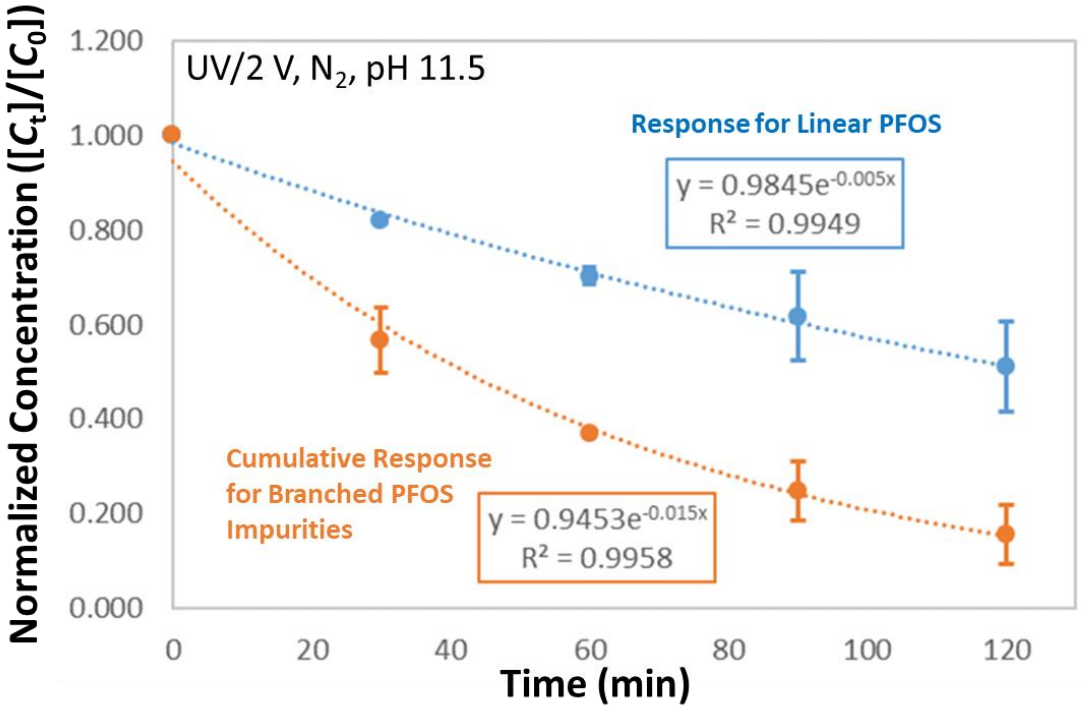

Figure 29: Concentration as a function of time for decay of linear PFOS and branched chain PFOS impurities in the most reactive experimental system (UV/2 V/N_2, pH 11.5). In developing these decay curves, we assumed the LCMS response for branched chained impurities was equivalent to that for linear PFOS. Further, we summed the peak area response for all three impurities that we observed, producing a decay curve for the cumulative mass associated with the presumed branched chain PFOS impurities. Impurities decayed at a rate roughly three-fold greater than linear PFOS. Initially present at ~13% of the total organofluorine mass in our initial PFOS solutions (e.g., t = 0 samples in our reactor experiments with ~5 ppm PFOS), ~16% of the initial impurity mass was present at the conclusion of the experiment after 2 hours. Thus, the amount of impurities present cannot fully account for the extent of defluorination (~24%) reported under these experimental conditions.

In addition to fluoride, sulfate and PFOS concentrations were measured at the end of the 2-hour experimental period. The reaction of h_e and PFOS can lead to the cleavage of the sulfonate group from the PFOS molecule, which transforms to sulfate in water.[112] In general, PFOS removal (defined as the final PFOS concentration divided by the initial PFOS concentration) was greater than desulfonation (defined as the final sulfate concentration divided by the total theoretical sulfate concentration generated after 100% PFOS degradation); desulfonation was nearly always greater than defluorination (defined as the final fluoride concentration divided by the total theoretical fluoride concentration generated after 100% PFOS degradation), except when tert-butanol (the hydroxyl radical scavenger) was added to the

solution (Table 4). When a PFOS solution (pH 11.5) was exposed to medium-pressure UV light, no PFOS or sulfate were removed, and the % defluorination was extremely low (0.4± 0.10%). When a CNT/CTAB/Pt-Ti electrode pair was added to the solution (0 V), desulfonation, and defluorination increased to 57.1 ± 6.2%, and 3.7 ± 0.1%, respectively (Table 4). Upon purging with N_2, PFOS removal, desulfonation, and defluorination increased to 81.0 ± 3.1%, 70.0 ± 3.4% and 6.8 ± 1.0%. When a potential was applied to the electrode pair (-0.58 V vs. Ag/AgCl), these ratios further increased to 86.2 ± 5.9%, 77.8 ± 4.5% and 23.7 ± 1.2%. Interestingly, the addition of tert-butanol did not change defluorination (23.3 ± 0.9%), but desulfonation dropped dramatically (to 24.1 ± 2.2%). At a moderate pH (8.5), desulfonation and defluorination were somewhat lower than at higher pH. Based on the data presented in Table 4, it can be deduced that anaerobic conditions, high pH, and moderate potentials are favorable for both defluorination and desulfonation of PFOS.

Table 4: PFOS removal and degradation performance after 2 hours of reactions under different conditions.

Experiment conditions	**PFOS removal (%)**	**Desulfonation (%)**	**Defluorination (%)**	**Defluorination rate[a] (ppm/h; µM F^-/h)**
$UV^{w/t}$, pH 11.5	/	-	0.4 ± 0.1	0.0057; 0.30
UV/0 V, pH 11.5	NM	57.1 ± 6.2	3.7 ± 0.1	0.05738; 3.02
UV/0 V, N_2, pH 11.5	81.0 ± 3.1	70.0 ± 3.4	6.8 ± 1.0	0.13794; 7.26
UV/2 V, pH 8.5	NM	49.4 ± 9.0	7.5 ± 0.1	0.11362; 5.98
UV/2 V, pH 11.5	NM	73.2 ± 11.2	12.8 ± 0.2	0.19513; 10.27
UV/2 V, N_2, pH 11.5	86.2 ± 5.9	77.8 ± 4.5	23.7 ± 1.2	0.45657; 24.03*
UV/1 V, pH 11.5	NM	47.4 ± 5.6	9.8 ± 0.1	0.14877; 7.83
UV/3 V, pH 11.5	NM	57.6 ± 6.7	9.6 ± 0.4	0.14725; 7.75
UV/2 V, TB, pH 11.5	65.6 ± 7.1	24.1 ± 2.2	23.3 ±0.9	0.47652; 25.08*

1.6.1.1

4.3.4 PFOS degradation pathway and products

Analysis of the products generated from PFOS decay were explored using LCMS for the UV/2V system under N_2 gas at pH 11.5 (from Table 4, PFOS removal of ~86%, desulfonation of ~78% and defluorination of ~24%). Degradates from other photoelectrochemical systems from Table 4 were not explored.

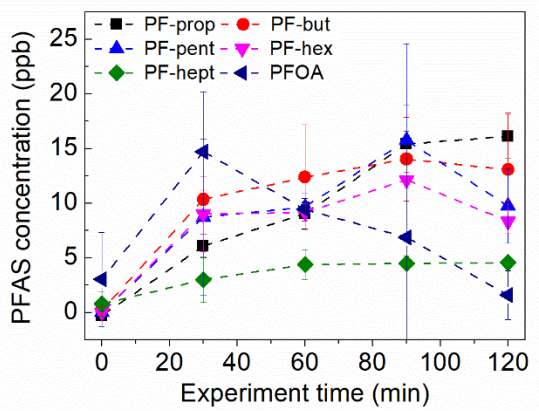

Figure 30: Evolution of PFOS degradation products over time.

PFOS decay occurred concomitantly with the formation of PFOA and several shorter chain perfluorinated acids (Figure 32), the formation of which was confirmed using commercially available standards. PFOA concentration was greatest at our earliest sampling point but steadily degraded over the remainder of the reaction time. At all sampling points, the least abundant degradate was perfluoroheptanoic acid. Perfluorohexanoic and pentanoic acid species accumulated over the first 90 minutes, but their concentrations decreased in the final sampling point. The concentration of shorter chain length perfluorobutyric acid and pentafluoropropionic acid increased monotonically over time, and were present at the greatest abundance at the final sampling point after 2 hours.

The amount of products detected and quantified is far below the initial concentration of PFOS used in these experiments. To assess potential non-reactive mass losses in our electrode systems, we also conducted control studies in the absence of UV light and applied potential to measure the uptake of PFOS

on CTAB functionalized electrode materials. These sorption studies, which were conducted at an identical electrode loading (based on surface area ~0.067 cm^2/mL) to that used in photoelectrochemical systems, revealed some uptake capacity for the electrode materials (2.6 μg PFOS/cm^2 of electrode area). In contrast, DDBS functionalized electrodes did not exhibit any detectable uptake.

We note that no attempts were made to evaluate the relative degree to which degradates sorbed to the electrode surface, such that dissolved concentrations reported in Figure 32 may not reflect the total mass of each species generated from PFOS degradation (i.e., some degradates may remain surface associated). We also did not attempt to identify, via non-target analysis, any previously unidentified PFAS degradates that may have been generated photoelectrochemically under these conditions, which may also explain the difference observed between initial PFOS mass and measured degradate mass.

4.3.5 Modeling the impact of electron addition to PFOS

To explore the impact of ET on the various PFOS bonds, we performed density functional theory (DFT) calculations. To simplify the calculations, we focused only on the impact of additional electrons to PFOS, and neglected other (potentially important) interactions, such as between CTAB and PFOS and CNTs and PFOS. Both the geometries of the native (-1 charge) and excess-charged (-2 charge) PFOS systems were optimized in the presence of a conductor-like polarizable continuum model (PCM) by Tomasi and co-workers,[263, 264] which creates a solute cavity via a set of overlapping spheres to calculate the solvent reaction For the PFOS molecule analyzed in this work, we utilized DFT with the M06-2X functional[265] and the 6-311+G (d,p) basis set. We have specifically chosen this level of theory for our calculations since this functional and basis set has been previously benchmarked for accurate calculations in aqueous chemical systems.[266] To obtain the Gibbs free energies for dissociating the various C–F bonds in both the native and excess-charged PFOS systems, the thermodynamic partition function, q, was calculated to obtain contributions from translational, rotational, and vibrational degrees of freedom from standard statistical thermodynamics formulae at 298 K. With these free energies obtained from the optimized

geometries, we calculated the bond dissociation free energies for each of the unique C–F bonds in both the native and excess-charged PFOS molecules. Based on a molecular orbital density analysis, we attribute this drastic reduction in bond dissociation energy to an anti-bonding C–F orbital, which is populated by the extra electron placed on the PFOS molecule. These results are similar to those reported by Paul et al., (2004), who note that the addition of an electron to aliphatic perfluorinated hydrocarbon (not a surfactant), elongates the C-F bond length; since longer bonds translate to weaker bonds, these results mirror ours. However, one important difference is that the previous study predicts that only a single C-F bond is elongated, while our model predicts that all C-F bonds are weakened. These structural differences are due to the highly-symmetric, constrained geometries that were used in the 2004 study of Paul et al.; in contrast, our DFT geometries and energies were optimized without any symmetry constraints, which allowed the energy of the addition electron to distribute throughout the entire molecular structure, leading to our observed results. Importantly, our DFT calculations do not distinguish the source of the electron, i.e., we do not make any assumption whether the first electron, which transforms PFOS from its native to excess-charged state, originated from the cathode or from a . As such, we do not make any *he* a priori assumption on the order of ET reactions. What we do find, is that cathodic potentials alone (up to -1.25 V vs. Ag/AgCl) are not capable of driving the defluorination reaction. We also find that UV light alone results in very slow defluorination. Our DFT model does show that the C-F bond dissociation energy dramatically drops after the addition of a single electron to PFOS, but that the addition of a single electron to the molecule is not sufficient to break the C-F bond. Thus, in the pure UV system (or UV + sulfite, iodide, etc) the defluorination of PFOS likely requires multiple interactions with PFOS to drive C-F *he* dissociation and PFOS defluorination. field.

For the native system, we obtained strong bond dissociation free energies of ~102 kcal/mol (on average), which reflect the strength of the polar C–F bond (Figure 33). Upon the addition of a single electron to the PFOS molecule (which formed the excess-charged state), we obtained C-F bond dissociation free energies of ~30 kcal/mol (Figure 33), which are significantly reduced compared to its native configuration.

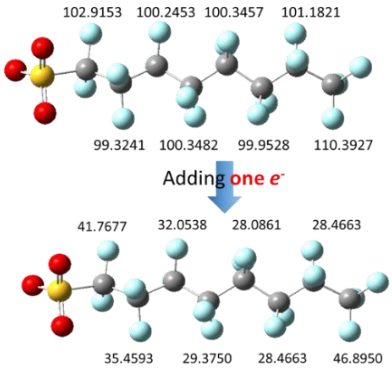

Figure 31: Change of bond dissociation free energy after adding one electron onto native PFOS molecule.

In addition to changes in C-F bonds, we used DFT to explore the bond length of the C-S bond in response to ET. Similar to the C-F bonds, the C-S bond weakens as electrons are added to PFOS. Interestingly, the C-S bond length (a proxy to bond strength, with longer distances pointing towards lower strength[267]) responds rather weakly to the first ET event (increasing from 1.92 $\dot{A}$ to 1.94 $\dot{A}$. However, the addition of a second electron more than doubles the bond length (to 4.22 $\dot{A}$), which strongly suggests bond dissociation.

4.4 Discussion

4.4.1 Enhanced PFOS defluorination on suitably functionalized electrodes

While it known that h_e are capable of defluorinating PFOS, current defluorination methods involve the large-scale production of h_e, typically by exposing the contaminated solution to UV light in the presence of specific chemical additives (e.g., sulfite, iodide). Here, we present, for the first time, a reductive defluorination method that enhances the effectiveness of the h_e by facilitating direct (and likely reversible) ET between the sorbed contaminant and a suitable functionalized electrode. We have demonstrated that the degree of enhancement is dependent on the chemical species attached to the electrode, the applied potential, the surface area of the electrode, and the presence of h_e scavengers (Figure 29).

Based on our experimental observations, it is clear that the first step of the enhanced defluorination process is the effective adsorption of PFOS on the surface of the electrode. Based on XPS analysis, we have shown that CTAB-functionalized CNT electrodes, formed through the sorption of CTAB on CNTs during the CNT suspension preparation process, are the most effective at sorbing PFOS. Other positively charged surfactants (TDTAB and BZT) showed some minor sorption capacity, but negatively charged and neutral surfactant-functionalized CNTs showed no sorption capacity. Clearly, the positive charge of the cationic surfactants facilitates PFOS adsorption to the cathode via favorable electrostatic interactions. We speculate that the slightly longer hydrophobic tail of CTAB, compared to TDTAB (16 carbons in CTAB *vs.* 14 carbons in TDTAB), and the buried nature of the positively charged quaternary ammonium group in TDTAB, allow for more effective PFOS interactions.

It has been demonstrated that after binding with positively charged quaternary ammonium groups, the reactivity of the PFOS-N(NH_4) to h_e increased to 7.3×10^7 $M^{-1}s^{-1}$ from $<10^5$ $M^{-1}s^{-1}$.[244, 268] This improvement was also observed in our experiment: by simply mixing CTAB into a PFOS solution under UV light (pH = 6.5, oxic condition), the final F^- concentration increased from 0.012 ppm to 0.050 ppm. In the absence of an applied potential, some defluorination was observed when a CNT/CTAB surface was immersed in the PFOS solution, when compared to the control (no CTAB in the system). CTAB and PFOS can form complexes/micelles (either in solution or possibly on the surface of the CNT/CTAB electrode), where the positively charged quaternary ammonium group of CTAB interacts with the negatively charged PFOS sulfonate group. Micelle catalysis has been suggested as an efficient way to enhance ET due to the lowered dielectric constant in the vicinity of the micelle surface, and outer-sphere solvent reorganization[269], which can contribute to the large electron-transfer reaction rate increase.[270] A similar observation was made by a study investigating ET between an electrode surface and biomolecules, where CTAB-modified CNT electrodes exhibited elevated ET[64]. However, when we applied a negative potential to the CNT/CTAB electrode, a dramatic increase in the defluorination rate was observed.

Our modeling efforts showed that the addition of a single electron (e.g., from the cathode) to PFOS elongates the C-F bonds throughout the molecule (Figure 33), and reduces the activation energy of these bonds, as well as the C-S bond. When a second electron is added to PFOS (e.g., h_e), C-F and C-S bonds dissociate, which leads to the release of fluoride and sulfate. We hypothesize that the defluorination reaction is a two-step process, where the first step involves ET between the cathode and PFOS, and the second step involves the interaction of PFOS in the excess-charge state with a h_e. However, we do not have direct evidence regarding the order of the ET process, i.e., it is possible the first electron is the hydrated electron and the second electron is from the cathode. Furthermore, while we do not have direct evidence of ET from the cathode to PFOS, our experimental evidence strongly suggests that this indeed is the case. Specifically, we note that the defluorination rate is surface area dependent, with larger areas leading to higher rates, emphasizing the importance of available surface area to the reaction (Figure 29d). Previous experiments on aliphatic perfluorinated carbons (investigating the species CF_4 – C_6F_{14} in the gas phase) have reported that the addition of a single electron to these molecules resulted in dissociative decomposition of the C-F bond only in the smallest molecules (CF_4 and C_2F_6), with larger molecules exhibiting a stable parent anion post electron addition.[106] This was verified computationally, with DFT results showing the formation of a stable anion for larger (C>2) perfluorinated carbon molecules[69]. In fact, the DFT study showed that longer perfluorinated carbons (C>2) show a positive adiabatic electron affinity, indicating that the addition of an electron to these molecules is an exothermic reaction, with longer carbon chains exhibiting larger electron affinities.[271] Since PFOS is negatively charged in its native state (due to the presence of the sulfonate group), it is unlikely that its adiabatic electron affinity is identical to C_8F_{14}. Nevertheless, these previous results support our DFT calculations that show an overall weakening, but not breaking, of the C-F bonds upon the addition of a single electron to PFOS. This lends further credence to our hypothesis that the PFOS defluorination reaction is a two-electron process, which is different than what is typically reported in the literature.[113, 245] Since previous investigations used large amounts of chemical additions to enhance h_e generation (e.g., sulfite, KI), it is possible that the excess

numbers of h_e masked the nature of the defluorination reaction, making it appear as a single-electron process.

Another interesting set of observations noted in previous gas-phase experiments is the strong dependence of the rate of ET on the length of the carbon chain and the energy of the exciting electron.[106, 271] Specifically, longer carbon chains required lower energy electrons to affect a given ET rate, and, for a given molecule, the ET rate peaks at a certain electron energy, with higher energy electrons leading to slower ET rates. Thus, peak ET rates shift to lower energy electrons with increasing molecule size. These observations can potentially help explain our experimental results that show a peak defluorination rate when a cell potential of 2 V was applied, with falling rates at 1 V and 3 V cell potentials. While this is speculative, with our observations potentially explained through enhanced electrostatics and/or gas evolution, it is possible that by tuning the applied potential on the electrode (and through this, the electron energy), it would be possible to target specific contaminants rather than adopting the sledge-hammer approach often encountered in chemical decontamination processes.

Evidence for the second step of the defluorination process (i.e., the involvement of h_e in the reaction) is clear since in the absence of h_e no defluorination is observed (Figure 29c). Moreover, introducing h_e scavengers (nitrate) completely stop the reaction, while the elimination of scavengers (O_2, $OH\cdot$) increases the defluorination rate (Figure 30). Interestingly, scavenging $OH\cdot$, which are co-generated with h_e from the interaction of energetic photons and water (Equation A), not only increases defluorination, but also drastically decreases the degree of desulfonation. This strongly suggests that both $OH\cdot$ and h_e are responsible for the C-S bond schism. While our DFT data does show the potential for C-S bond dissociation when two electrons were added to PFOS, our experimental data shows that the presence of oxidative radicals dramatically increases this event. From a practical perspective, minimizing desulfonation may be advantageous, as sulfonated degradation products are less likely to volatilize, which could increase the overall defluorination of the compounds, as well as minimize the release of volatile fluorinated hydrocarbons.

4.4.2 PFOS degradation pathway

For the conditions at which degradate analysis was explored (UV/2V system under N_2 gas at pH 11.5; PFOS removal of ~86%, desulfonation of ~78%, and defluorination of ~24% - see Table 4), the observed products match those previously reported for the radiolytic degradation of PFOS[71]. Bond dissociation results in loss of the sulfonic acid end group to yield sulfur trioxide (SO_3^-), which is subsequently oxidized to sulfate (SO_4^{2-}), and a presumed perfluoroalkyl radical ($C_8F_{17}^{\bullet}$). Our observed concentration profile for PFOA (i.e., an early concentration maximum and subsequent decay with reaction progress) suggests it is an intermediate to the formation of the lower-order fluorinated acids. Kim *et al.*[71] proposed formation of PFOA via the elimination of HF from perfluoroalkyl alcohol, which they hypothesized to form from the reaction of $C_8F_{17}^{\bullet}$ with $OH\cdot$. Further radiolytic decomposition of PFOA via decarboxylation could then explain the formation of shorter chain perfluorinated acids through sequential loss of CF_2.

Because we are only measuring products at levels (i.e., 10's of ppb) that are far below our initial PFOS concentration (5 ppm), we cannot rule out other loss processes and transformation pathways in our experimental systems. For example, in Table 4, the addition of *tert*-butanol to quench $OH\cdot$ appears to inhibit desulfonation even though removal of PFOS and the overall extent of defluorination was comparable to that measured in systems without *tert*-butanol. We speculate that there may be a parallel reaction pathway for PFOS destruction in our system that proceeds via C-F bond cleavage, as supported by our DFT studies. Such a pathway would be expected to yield products different from those explored analytically herein (i.e., perfluorinated organic acids), and thus, future work will be needed to validate the formation of degradates produced through this alternative transformation route.

4.4.3 Implications for the treatment of contaminated water

From a practical perspective, the main advantages of our proposed degradation process are that it does not require chemical additives, and its relative energy efficiency. A detailed description of the economic considerations and advantages can be found in the Supporting Information.

4.5 Conclusion

Here, we demonstrated an additive-free PFOS degradation method that enhanced the defluorination of PFOS by first "priming" the PFOS molecule through an ET process taking place between sorbed PFOS and a CNT/CTAB electrode (at low potentials). DFT calculations showed that the addition of a single electron to the PFOS molecule reduced the activation energy of the C-F bond by approximately 70%. A second electron, this one generated from UV-induced photolysis of water (i.e., a h_e), upon interacting with the primed PFOS molecule, was able to rapidly defluorinate it. This chemical-free, and energy efficient decontamination method opens the door to a new treatment process that could be used to treat other highly recalcitrant halogenated contaminants, as well as offering a potential to target specific contaminants by tuning the excitation energy of the first electron through careful adjustment of the applied electrochemical potential.

Acknowledgements:

We thank the Strategic Environmental Research and Development Program (ER18-1595) for their generous financial support.

Chapter 5: Structural Dependence of Reductive PFAS Defluorination in a UV/Electrochemical System

Abstract:

Per and polyfluoroalkyl substances (PFAS), legacy chemicals used in firefighting and the manufacturing of many industrial and consumer goods, are now widely found in groundwater resources, along with other regulated compounds, such as chlorinated solvents. Due to their strong C-F bonds, these molecules are extremely recalcitrant, requiring advanced treatment methods for effective remediation, with hydrated electrons shown to be able to defluorinated these compounds. A combined photo/electrochemical method has been demonstrated to dramatically increase defluorination rates, where PFAS molecules sorbed onto appropriately functionalized cathodes charged to low potentials (-0.58 V vs. Ag/AgCl) undergo a transient electron transfer event from the electrode, which "primes" the molecule by reducing the C-F bond strength and enables the bond's dissociation upon the absorption of a hydrated electron. In this work, we explore the impact of head group and chain length on the performance of this two-electron process, and extend this technique to chlorinated solvents. We use isotopically-labeled PFAS molecules to take advantage of the kinetic isotope effect, and demonstrate that indeed PFAS defluorination is likely driven by a two-electron process. We also present density functional theory calculations to illustrate that the externally applied potential resulted in an increased rate of electron transfer, which ultimately increased the measured defluorination rate.

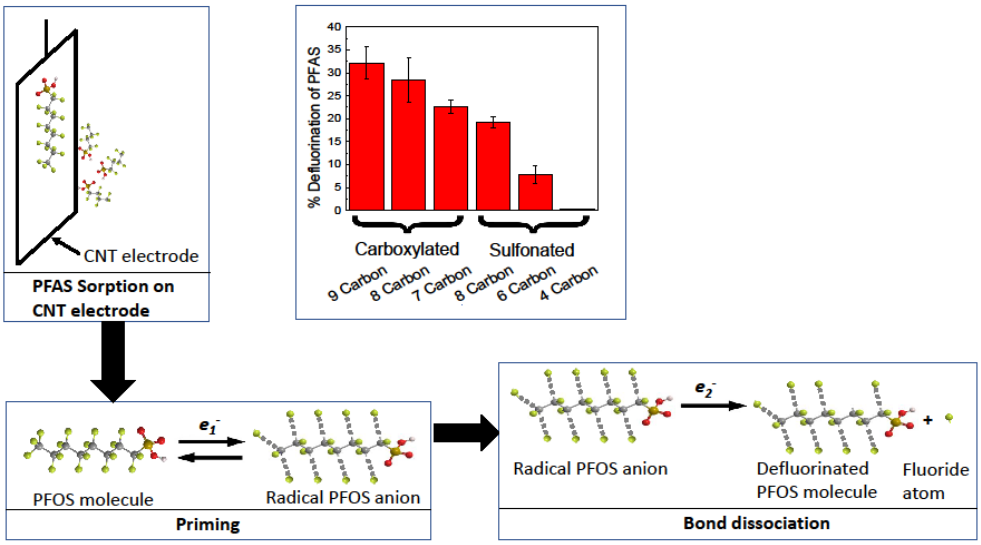

Figure 32: Graphical representation of the process

5.1 Introduction

Groundwater sources provide drinking water to at least 50% of the world's population.[272] However, emerging contamination of per- and poly- fluoroalkyl substances (PFAS), consisting of an aliphatic hydrophobic tail saturated with F atoms attached to a hydrophilic head group, have imposed an increasingly high risk to groundwater supplies due to their toxicity, environmental persistence, and resistance to conventional treatment processes.[231, 273] PFAS contamination is commonly associated with areas where fire suppression, manufacturing, and metal plating activities took place.[235] Often, chlorinated solvents (e.g., cis-dichloroethylene (cDCE), trichloroethylene (TCE) are found as co-contaminants.[274, 275] Chronic exposure to all these contaminants has been shown to have negative effects on the central nervous system, reproductive system, liver and kidney function, as well as causing cancer.[276, 277] The EPA has established health advisory guidelines in drinking water for some of these pollutants: 5 ppb for TCE and cDCE, and 70 ng/L for PFOS and PFOA.[94] Therefore, it is of great importance to develop a suitable technique for the removal of PFAS and chlorinated compounds.

Two commonly found PFAS groups include perfluoroalkyl carboxylates (PFCA), which have a carboxyl group as the hydrophilic head, and perfluoroalkyl sulfonates (PFSA) having a sulfonate group as the head. While chemical oxidation has been successfully used to degrade PFCAs, PFSAs are known to be highly resistant to oxidative degradation.[245] For example, perfluorooctanoic acid (PFOA) (a member of the PFCA group) has been successfully degraded by oxidation with persulfate and hydrogen peroxide.[278, 279] In contrast, advanced oxidation methods using ozone, ozone/hydrogen peroxide and Fenton's reagent have been unsuccessful at degrading perfluorooctane sulfonate (PFOS) (a member of the PFSA group) at the lab scale.[280] Oxidation with potassium permanganate has been effective to some extent, with a PFOS degradation rate of 46.8% when heated to 65^0C.[281] Electrochemical oxidation of PFOS has been shown to be successful. However, high potentials (greater than 5 V) are required, leading to electrode corrosion unless appropriate high-cost anode materials are used, such as boron doped diamond.[102] In addition, the high potentials needed to drive the reaction lead to relatively high energy demands and gas evolution.[282] Direct UV photolysis of PFOS, although successful, has shown a very low rate of defluorination (48% after 10 days).[254] This defluorination is hypothesized to be due to the formation of hydrated electrons generated by the breakdown of water by energetic photons provided by a UV source.[255, 283] Hydrated electrons are sufficiently powerful reducing agents to sever the C-F bond.[248] A common method to increase PFAS degradation is to encourage hydrated electron formation (by adding sulfite or iodide)[114, 249] while ensuring the reactive species are not consumed by competing reactions (with protons, dissolved oxygen and hydroxyl radicals).[256]

A UV/sulfite system achieved 98% decrease in PFOS concentration within 30 minutes, [284, 114] and a UV/iodide system achieved 55% decrease in PFOS concentration after 1.5h .[244, 285] Hydrated electrons are highly reactive and have extremely short lifespans (about 10^{-7}s) with a diffusion pathway of < 2 nm.[245, 256, 286] Competing side-reactions that scavenge hydrated electrons include their reaction with protons, oxygen, and hydroxyl radicals.[256] Thus, to increase the reaction between PFAS and hydrated electrons, different approaches can be used, including increasing the rate of production (sulfite or iodide addition), eliminating

competing scavengers (oxygen, protons, hydroxyl radicals), and increasing the probability of reaction between the hydrated electron and PFAS.

In our previous study, we developed a UV-electrochemical system, capable of effectively defluorinating PFOS through a combination of enhanced adsorption (concentrating PFOS on electrode surface), transient electron transfer (ET) from the electrode to sorbed PFOS molecules, which destabilized the C-F bonds, and reaction with UV-generated hydrated electrons.[111] The degradation process yielded fluoride ions and shorter-chained PFAS. The combined process achieved a defluorination rate of 23 ± 1.2 %, compared to 6.8 ± 1 % when only UV was used. While we demonstrated the process on difficult-to-degrade PFOS, it was unclear whether the process could be used on other recalcitrant contaminants, such as chlorinated organics.

In this study, we explore the ability of the combined UV/electrochemical method to degrade a range of PFAS molecules with different chain lengths and head groups. In addition, we explore the degradation of chlorinated solvents (TCE and cDCE) alongside PFAS. We discuss the impact of head group species and chain length on degradation kinetics. We observed that the enhanced adsorption exhibited by longer-chained PFAS make it easier to degrade compared to their shorter-chain counterparts. In addition, while chlorinated solvents were degraded, the degradation mechanism was independent of the presence of an electrode, and is likely a function of the UV-generated reactive species. Furthermore, by using isotopically-labeled PFOS, we demonstrate that transient electron transfer from the electrode to sorbed PFOS (which destabilizes the C-F bond) is indeed responsible for the enhanced defluorination rates by UV-generated hydrated electrons.

5.2 Materials and methods

5.2.1 Chemicals

Perfluorooctane sulfonic acid (PFOS), perfluorohexane sulfonic acid (PFHxS), perfluorooctanoic acid (PFOA), perfluorononanoic acid (PFNA), perfluoroheptanoic acid (PFHpA), trichloroethylene (TCE), cis-

dichloroethylene (cDCE), sodium perchlorate ($NaClO_4$), tert-butanol (TB) and cationic surfactant cetyl trimethylammonium bromide (CTAB) were purchased from Fisher Scientific. Perfluorobutane sulfonic acid (PFBS) was purchased from Sigma Aldrich. Isotopically labeled and unlabeled PFOS (50 µg/ml dissolved in methanol) were purchased from Cambridge Isotope Laboratory (Tewksbury, MA), COOH-functionalized CNT with purity of >99% by weight were purchased from Cheaptubes (Vermont, USA). Polysulfone (PS-35) membranes which were used as a substrate for the CNT electrode were provided by Tisch (Oceanside, CA). Total ionic strength adjustment buffer II (TISAB II) solution was purchased from Sigma-Aldrich.

5.2.2 Electrode preparation

The working electrode used in this work was composed of a percolating layer of CNTs deposited on a porous polymeric membrane support (PS35, Solecta Inc., Oceanside, CA).[111] For the CNT electrode, 0.1 g CNTs were suspended in 1 L of deionized water along with 0.5 g of a surfactant (CTAB) as a dispersing agent. The solution was sonicated with a horn sonicator (Branson, Danbury, CT) for 30 minutes, followed by centrifugation (Beckman Coulter, Brea, CA) for 20 minutes at 11,000 rpm at 4^0C, to produce a dispersed CNT solution. 450 ml of the solution was pressure deposited at 50 psi onto the membrane (with a surface area of 120 cm^2) using a pressure deposition system. The material was then washed with 1 L of deionized water to remove excess surfactant and dried at 90^0C for 10 minutes. This electrode was cut to the required surface area (40 cm^2) and used without further modification. A platinum coated titanium (Pt-Ti) sheet was used as the counter electrode.

5.2.3 Experimental setup and procedure

The experimental solution was composed of 5 ppm of the chemical being tested together with 50 mM $NaClO_4$ dissolved in DI water. A medium pressure UV lamp (ACE Glass, Vineland, NJ) placed inside a cooling jacket was immersed into the solution. DI water was flowed through the quartz cooling jacket (ACE Glass, Vineland, NJ) to avoid overheating of the UV lamp. Electrodes were suspended in the solution using

alligator clips with a 4 cm separation, with the CNT membrane as the cathode and Pt-Ti sheet as the anode. A DC power supply (Rigol; Oakwood village, OH) was used to power the two electrodes. To eliminate interference from oxygen and protons, N_2 gas was bubbled through the solution, and the solution pH was adjusted to 11.5 using 2.5 N NaOH. 5 ml samples were collected every 30 minutes after allowing a 15-minute lamp warmup time, with the experiment being carried out for two hours. For experiments with TB, 15µl of TB were added to the solution prior to starting the experiment.

In the isotopically labeled PFOS experiments, 1.2 ml of the labelled and unlabeled PFOS were diluted to 12 ml respectively (separately). 1 ml of this solution (5 µg of PFOS) was drop-coated on to the electrode surface and allowed to dry. The electrode was then directly immersed into 600 ml of degassed 50 mM $NaClO_4$ solution. No samples were collected during the experiment. At the end of the two-hour period, the solution was concentrated using a rotary evaporator to a final volume of 30 ml.

5.2.4 Analytical methods and electrode characterization

Fluoride measurements were conducted using an ion selective electrode (Thermo Fisher, Waltham, MA). 2 ml of the sample was added to 2 ml of the TISAB II solution and the probe was immersed into this solution while being continuously stirred. An Orion A320 meter was used to read mV values and the probe was calibrated using standard solutions of known fluoride concentrations. pH was measured using a pH probe (Thermo Fisher, Waltham, MA). Contact angle measurements of the CNT electrode were conducted using a contact angle goniometer (Rame-Hart, model 250, Netcong, NJ). An ion chromatograph (Dionex, Thermo Fisher, Waltham, MA) was used to measure chloride concentrations. Electrode conductivity was measured using a four-point conductivity probe (Mitsubishi MCP T610, Tokyo, Japan). To analyze surface adsorption of target molecules on the electrode, a small piece of the electrode was immersed in the solution for 15 minutes, rinsed, and dried in a vacuum oven at 100°C. The sample was then analyzed using X-ray photo spectrometry (XPS) (Kratos Axis Ultra DLD Spectrometer equipped with a monochromatic Al kα X-ray source, Manchester, UK). Membrane surfaces were imaged using scanning electron microscopy (SEM) (Zeiss Supra 40VP, Carl Zeiss Microscopy, LLC, NY). Samples were secured on SEM stubs using double

sided carbon tape and sputter coated (Ion beam sputtering/etching system, South Bay Technology, San Clemente, CA) with iridium before imaging. Cyclic voltammetry and open circuit potential measurements were carried out using a potentiostat (CH Instruments, Austin, TX) with an Ag/AgCl reference electrode. In these experiments, the PFAS solution was placed in a stirred (250 rpm) beaker with the two electrodes (CNT membrane as working electrode and Pt-coated Ti as the counter electrode) separated by 4 cm. Surface roughness was determined using atomic force microscopy (AFM) (Bruker Dimension FastScan Scanning Probe Microscope, Bruker, Billerica, MA).

5.3 Results and discussion

5.3.1 Electrode characterization

The contact angle of the CNT electrode was $91.4^0 \pm 3.3^0$ (Figure 35a), indicating a somewhat hydrophobic surface. The root mean square of surface roughness, determined using AFM was 35 ± 5 nm (Figure 35b). Figure 35c shows a top view of the CNT-CTAB membrane, where a dense network of CNT can be seen. The high conductivity of CNTs imparts the fabricated electrode with conductive properties, with the sheet resistance of the electrode found to be 21.7 Ω/□. Considering that the CNT layer thickness was 6 μm, the electrical conductivity was found to be 7680 S/m.

The open circuit potential across the working (CNT) electrode and the Ag/AgCl electrode when no cell potential was applied was -0.03 V, and when a cell potential of 2 V was applied, was -0.58 V. Cyclic voltammetry curves showed that some water splitting occurred at a potential of -0.3 V with respect to the

reference electrode. Water splitting is evident by the sudden change in slope at -0.3 V in the current versus voltage curve (Figure 35d).

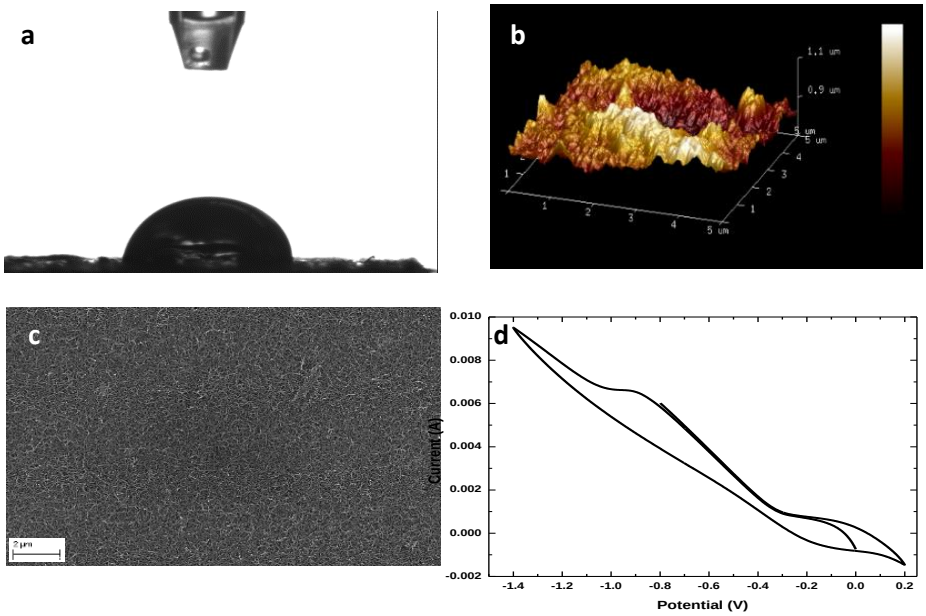

Figure 33: Electrode characterization: (a) Contact angle image indicating a somewhat hydrophobic surface, (b) AFM image indicating a root mean square roughness of 35 ± 5 nm (c) SEM image of electrode indicating uniform CNT network, and (d) CV curve of the electrode immersed In PFOS solution with potential sweep. from -1.4 V to 0.2 V.

5.3.2 Effect of chain length and head group on degradation rate.

In our previous work, we concluded that PFOS degradation by the UV/electrochemical system takes place in a stepwise manner, with the first step involving sorption of the target onto the electrode surface, and the second step involving the transient ET from the electrode to the sorbed molecule driven by the applied potential. This ET step causes a disruption in the electron cloud, which leads to C-F bond elongation and weakening, in effect "priming" these molecules. Meanwhile, in the liquid phase, hydrated electrons are generated through UV photolysis of water; these hydrated electrons can attack the "primed" molecules,

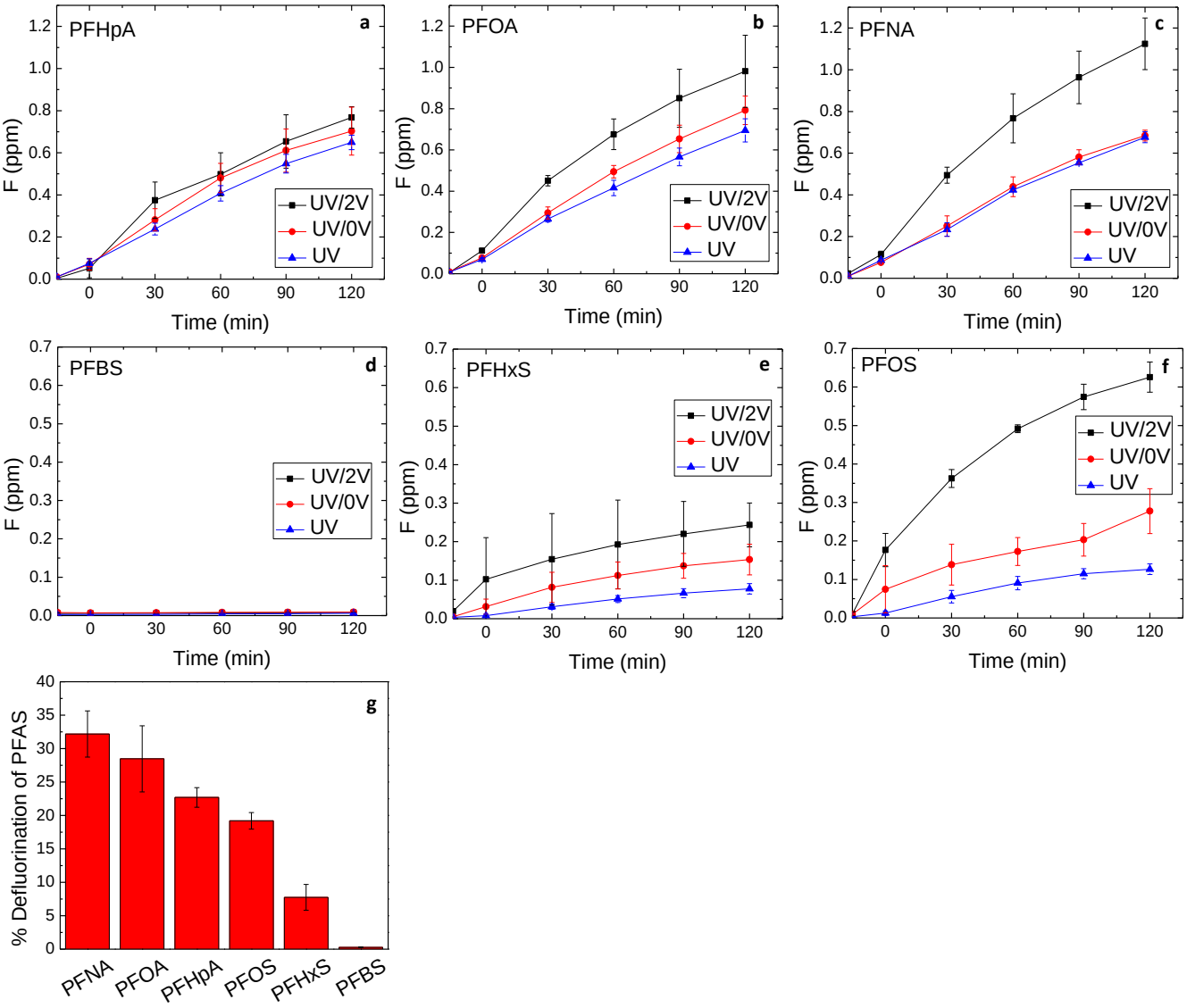

Figure 34: Defluorination of PFAS with different chain lengths under UV/2V, UV/0V and UV-only (i.e., no electrode was present) conditions: (a) PFHpA, (b) PFOA, (c) PFNA, (d) PFBS, (e) PFHxS and (f) PFOS, and (g) % defluorination of six PFAS compounds under UV/2V conditions after two hours of reaction. UV/0V conditions imply that the electrodes were immersed in the solution, but no external potential was applied, while UV implies that no electrodes were present.

leading to dramatically higher defluorination rates. In this section, we report on the degradation rates of PFCA and PFSA molecules with different chain lengths. The PFCA molecules we tested were PFHpA (7 carbons), PFOA (8 carbons), and PFNA (9 carbons), while the PFSA molecules were PFBS (4 carbons), PFHxS (6 carbons), and PFOS (8 carbons).

Reduction by hydrated electrons is an effective method for PFCA degradation.[287] The evolution of fluoride (F) concentrations over time from the degradation of the three PFCAs investigated can be seen in Figures

36a-c, and a comparison of the defluorination rates can be seen in Figure 36g. For PFHpA (7 carbon), the F concentration was 0.64 ± 0.03 ppm after 2 hours with UV-only. Under UV/0V conditions, the F concentrations increased to 0.7 ± 0.11 ppm (a 9.3% increase). However, the error bars for these results do overlap, making the differences not statistically significant (p=0.29 by unpaired t-test). However, when a potential of 2 V was applied, there was a significant increase to 0.76 ± 0.05 ppm (an 18.75% increase over UV-only conditions). For PFOA (8 carbon), degradation under UV-only conditions resulted in a F concentration of 0.69 ± 0.06 ppm after two hours, which increased to 0.79 ± 0.07 ppm (14.5% increase) under UV/0V conditions, not a statistically significant difference (p=0.36 by unpaired t-test). However, the application of 2 V significantly increased the rate of defluorination, with a final F concentration of 0.98 ± 0.17 ppm (a 42% increase over UV-only conditions). In PFNA (9-carbon) degradation, the final F concentration was 0.67 ± 0.03 ppm under UV-only conditions, which increased marginally to 0.68 ± 0.03 under 0 V conditions (not significant). However, under UV/2V conditions, the final F concentration increased significantly to 1.12 ± 0.12 ppm (a 67% increase over UV-only conditions). Based on these results, under UV-only conditions, the PFCA chain length had little impact on the defluorination rate when only hydrated electrons were involved (0.64 ppm, 0.69 ppm and 0.67 ppm for 7, 8 and 9 carbon chain compounds, respectively). This data matches previous studies where defluorination rates by hydrated electrons were found to be independent of chain length.[244] Immersing the electrodes (UV/0V conditions) resulted in a small increase in defluorination rates of PFHpA and PFOA (9.3% and 14.5% respectively), and only a marginal increase in the defluorination of PFNA. However, the increased defluorination was not statistically significant, and it is unclear why an uncharged electrode surface would contribute to increased defluorination.

Under UV/2V conditions, there was a small increase in the defluorination rate of PFHpA (8.5% increase in the final F concentration over UV/0V conditions). We observed a greater enhancement in defluorination for PFOA (24% increase in F concentration over UV/0V), and an even greater increase during PFNA degradation (67% increase in F concentration over UV/0V). In order to determine whether this increase can

be attributed to potential-driven ET between the electrode and the sorbed molecules, we performed XPS measurements (Table 5) to quantify the amount of PFCA sorbed on the electrode surface, which is the first step in the ET process.

Table 5: Surface coverage on the electrode (measured by XPS)

Species	Fluoride surface coverage
PFNA	0.19±0.06%
PFOA	0.13±0.01%
PFHpA	0.08±0.04%
PFOS	4.45±0.49%
PFHxS	0.65±0.23%
PFBS	below detection limit

A previous study on the sorption of PFCAs on activated carbon showed that longer chain compounds exhibited higher sorption, which is associated with the more hydrophobic nature of the longer perfluorinated tail.[288] This would indicate that PFNA should have the highest sorption, followed by PFOA and then PFHpA. While very little F could be detected on the surface of the electrode tested for sorption of PFHpA (0.08 ± 0.04 % surface coverage), the electrodes tested with PFOA showed a slightly greater amount of F (0.13 ± 0.01 % surface coverage), and PFNA showed an even greater amount (0.19 ± 0.06 % surface coverage). Since the data clearly demonstrates that the longer-chained molecules exhibit better defluorination under these conditions (UV/2V), and since there is some difference in sorption of PFHpA, PFOA and PFNA on the electrode surface, this enhanced defluorination rate for longer chained compounds is likely due to sorption on to the electrode, followed by ET from the electrode which weakens C-F bonds, and subsequent breakdown by hydrated electrons. Previous studies used density function theory (DFT) to calculate the effect of the chain length on the bond dissociation energy (BDE) of the C-F bond in PFAS

molecules.[289] It was found that the BDE for C-F bonds on longer chain compounds are lower.[289] The average BDE reported for PFNA, PFOA, and PFHpA was 108.6 kcal/mol, 108.8 kcal/mol, and 109.4 kcal/mol, respectively. However, the energy provided by one hydrated electron is 85.33 kcal/mol (genuine binding energy).[290] This energy is insufficient to break the C-F bond, and a minimum of two hydrated electrons would be required for this process. As a result, there was no observed difference in the degradation rate under UV-only or UV/0V conditions (since energy from two hydrated electrons is much greater than the bond dissociation energy of C-F bonds in all three PFCAs investigated). However, under the UV/2V conditions, the priming of the sorbed molecules which destabilizes and weakens the C-F bond, allows cleavage by a single hydrated electron.

The defluorination of PFSA molecules with different chain lengths (PFBS (4 carbons), PFHxS (6 carbons), and PFOS (8 carbons)) was studied under UV, UV/0V and UV/2V conditions (Figures 36d, e, f). For PFBS, very little defluorination was observed under all three conditions (0.006 ± 0.001 ppm with UV, 0.009 ± 0.002 ppm with UV/0V, and 0.008 ± 0.001 ppm with UV/2V) (Figure 36d). When studying the 6-carbon PFHxS, the F concentrations under UV-only conditions reached a very low 0.07 ± 0.01 ppm. Immersing electrodes in the solution enhanced degradation rate by 100% to 0.15 ± 0.03 ppm, and the application of 2 V enhanced the defluorination further, increasing F concentrations from 0.15 ± 0.03 ppm to 0.24 ± 0.06 ppm (a 60% increase over UV/0V) after 2 hours of reaction (Figure 36e). For 8-carbon PFOS, the F concentration under UV conditions was 0.12 ± 0.01 ppm, increasing by 125% to 0.27 ± 0.05 ppm when electrodes were immersed into the solution (Figure 36f). The application of 2 V further increased the defluorination rate, resulting in a final F concentration of 0.63 ± 0.03 ppm (a 133% increase over UV/0V). While we observed some (albeit, very limited) breakdown of 6 carbon compound PFHxS (0.07 ± 0.01 ppm) and 8 carbon compound PFOS (0.12 ± 0.01 ppm) under UV-only conditions, no PFBS (4 carbon compound) breakdown (0.006 ± 0.001 ppm) was observed. This agrees with previous studies showing that shorter chain PFSAs are much harder to break down by hydrated electrons.[289] While immersing the electrode and applying potential did not impact the PFBS degradation rate, results were different in the case of the two

longer chained compounds. For PFHxS and PFOS, simply immersing the electrode increased defluorination rate significantly, whereas the application of 2 V enhanced it even further. Several studies on the sorption of different chain-length sulfonated PFAS molecules have shown that longer chain PFAS are sorbed on to granular activated carbon to a much greater extent.[288] The data in Table 5 shows that, as expected, the carbon chain length had a big impact on PFSA adsorption (F not detected, 0.65 ± 0.23 % surface coverage, and 4.45 ± 0.49 % surface coverage for PFBS, PFHxS, and PFOS, respectively). As in the case of PFCAs, the enhanced defluorination observed when the 2 V potential was applied is likely due to potential- driven ET between the electrode and the sorbed molecule, followed by an attack by a hydrated electron. Since sorption on the electrode surface is the first step in the defluorination process, and is critical for the ET between the electrode and target molecule to occur, it follows that shorter chain compounds which are sorbed to a lesser extent will exhibit lower defluorination rates. It is possible that the enhanced defluorination of PFHxS and PFOS that we observed in the absence of an applied cell potential can be attributed to ET caused by the open circuit potential (-0.03 V), which possibly causes bond destabilization to a lesser extent, making the C-F bonds more susceptible to breakdown by hydrated electrons. Alternatively, it has been observed that the simple act of adsorption onto surfaces functionalized with quaternary ammonium groups increased the defluorination of PFOS.[291, 292] It is possible that the CTAB molecules on the surface of the electrode used here facilitates a measure of instability in the adsorbed PFSA molecules, which contributes to the observed elevated defluorination rates. However, further investigation of this matter is warranted.[291, 292]

The % defluorination (Figure 36g) was calculated as the concentration of fluoride measured in the sample at the end of two hours, expressed as a percent of the fluoride concentration expected on 100% defluorination. The highest defluorination was observed for 9-carbon PFNA, at 32 ± 3.4% defluorination. For the slightly shorter 8-carbon PFOA, the defluorination was 28.5 ± 5%. For 7-carbon chained compound PFHpA, the defluorination further dropped to 22.7 ± 1.5%. For sulfonated compounds, the 8-carbon chain PFOS reached 19.2 ± 1.2% defluorination. For the 6-carbon chained PFHxS, the final defluorination was

7.8 ± 1.9%. However, the 4-carbon PFBS experienced barely any defluorination (0.3 ± 0.03%). These values are in line with previous studies where sulfonated PFASs were harder to defluorinate than

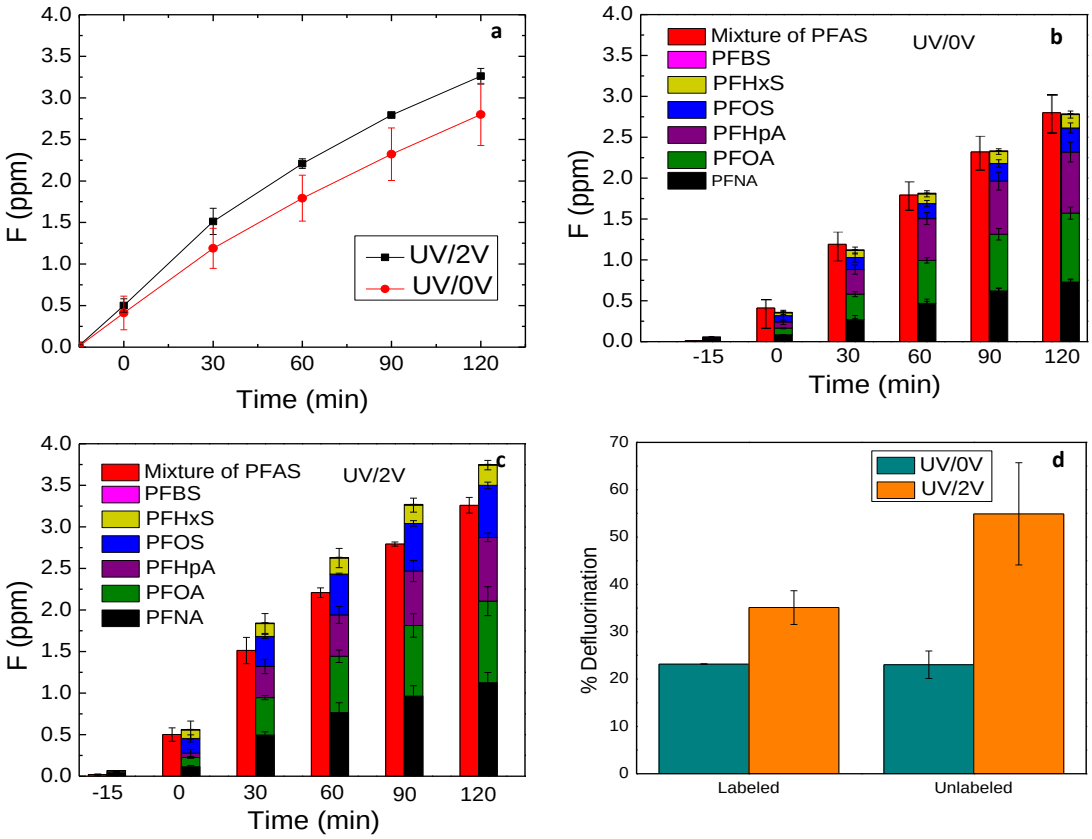

Figure 35: (a) Defluorination of PFAS mixtures under UV/0V and UV/2V conditions, and comparison between experimentally observed defluorination of PFAS mixtures and expected defluorination of PFAS mixtures based on individual compounds, tested under conditions of (b) UV/0V and (c) UV/2V; and (d) defluorination for labeled (C13) and non-labeled (C12) PFOS under UV/2V All experiments conducted at pH 11.5 and N_2 purging.

carboxylated PFAS, and in compounds with the same headgroup, the ease of defluorination decreases with decrease in chain length.[10]

5.3.3 Degrading PFAS mixtures

To test the effect of mixtures on PFAS defluorination rates, experiments were carried out with 5 ppm of each of the PFAS molecules tested previously along with 50mM of $NaClO_4$ (Figure 37a, b and c). Under UV/0V conditions, the final F concentration resulting from the defluorination of the PFAS mixture was 2.8 ± 0.3 ppm (Figure 37a). When 2 V potential was applied, the fluoride concentration increased by 16.1% to 3.2 ± 0.1 ppm (Figure 37a). Figures 37b and 37c show a comparison between the F concentrations observed

during degradation of the mixture and the sum of the F concentration observed during degradation of individual compounds. Under UV/0V conditions, at the end of 2 hours, the experimental values (2.8 ± 0.3 ppm) are close to the expected values from defluorination of individual compounds (2.6 ± 0.3 ppm), a 7.1% difference albeit not a statistically significant one. However, under UV/2V conditions, significant differences emerge. Specifically, the experimentally observed fluoride concentration resulting from degrading the PFAS mixture was 3.2 ± 0.1 ppm, significantly lower than the expected values from the degradation of individual compounds (3.8 ± 0.4 ppm), an 18.8% difference. Studies on the sorption of PFCAs on bamboo activated carbon and IRA67 resin showed a significant reduction in adsorption when a mixture of PFCA was tested.[243, 293] This was due to the PFCA molecules competing for adsorption sites. Thus, we speculate that competition between PFSA molecules for adsorption sites on the CNT electrode limits ET and reduces overall PFAS degradation rates.

5.3.4 Probing the mechanism of the two-electron reduction of PFAS

ET reactions occur when an electron is passed from the electrode surface to the molecule, requiring these two entities to be in close proximity, with the driving force for this reaction being a potential difference between the electrode and the molecule.[246] If the potential difference is large enough (which leads to a sufficiently energetic electron), this ET reaction can result in bond cleavage. However, if the potential difference is insufficient (leading to an insufficiently energetic electron), the electron can relax and return to the electrode.[294] After electron transfer to a sorbed PFAS molecule, the bound molecule shifts to an excited state and a radical anion intermediate is formed. In this excited state, molecular bonds are weakened (i.e., elongated) and are more susceptible to cleavage by the transfer of a hydrated electron.[294, 295]

The strength of a covalent bond is a function of the atomic species that compose the bond, as well as their atomic weight. Specifically, heavier atoms form stronger bonds.[296] Therefore, when comparing the defluorination of PFOS molecules sorbed onto a CNT electrode, as an example, we would expect that PFOS molecules containing heavier atoms (i.e., ^{13}C labeled PFOS) undergo slower defluorination rates relative to unlabeled PFOS, if destabilization and cleavage of the C-F bond is involved in the rate-determining step of

PFOS transformation. This is known as the kinetic isotope effect, where heavier isotopes of molecules exhibit a lower vibrational frequency, making it harder to break the bonds and resulting in slower rates of reaction.[297]

Figure 37d shows the defluorination rates of isotopically labeled and unlabeled PFOS under UV/0V and UV/2V conditions. In UV/0V conditions, the defluorination rates of both labeled and unlabeled PFOS were very similar (23.02 ± 2.9 % for unlabeled, and 23.16 ± 0.06 for labeled), such that there is no observable kinetic isotope effect in this system. In contrast, a marked isotope effect was observed in UV/2V systems; while application of 2 V resulted in a % defluorination of 54 ± 10.8 % (a 134% increase relative to 0 V systems) for unlabeled PFOS, we observed a significantly smaller increase in the defluorination rate of isotopically labeled PFOS (^{13}C) of 35 ± 3.6 % (only a 52% increase relative to 0 V systems). This difference corresponds to a ^{13}C kinetic isotope effect (k_{13}/k_{12}) for labeled PFOS of ~1.5 in 2 V systems.

The evidence of a ^{13}C kinetic isotope effect in the 2 V systems, and the lack of such an effect in the absence of an applied potential, is consistent with different rate determining reaction steps in each system. In the absence of applied potential, hydrated electrons are the only species that contribute to defluorination. As previously noted, the energy supplied by one hydrated electron (85.33kcal/mol) is insufficient to dissociate the C-F bond, whereas the energy provided by two hydrated electrons is much larger than that needed to break the C-F bond (~100 kcal/mol for unlabeled[111], and slightly higher for labeled). In this case, we hypothesize that the rate determining reaction step is associated with the rate of hydrated electron transfer (i.e., the timescales associated with the transfer of a second hydrated electron needed to dissociate the C-F bond are longer than the subsequent bond dissociation step). Because the rate-determining step involves electron transfer but not bond dissociation, there is no difference between the rate of defluorination of labeled and unlabeled PFOS under UV/0V conditions.

In systems with applied potential, DFT calculations have shown that the addition of one electron reduces the C-F BDE significantly, making these bonds more susceptible to cleavage through the addition of a hydrated electron.[111] Thus, for the UV/2V systems, we hypothesize that the initial electron transfer step

from the electrode, which distorts and destabilizes the C-F bond, becomes rate limiting in the PFOS degradation process. The rate of this initial electron transfer would be expected to be slower for stronger ^{13}C-F bonds relative to ^{12}C-F bonds, consistent with the kinetic isotope effect observed in these systems. Once the bound PFOS is primed via this initial electron transfer, our hypothesis assumes that subsequent reaction with a hydrated electron and C-F bond dissociation would be fast relative to the initial, destabilizing electron transfer event. This mechanism is consistent with our overall hypothesis that the enhanced defluorination observed under the UV/2V conditions is a result of C-F bond excitation by the transient ET step and subsequent breakdown by the hydrated electron.

5.3.5 Theoretical calculations comparing electron transfer rates from the electrode to a sorbed PFOS molecule with and without applied potential

To calculate and predict the electron-transfer rates for all the chemical species examined in this work, we utilized Marcus theory,[259, 298] which describes the electron-transfer process between a donor and acceptor molecule according to the following general equation:

$$D^m + A^n \xrightarrow{k_{ET}} D^{m+1} + A^{n-1}. \quad \text{(A)}$$

On the left-hand side of Eq. (A), D^m denotes a donor molecule with an electronic charge state of m, and A^n represents an acceptor molecule having a charge state of n (we have chosen to use this notation since many of the chemical species studied in this work have various electronic charged states). After the electron-transfer process has occurred, the donor (D^{m+1}) on the right-hand side of Eq. (A) now has a charge state of $m + 1$, and the acceptor (A^{n-1}) gains an electron and attains a charge state of $n - 1$. The non-adiabatic electron-transfer rate, k_{ET}, in Marcus theory is given by

$$k_{ET} = \frac{4\pi}{h} V_{rp}^2 \left(\frac{1}{4\pi\lambda k_B T}\right)^{\frac{1}{2}} \exp\left[-\frac{\Delta G^{\ddagger}}{k_B T}\right], \quad \text{(B)}$$

where h is Planck's constant, k_B is Boltzmann's constant, T is the temperature, V_{rp} is the transfer integral between the reactant and product, λ is the reorganization energy, and $\Delta G^{\ddagger}$ is the activation energy

$\left(=\frac{(\lambda+\Delta G^{\circ})^2}{4\lambda}\right)$, where ΔG° is the difference in energy between the reactants and products in Eq. (A). Figure 38 depicts the relationships between ΔG°, $\Delta G^{\ddagger}$, and λ for two Marcus-theory parabolas that represent the free energy curves of the reactant and product states. In the diabatic (i.e., non-adiabatic) representation, the electronic character of the reactant and product does not change as one moves along the reaction coordinate; hence, the reactant and product curves (colored red and blue) cross with an activation energy of $\Delta G^{\ddagger}$. In contrast, within the adiabatic representation (which are solutions/eigenstates of the Schrödinger equation and can be directly computed with quantum chemistry methods), the two curves avoid crossing and form an upper and lower curve (colored in solid black).

As mentioned previously, quantum chemistry methods can be used to directly calculate ΔG°, λ, and V_{rp} to yield the electron-transfer rate, k_{ET}. For generality, we use the standard notation $E(a|b)$ to represent the energy of state "a" calculated at the optimized equilibrium structure of state "b" (i.e., a and b may or may not be the same). To this end, the difference in energy between the reactants and products, ΔG°, is given by

$$\Delta G^{\circ} = E(D^m|D^m) + E(A^n|A^n) - E(D^{m+1}|D^{m+1}) - E(A^{n-1}|A^{n-1}). \quad \text{(C)}$$

The reorganization energy can be computed with the conventional "four-point" method[299]:

$$\lambda = E(D^{m+1}|D^m) - E(D^{m+1}|D^{m+1}) + E(A^{n-1}|A^n) - E(A^{n-1}|A^{n-1}). \quad \text{(D)}$$

Finally, the transfer integral for electrons, V_{rp}, can be approximated by an energy-splitting expression[300] given by

$$V_{rp} = \frac{\varepsilon_{\mathrm{LUMO+1}} - \varepsilon_{\mathrm{LUMO}}}{2}, \quad \text{(E)}$$

where $\varepsilon_{\mathrm{LUMO}}$ and $\varepsilon_{\mathrm{LUMO+1}}$ are the lowest unoccupied molecular orbital (LUMO) and the (L+1)UMO orbital energies of the dimer complex. With the adiabatic quantities in Eqs. (C) – (E) properly defined (and computable with quantum chemistry methods), this allow us to calculate the non-adiabatic electron-transfer rate, k_{ET} , in Eq. (B). All of the parameters in Eqs. (C) – (E) were obtained at the B97D/6-31G(d,p) level of theory in conjunction with a conductor-like polarizable continuum model (PCM) devised by Tomasi and

co-workers[301-305] , which we have previously used to calculate radical-based oxidation reactions in other aqueous systems.[266, 306]

We used the ET process between a CTAB-functionalized CNT electrode and PFOS as a model calculation. To rationalize the electron-transfer rates between the various charged states of the electrode (CNT + ammonium) and PFOS, we considered two specific reactions:

$$(\mathrm{CNT + ammonium})^{+1} + \mathrm{PFOS}^{-1} \xrightarrow{k_{ET}} (\mathrm{CNT + ammonium})^{+2} + \mathrm{PFOS}^{-2}, \quad \text{(R1)}$$

$$(\mathrm{CNT + ammonium})^{0} + \mathrm{PFOS}^{-1} \xrightarrow{k_{ET}} (\mathrm{CNT + ammonium})^{+1} + \mathrm{PFOS}^{-2}, \quad \text{(R2)}$$

where the subscripts follow the same convention described previously in Eq. (1) and denote the charge state of the specific chemical species/complex. Reactions R1 and R2 were chosen as representative models to contrast electron-transfer rates when the (CNT + ammonium) complex has a different charge state (i.e. the $(\mathrm{CNT + ammonium})^{0}$ complex has an extra negative charge compared to the positively-charged $(\mathrm{CNT + ammonium})^{+1}$ complex). The following Marcus theory parameters for each of the molecular reactions were obtained at the B97D/6-31G(d,p) level of theory with the PCM model (Table 6):

Table 6: Marcus theory calculations

Reaction	V_{rp} (eV)	λ (eV)	ΔG° (eV)	k_{ET} (s^{-1})
R1	0.135	0.648	-2.91	4.84×10^{-20}
R2	0.138	0.650	-2.54	6.48×10^{-10}

As can be seen in Table 6, the electron-transfer rate of R2 is significantly faster than R1, primarily due to the ΔG° term. In other words, the electron-transfer rate from the (CNT + ammonium) complex to PFOS is significantly faster when it is more negatively charged, which is reflected in the ΔG° energetic difference.

Since it is well-known that DFT-predicted rate constants are known to exhibit error, the numbers presented in the table are only meant to give overall trends. While the k_{ET} rates reported in Table 6 represent electron-transfer reactions under ideal conditions (i.e., they do not take into account other non-adiabatic electronic/nuclear effects), the significantly larger R2 value clearly indicates that a negatively charged electrode will yield a faster ET from the electrode to sorbed PFOS, resulting in the C-F bonds weakening to a larger extent, thus making them more susceptible to breakdown by hydrated electrons.

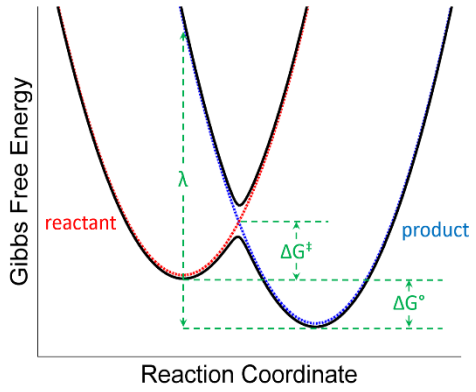

Figure 36: Schematic depicting the relationships between ΔG^°, 〖ΔG〗^‡, and λ for an electron transfer between two free energy curves of a reactant and product. The dotted diabatic curves are allowed to intersect whereas the solid-colored adiabatic curves avoid crossing

5.3.6 Degradation of chlorinated solvents

The degradation rates of trichloroethylene (TCE) and cis-dichloroethylene (cDCE) were measured using the same experimental conditions used to assess PFAS defluorination (Figure 39). For TCE (Figure 39a), the final Cl concentration under UV-only conditions was 1.53 ± 0.13 ppm, increasing marginally to 1.62 ± 0.36 ppm under conditions of UV/0V (not statistically significant). Under UV/2V conditions, the final Cl concentration was 1.58 ± 0.3 ppm at the end of two hours. The error bars for all these conditions are overlapping, indicating that there was no significant difference in chloride evolution rates. For cDCE (Figure 39b), the Cl concentration after two hours was 1.42 ± 0.08 ppm under UV only conditions. Under UV/0V conditions, final Cl concentration was 1.6 ± 0.4 ppm, and the degradation rate under UV/2V

conditions was the lowest, with a final Cl concentration of 1.15 ± 0.04 ppm. However, from figure 39b, it can be seen that the Cl concentrations are very close until the 90-minute sample was collected, and then deviated significantly in the final 30 minutes. The reason for this is unclear, although error bars for UV/0V and UV are quite large, making this difference statistically insignificant. These results suggest that the immersion of electrodes and the application of an external potential did not impact dechlorination rates of chlorinated solvents.

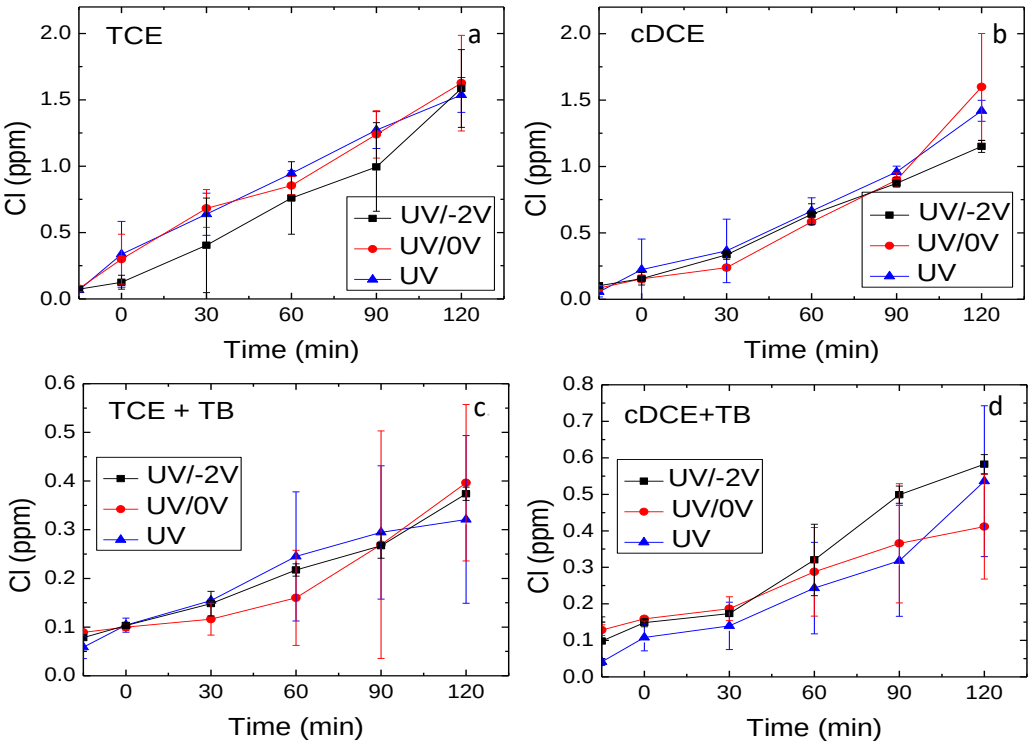

Figure 37: Degradation of (a) TCE and (b) cDCE under UV/-2V, UV/0V and UV only; and degradation of (c) TCE+TB and (d) cDCE+TB under UV/-2V, UV/0V and UV only.

Degradation of aqueous TCE and cDCE has been carried out by direct UV photolysis, generally in the presence of chlorine or H_2O_2.[307, 308] Such advanced oxidation processes work by generating OH• that break down TCE and cDCE.[309] Medium pressure UV light (with no additional chemical additives) can also generate OH• when water is irradiated with it.[310] Hence, it is possible that the degradation of TCE and cDCE observed in figures 39a and 39b was due to oxidation by hydroxyl radicals rather than reduction by hydrated electrons. To test whether oxidation was indeed the dominant mechanism, we added 15 µM of TB, a hydroxyl radical scavenger, to the solution (Figures 39c, d). Indeed, the rate of chloride evolution fell

dramatically, with a final chloride concentration between 0.3-0.4 ppm for TCE and 0.4-0.6 ppm for cDCE (compared to 1.5-1.6 ppm and 1.1-1.6 ppm in the absence of TB, a 75% and 60% decrease for TCE and cDCE, respectively). Therefore, it is reasonable to conclude that in these experiments, both TCE and cDCE were primarily degraded through an oxidative reaction with hydroxyl radicals and not through a reductive mechanism. While chloride evolution was suppressed in the presence of TB, it did not go to zero, suggesting that hydrated electrons possibly play a role in the dechlorination of these compounds, albeit a relatively minor one compared to hydroxyl radicals. Again, no significant difference was observed between the different operating conditions (UV-only, UV/0 V, and UV/2 V) (Figures 39c, d).

For enhanced reductive dechlorination from potential-driven ET to occur, sorption of the molecule on to the electrode is a prerequisite. To test whether this is taking place, we performed XPS analysis of the electrode material immersed in solutions of TCE and cDCE (data not shown). However, no chlorine could be detected on the electrode surface, indicating that no sorption occurred. Therefore, in order to promote degradation by this pathway, electrode materials that are more capable of sorbing chlorinated solvents need to be fabricated.

5.4 Conclusion

In summary, we tested the dehalogenation of six PFAS compounds and two chlorinated solvents by a combined UV/electrochemical system. The rate of defluorination for PFAS was highly dependent on the headgroup, with carboxylated compounds defluorinating to a greater extent than sulfonated compounds. Carbon chain length affects the extent to which defluorination occurs, with shorter chain compounds being harder to degrade. We speculate that this difference arises from a combination of poor adsorption onto the electrode, which limits the effectiveness of ET, coupled to the stronger C-F bonds in short-chained PFAS molecules. When attempting to degrade PFAS mixtures, we observed a small drop in performance compared to pure PFAS solutions, under the UV/2V conditions; this difference was not observed under the UV/0V conditions. This is likely caused by competition for electrode sorption sites, which limited the effectiveness of ET reactions that promote defluorination. Using DFT, we calculated that rate of ET from

the electrode to the PFOS molecule is 10 orders of magnitude greater when the electrode is more negatively charged (i.e. when an external cathodic potential is applied), compared to when there is no externally applied potential, demonstrating that ET is likely to occur in our system. In addition, experiments with isotopically labeled and unlabeled PFOS compounds showed higher defluorination rates of unlabeled PFOS, confirming that ET from the electrode to the PFOS molecule facilitates its defluorination. We also confirmed that chlorinated solvents can be degraded in the UV system, although the degradation mechanism is dominated by an oxidative pathway driven by UV-generated hydroxyl radicals. No adsorption of these solvents was detected on the electrodes, which would limit the effectiveness of any potential-driven ET in their degradation.

Acknowledgments:

We thank the Strategic Environmental Research and Development Program (ER18-1595) for their generous financial support.

Chapter 6: Summary, Conclusions and Future Work

The dissertation presented methods to modify surface properties to engineer interactions on the molecular level. These modifications in surface properties pave the way for enhanced contaminant removal and degradation.

In chapter 1, we briefly discussed the water scarcity issue and discussed ways to address them by using conventional and unconventional sources of water. We discussed membrane treatment processes in brief, classifying pressure-based membranes by size cut-off. We also discussed membrane distillation in depth, and talked about its potential applications in high salinity brine treatment and when waste heat is available. We discussed the temperature polarization phenomenon and various transport mechanisms, and talked about types of fouling and typical methods to address them. Thereafter, we introduced contaminants of emerging concern, with an in-depth discussion of PFAS. We talked about typical treatment processes and the need for an energy efficient degradation mechanism. We introduced previous studies of PFAS degradation by the hydrated electron. We then introduced and discussed the unique thermal, electric and adsorptive properties of carbon nanotubes (CNTs), alluding to their use in anti-scaling and potential for PFAS breakdown.

Chapter 2 included the set-up of an automated MD system, and treatment of dairy farm wastewater. We studied permeate flux and conductivity to analyze fouling and wetting behavior. Further, we used analytical techniques such as colorimetry, total organic carbon and gas chromatography-time of flight mass spectrometry to measure carbon, nutrient and organic presence in the feed, permeate and retentate. We analyzed membrane surface using SEM and XPS. We demonstrated that polypropylene membranes can successfully be used for water recoveries up to 75%, while maintaining a flux greater than 10 LMH. Along with water vapor, we also recovered volatile organic compounds on the permeate side. In this study, we demonstrated that MD can effectively be used to separate volatiles and water vapor from non-volatiles. Being hydrophobic, MD membranes rejected water with dissolved contaminants. However, the large pores allowed vapor and volatile compounds to pass through after volatilization. With accurate control of operating conditions, there is potential application in separation of volatiles from water, as well as

separation of different volatile compounds. We also demonstrated that residual heat from the hydrothermal liquefaction process can be used to drive the membrane distillation system.

In chapter 3, we extended the application of membrane distillation to the treatment of high salinity brines. A polypropylene membrane showed very rapid flux decline due to scaling. Using a custom-built spray coater, we coated a percolating network of CNTs on the membrane, and used this electrically conductive membrane for high salinity brine treatment. We studied scaling (by measuring flux and observing the membrane surface under SEM and EDAX) behavior due to silicate and calcium sulfate under different potentials and frequencies applied. Best results were observed under 2 V alternating current of 1 Hz frequency, where we observed 80% decrease in the rate of flux decline. Ions in the solution respond to applied potential on the membrane. Thus, the switching membrane polarity results in mixing within the concentration polarization layer, preventing the formation of prenucleation clusters, and effectively disrupting the EDL. We considered the time-scale required for the formation of an EDL, and concluded that the time in 1 Hz as well as 10 Hz is sufficient for EDL formation. To explain why 1 Hz showed better results than 10 Hz, we performed EIS measurements. These measurements showed that the electrical conductivity of the CNT membrane limits the transfer of charges within the membrane, and the membrane behaves as a resistor rather than a capacitor under 10 Hz conditions. We hypothesize that a more conductive membrane will potentially show even better scaling resistance. An economic analysis showed that an additional cost of 0.024\$/m^3 of water produced due to the use of these conductive membranes. For a thorough analysis, we need to consider the potential cost savings due to reduce in pretreatment and brine disposal. In this chapter, we demonstrated that coating polymeric membranes with an electrically conducting layer such as CNTs can enhance anti-scaling properties. Applied electric potential can lead to the formation of electric fields, which influence ion movement in the water. The frequency of the potential applied has an effect on ion movement, and higher frequency should be more effective as it reduces the time available for cations and anions to precipitate and form scales.

In chapter 4, we talked about the difficulty of degrading PFOS, and fabricated a CNT electrode for PFOS degradation. We used this electrode in a UV reactor, where medium pressure UV light could generate hydrated electrons. We studied the effect of different surfactants used in the dispersion of CNT on PFOS degradation, and found by surface analysis using XPS, that the cationic surfactant CTAB showed best results. This was because of enhanced electrostatic attraction between quaternary ammonium group in the CTAB and the PFOS molecule. We studied the impact of pH, dissolved oxygen, applied potential, electrode surface area and the effect of adding t-butanol and nitrate as hydroxyl radical scavengers and hydrated electron scavengers respectively. We found that the defluorination ratio was 23.7% under 2 V potential at a pH of 11.5 with nitrogen gas bubbled. We also showed by DFT calculations that the addition of one electron from the power supply weakened the C-F bond, making it susceptible to breakdown by hydrated electron. Here, we demonstrated that a CNT electrode can affectively sorb molecules, and the surface properties of the electrode can be tailored to suit the contaminant to be sorbed. Superior electrical properties of the electrode also allow electron transfer, which was important for PFAS degradation.

In chapter 5, we extended this photo-electrochemical degradation mechanism to other linear PFAS having different headgroups and chain lengths. The CNT-CTAB electrode showed best absorption of long chained sulfonated compounds, with the adsorption decreasing with a decrease in chain length. For carboxylated compounds, adsorption was lower. We studied the impact of mixtures of these PFAS on degradation rate and found that under -2 V applied potential, degradation rate of mixtures drops and is lower than what we expected from individual compounds degradation. This is due to competition for adsorption sites on the electrode. We used isotopically labeled and unlabeled PFOS, and observed a higher defluorination ratio for the unlabeled compound. This confirmed our hypothesis of the two-electron mechanism for PFAS breakdown. We also studied dechlorination of chlorinated solvents TCE and cDCE and observed 30-40% dechlorination. However, when t-butanol was added (a hydroxyl radical scavenger), the dechlorination fell to 10-20%, indicating that these chlorinated solvents were being oxidized and the CNT electrode and applied potential were playing no role in their breakdown. Here, we demonstrated that individual as well

as mixtures of PFAS could be treated by the photo-electrochemical mechanism. We also demonstrated that when chlorinated solvent co-occur with PFAS, their degradation takes place primarily by an oxidative mechanism.

In conclusion, hydrophobic and electrostatic forces can be used to reject or attract contaminants in water. Modifying surface properties to take advantage of these forces can improve separation and sorption processes for water treatment. In the MD treatment of a stream containing a mixture of volatile and non-volatile hydrophobic and hydrophilic compounds by a hydrophobic polymeric membrane, hydrophobic forces play a role by selectively allowing hydrophobic compounds, volatiles and water vapor to pass through, or be adsorbed on the surface, while rejecting non-volatile dissolved and particulate matter. Any hydrophobic (volatile or non-volatile) contaminants present in these water sources would either sorb on to the hydrophobic surface (fouling in MD systems), or pass through (as flux in MD systems). The membrane surface properties can be modified to influence sorption of compounds on the membrane surface and rejection of undesired compounds in the permeate. Accurate control of operating conditions can also ensure that the passage of undesired volatile compounds into the permeate stream is limited. In the MD treatment of a stream containing non-volatile hydrophilic charged compounds or salts (which dissociate to form cations and anions), the main hindrance is scaling, or accumulation of precipitates on the membrane surface. Scale formation occurs due to crystallization of scale forming cations and anions, followed by their deposition on the membrane surface. For crystallization to occur, the co-location of cations and anions for some period of time is essential. If we prevent this co-location for timescales long enough to form prenucleation clusters, we can successfully mitigate scaling. This can be achieved by influencing the motion of cations and anions within the concentration polarization layer by subjecting them to varying electric fields. Due to the superior electrically conductive properties of CNTs, the fabricated ECMD membrane showed excellent anti-scaling properties. When an external potential was applied, an electric field was formed within the water flow channel. This caused the charged ECMD to attract oppositely charged ions, and repel similarly charged ions. This resulted in the formation of an electrical double layer along the

ECMD surface due to a high concentration of oppositely charged ions and low concentration of similarly charged ions near the surface. Rapid change in the direction of this electric field by applying alternating current can cause movement and mixing of anions and cations due to the rapid change in EDL. This influences the cation/anion ratio, and also causes movement of charged species, which prevents them from precipitating and forming scales.

Hydrophobic and electrostatic forces on surfaces can also lead to superior sorption properties. Hydrophobic contaminants will preferentially sorb on to hydrophobic surfaces, since the entropically favorable state for hydrophobic contaminants is to attach with other hydrophobic surfaces. Electrostatic forces also help in sorption, since oppositely charged contaminants are attracted to the surface, resulting in their electrosorption. The degradation of complex perfluorinated compounds is faster in the presence of excess electrons. Sorption of contaminants on to a surface can help achieve this state of excess electrons by providing electrons from an externally applied potential. CNTs have unique electron transfer, electrical and adsorptive properties. This combined with the ability to modify their surface properties by functionalization, make them excellent candidates for the removal and degradation of complex perfluorinated compounds. COOH functionalized CNTs with a cationic surfactant as dispersion medium proved successful at sorbing PFAS compounds. The positively charged quaternary ammonium group on the cationic surfactant formed an electrostatic bond with PFAS, which carries a net negative surface charge. The externally applied potential difference coupled with CNTs superior electron transfer properties caused a transient electron transfer, which destabilized bonds in sorbed PFAS molecules. This in turn increased the probability of their breakdown by hydrated electrons.

The use of CNTs to improve removal and degradation processes is promising, especially due to the ability to modify CNTs surfaces. Electrically conducting membranes for anti-scaling are promising as an energy efficient and economical method for high salinity brine treatment. They could also reduce the volume of brine to be disposed. Fabrication of more conductive membranes could be advantageous in further enhancing scaling mitigation. PFAS breakdown by the photo-electrochemical mechanism while not energy

efficient at low PFAS concentrations, can potentially be used as a secondary step after nanofiltration of PFAS contaminated water. The reductive dechlorination by a photo-electrochemical mechanism may be possible. However, further work on the sorption properties of carbon nanotubes with respect to chlorinated solvents is warranted.

References:

1. Magdoff, F., Global Resource Depletion: Is Population the Problem? *Monthly Review* **2013,** *64* (8), 13.
2. Sirotin, N. Technological advances will drive our quest to live longer. https://www.thenational.ae/opinion/technological-advances-will-drive-our-quest-to-live-longer-1.222373.
3. Roberts, L., 9 Billion? American Association for the Advancement of Science: 2011.
4. Repetto, R.; Holmes, T., The role of population in resource depletion in developing countries. *Population and development review* **1983**, 609-632.
5. Guest, J. S.; Skerlos, S. J.; Barnard, J. L.; Beck, M. B.; Daigger, G. T.; Hilger, H.; Jackson, S. J.; Karvazy, K.; Kelly, L.; Macpherson, L., A new planning and design paradigm to achieve sustainable resource recovery from wastewater. ACS Publications: 2009.
6. Gellings, C. W.; Parmenter, K. E., Energy efficiency in fertilizer production and use. 2016.
7. Christensen, J. B.; Jensen, D. L.; Grøn, C.; Filip, Z.; Christensen, T. H., Characterization of the dissolved organic carbon in landfill leachate-polluted groundwater. *Water research* **1998,** *32* (1), 125-135.
8. Posmanik, R.; Labatut, R. A.; Kim, A. H.; Usack, J. G.; Tester, J. W.; Angenent, L. T., Coupling hydrothermal liquefaction and anaerobic digestion for energy valorization from model biomass feedstocks. *Bioresource Technology* **2017,** *233*, 134-143.
9. Leahy, S. From not enough to too much, the world's water crisis explained. https://www.nationalgeographic.com/news/2018/03/world-water-day-water-crisis-explained/.
10. Global Water Assessment, D. o. W. S., UNESCO Global water resources under increasing pressure from rapidly growing demands and climate change, according to new UN World Water Development Report. http://www.unesco.org/new/fileadmin/MULTIMEDIA/HQ/SC/pdf/WWDR4%20Background%20Briefing%20Note_ENG.pdf.
11. Water, U. Water Scarcity. https://www.unwater.org/water-facts/scarcity/.
12. Hobza, P.; Müller-Dethlefs, K., *Non-covalent interactions: theory and experiment*. Royal Society of Chemistry: 2010.
13. Schalley, C. A., *Analytical methods in supramolecular chemistry*. John Wiley & Sons: 2012; Vol. 1.
14. Murray, J. S.; Politzer, P., The electrostatic potential: an overview. *Wiley Interdisciplinary Reviews: Computational Molecular Science* **2011,** *1* (2), 153-163.
15. Ciferri, A.; Perico, A., *Ionic interactions in natural and synthetic macromolecules*. John Wiley & Sons: 2012.
16. Butt, H.-J., Electrostatic interaction in atomic force microscopy. *Biophysical journal* **1991,** *60* (4), 777-785.
17. Grahame, D. C., The electrical double layer and the theory of electrocapillarity. *Chemical reviews* **1947,** *41* (3), 441-501.
18. Valleau, J.; Torrie, G., The electrical double layer. III. Modified Gouy− Chapman theory with unequal ion sizes. *The Journal of Chemical Physics* **1982,** *76* (9), 4623-4630.
19. Outhwaite, C. W.; Bhuiyan, L. B., An improved modified Poisson–Boltzmann equation in electric-double-layer theory. *Journal of the Chemical Society, Faraday Transactions 2: Molecular and Chemical Physics* **1983,** *79* (5), 707-718.
20. Kirby, B. J., *Micro-and nanoscale fluid mechanics: transport in microfluidic devices*. Cambridge university press: 2010.
21. Lyklema, J., *Fundamentals of interface and colloid science: soft colloids*. Elsevier: 2005; Vol. 5.

22. Clogston, J. D.; Patri, A. K., Zeta potential measurement. In *Characterization of nanoparticles intended for drug delivery*, Springer: 2011; pp 63-70.
23. Dzyaloshinskii, I. E.; Lifshitz, E. M.; Pitaevskii, L. P., The general theory of van der Waals forces. *Advances in Physics* **1961,** *10* (38), 165-209.
24. Israelachvili, J. N., The nature of van der Waals forces. *Contemporary Physics* **1974,** *15* (2), 159-178.
25. Margenau, H., Van der Waals forces. *Reviews of Modern Physics* **1939,** *11* (1), 1.
26. Rabinovich, Y. I.; Derjaguin, B., Interaction of hydrophobized filaments in aqueous electrolyte solutions. *Colloids and Surfaces* **1988,** *30* (2), 243-251.
27. Kronberg, B., The hydrophobic effect. *Current Opinion in Colloid & Interface Science* **2016,** *22*, 14-22.
28. Chandler, D., Interfaces and the driving force of hydrophobic assembly. *Nature* **2005,** *437* (7059), 640-647.
29. Claesson, P. M.; Christenson, H. K., Very long range attractive forces between uncharged hydrocarbon and fluorocarbon surfaces in water. *The Journal of Physical Chemistry* **1988,** *92* (6), 1650-1655.
30. Israelachvili, J.; Pashley, R., The hydrophobic interaction is long range, decaying exponentially with distance. *Nature* **1982,** *300* (5890), 341-342.
31. Pendergast, M. M.; Hoek, E. M., A review of water treatment membrane nanotechnologies. *Energy & Environmental Science* **2011,** *4* (6), 1946-1971.
32. Zularisam, A.; Ismail, A.; Sakinah, M., Application and challenges of membrane in surface water treatment. *Journal of Applied Sciences* **2010,** *10* (5), 380-390.
33. Alzahrani, S.; Mohammad, A. W., Challenges and trends in membrane technology implementation for produced water treatment: A review. *Journal of Water Process Engineering* **2014,** *4*, 107-133.
34. Zeman, L. J.; Zydney, A., *Microfiltration and ultrafiltration: principles and applications*. CRC Press: 2017.
35. Howe, K. J.; Clark, M. M., Fouling of microfiltration and ultrafiltration membranes by natural waters. *Environmental science & technology* **2002,** *36* (16), 3571-3576.
36. Mohammad, A. W.; Teow, Y.; Ang, W.; Chung, Y.; Oatley-Radcliffe, D.; Hilal, N., Nanofiltration membranes review: Recent advances and future prospects. *Desalination* **2015,** *356*, 226-254.
37. Greenlee, L. F.; Lawler, D. F.; Freeman, B. D.; Marrot, B.; Moulin, P., Reverse osmosis desalination: water sources, technology, and today's challenges. *Water research* **2009,** *43* (9), 2317-2348.
38. Zhang, S.; Drioli, E., Pervaporation membranes. *Separation science and technology* **1995,** *30* (1), 1-31.
39. Liu, G.; Wei, W.; Jin, W., Pervaporation membranes for biobutanol production. *ACS Sustainable Chemistry & Engineering* **2014,** *2* (4), 546-560.
40. Alkhudhiri, A.; Darwish, N.; Hilal, N., Membrane distillation: a comprehensive review. *Desalination* **2012,** *287*, 2-18.
41. Chan, K.; Matsuura, T.; Sourirajan, S., Interfacial forces, average pore size, and pore size distribution of ultrafiltration membranes. *Industrial & Engineering Chemistry Product Research and Development* **1982,** *21* (4), 605-612.
42. Wijmans, J. G.; Baker, R. W., The solution-diffusion model: a review. *Journal of membrane science* **1995,** *107* (1-2), 1-21.
43. Drioli, E.; Ali, A.; Macedonio, F., Membrane distillation: Recent developments and perspectives. *Desalination* **2015,** *356*, 56-84.

44. Burgoyne, A.; Vahdati, M., Direct contact membrane distillation. *Separation Science and Technology* **2000,** *35* (8), 1257-1284.
45. Curcio, E.; Drioli, E., Membrane distillation and related operations—a review. *Separation and Purification Reviews* **2005,** *34* (1), 35-86.
46. Lawson, K. W.; Lloyd, D. R., Membrane distillation. *Journal of membrane Science* **1997,** *124* (1), 1-25.
47. Lawson, K. W.; Lloyd, D. R., Membrane distillation. II. Direct contact MD. *Journal of Membrane Science* **1996,** *120* (1), 123-133.
48. Khayet, M., Membranes and theoretical modeling of membrane distillation: a review. *Advances in colloid and interface science* **2011,** *164* (1-2), 56-88.
49. Souhaimi, M. K.; Matsuura, T., *Membrane distillation: principles and applications*. Elsevier: 2011.
50. Khayet, M.; Godino, P.; Mengual, J. I., Theory and experiments on sweeping gas membrane distillation. *Journal of Membrane Science* **2000,** *165* (2), 261-272.
51. Khayet, M.; Godino, M.; Mengual, J., Theoretical and experimental studies on desalination using the sweeping gas membrane distillation method. *Desalination* **2003,** *157* (1-3), 297-305.
52. Bandini, S.; Saavedra, A.; Sarti, G. C., Vacuum membrane distillation: experiments and modeling. *AIChE Journal* **1997,** *43* (2), 398-408.
53. Lawson, K. W.; Lloyd, D. R., Membrane distillation. I. Module design and performance evaluation using vacuum membrane distillation. *Journal of membrane science* **1996,** *120* (1), 111-121.
54. Franken, A.; Nolten, J.; Mulder, M.; Bargeman, D.; Smolders, C., Wetting criteria for the applicability of membrane distillation. *Journal of Membrane Science* **1987,** *33* (3), 315-328.
55. García-Payo, M.; Izquierdo-Gil, M.; Fernández-Pineda, C., Wetting study of hydrophobic membranes via liquid entry pressure measurements with aqueous alcohol solutions. *Journal of colloid and interface science* **2000,** *230* (2), 420-431.
56. Swaminathan, J.; Chung, H. W.; Warsinger, D. M., Energy efficiency of membrane distillation up to high salinity: Evaluating critical system size and optimal membrane thickness. *Applied Energy* **2018,** *211*, 715-734.
57. Ali, M. I.; Summers, E. K.; Arafat, H. A., Effects of membrane properties on water production cost in small scale membrane distillation systems. *Desalination* **2012,** *306*, 60-71.
58. Karanikola, V.; Corral, A. F.; Jiang, H.; Sáez, A. E.; Ela, W. P.; Arnold, R. G., Effects of membrane structure and operational variables on membrane distillation performance. *Journal of Membrane Science* **2017,** *524*, 87-96.
59. Macedonio, F.; Ali, A.; Poerio, T.; El-Sayed, E.; Drioli, E.; Abdel-Jawad, M., Direct contact membrane distillation for treatment of oilfield produced water. *Separation and Purification Technology* **2014,** *126*, 69-81.
60. Schofield, R.; Fane, A.; Fell, C., Heat and mass transfer in membrane distillation. *Journal of Membrane Science* **1987,** *33* (3), 299-313.
61. Qtaishat, M.; Matsuura, T.; Kruczek, B.; Khayet, M., Heat and mass transfer analysis in direct contact membrane distillation. *Desalination* **2008,** *219* (1-3), 272-292.
62. Martínez-Díez, L.; Vazquez-Gonzalez, M. I., Temperature and concentration polarization in membrane distillation of aqueous salt solutions. *Journal of membrane science* **1999,** *156* (2), 265-273.
63. Dittscher, U.; Woermann, D.; Wiedner, G., Temperature polarization in membrane distillation of water using a porous hydrophobic membrane. *Berichte der Bunsengesellschaft für physikalische Chemie* **1994,** *98* (8), 1056-1061.
64. Velazquez, A.; Mengual, J. I., Temperature polarization coefficients in membrane distillation. *Industrial & engineering chemistry research* **1995,** *34* (2), 585-590.

65. Ali, A.; Macedonio, F.; Drioli, E.; Aljlil, S.; Alharbi, O., Experimental and theoretical evaluation of temperature polarization phenomenon in direct contact membrane distillation. *Chemical Engineering Research and Design* **2013,** *91* (10), 1966-1977.
66. Tiraferri, A. Membrane-based water treatment to increase water supply. http://www.colloid.ch/index.php?name=membranes.
67. Chang, I.-S.; Le Clech, P.; Jefferson, B.; Judd, S., Membrane fouling in membrane bioreactors for wastewater treatment. *Journal of environmental engineering* **2002,** *128* (11), 1018-1029.
68. Goh, S.; Zhang, J.; Liu, Y.; Fane, A. G., Fouling and wetting in membrane distillation (MD) and MD-bioreactor (MDBR) for wastewater reclamation. *Desalination* **2013,** *323*, 39-47.
69. Gryta, M., Fouling in direct contact membrane distillation process. *Journal of Membrane Science* **2008,** *325* (1), 383-394.
70. Rao, U.; Posmanik, R.; Hatch, L. E.; Tester, J. W.; Walker, S. L.; Barsanti, K. C.; Jassby, D., Coupling hydrothermal liquefaction and membrane distillation to treat anaerobic digestate from food and dairy farm waste. *Bioresource technology* **2018,** *267*, 408-415.
71. Rao, U.; Iddya, A.; Jung, B.; Khor, C. M.; Hendren, Z.; Turchi, C.; Cath, T.; Hoek, E. M.; Ramon, G. Z.; Jassby, D., Mineral Scale Prevention on Electrically Conducting Membrane Distillation Membranes Using Induced Electrophoretic Mixing. *Environmental Science & Technology* **2020,** *54* (6), 3678-3690.
72. Duan, W.; Dudchenko, A.; Mende, E.; Flyer, C.; Zhu, X.; Jassby, D., Electrochemical mineral scale prevention and removal on electrically conducting carbon nanotube–polyamide reverse osmosis membranes. *Environmental Science: Processes & Impacts* **2014,** *16* (6), 1300-1308.
73. Antony, A.; Low, J. H.; Gray, S.; Childress, A. E.; Le-Clech, P.; Leslie, G., Scale formation and control in high pressure membrane water treatment systems: a review. *Journal of membrane science* **2011,** *383* (1-2), 1-16.
74. Al-Mutairi, N. N.; Aleem, F. A.; Al-Ahmad, M. I., Effect of antiscalants for inhibition of calcium sulfate deposition in thermal desalination systems. *Desalination and Water Treatment* **2009,** *10* (1-3), 39-46.
75. Zarebska, A.; Amor, A. C.; Ciurkot, K.; Karring, H.; Thygesen, O.; Andersen, T. P.; Hägg, M.-B.; Christensen, K. V.; Norddahl, B., Fouling mitigation in membrane distillation processes during ammonia stripping from pig manure. *Journal of Membrane Science* **2015,** *484*, 119-132.
76. Kim, C. Y.; Zhu, X.; Herzberg, M.; Walker, S.; Jassby, D., Impact of physical and chemical cleaning agents on specific biofilm components and the implications for membrane biofouling management. *Industrial & Engineering Chemistry Research* **2018,** *57* (9), 3359-3370.
77. Naidu, G.; Jeong, S.; Kim, S.-J.; Kim, I. S.; Vigneswaran, S., Organic fouling behavior in direct contact membrane distillation. *Desalination* **2014,** *347*, 230-239.
78. Warsinger, D. M.; Swaminathan, J.; Guillen-Burrieza, E.; Arafat, H. A., Scaling and fouling in membrane distillation for desalination applications: a review. *Desalination* **2015,** *356*, 294-313.
79. Gilron, J.; Ladizansky, Y.; Korin, E., Silica fouling in direct contact membrane distillation. *Industrial & Engineering Chemistry Research* **2013,** *52* (31), 10521-10529.
80. Aslam, M.; Ahmad, R.; Kim, J., Recent developments in biofouling control in membrane bioreactors for domestic wastewater treatment. *Separation and Purification Technology* **2018,** *206*, 297-315.
81. Maartens, A.; Swart, P.; Jacobs, E., Membrane pretreatment: a method for reducing fouling by natural organic matter. *Journal of colloid and interface science* **2000,** *221* (2), 137-142.
82. Rezaei, M.; Warsinger, D. M.; Duke, M. C.; Matsuura, T.; Samhaber, W. M., Wetting phenomena in membrane distillation: Mechanisms, reversal, and prevention. *Water research* **2018,** *139*, 329-352.
83. Lu, K. J.; Chen, Y.; Chung, T.-S., Design of omniphobic interfaces for membrane distillation–a review. *Water research* **2019,** *162*, 64-77.

84. Chen, L.-H.; Huang, A.; Chen, Y.-R.; Chen, C.-H.; Hsu, C.-C.; Tsai, F.-Y.; Tung, K.-L., Omniphobic membranes for direct contact membrane distillation: effective deposition of zinc oxide nanoparticles. *Desalination* **2018,** *428*, 255-263.
85. Deshmukh, A.; Boo, C.; Karanikola, V.; Lin, S.; Straub, A. P.; Tong, T.; Warsinger, D. M.; Elimelech, M., Membrane distillation at the water-energy nexus: limits, opportunities, and challenges. *Energy & Environmental Science* **2018,** *11* (5), 1177-1196.
86. Sharqawy, M. H.; Lienhard, J. H.; Zubair, S. M., Thermophysical properties of seawater: a review of existing correlations and data. *Desalination and water Treatment* **2010,** *16* (1-3), 354-380.
87. Le Gouellec, Y. A.; Elimelech, M., Calcium sulfate (gypsum) scaling in nanofiltration of agricultural drainage water. *Journal of Membrane Science* **2002,** *205* (1-2), 279-291.
88. Elimelech, M.; Phillip, W. A., The future of seawater desalination: energy, technology, and the environment. *science* **2011,** *333* (6043), 712-717.
89. Wang, P.; Chung, T.-S., Recent advances in membrane distillation processes: Membrane development, configuration design and application exploring. *Journal of membrane science* **2015,** *474*, 39-56.
90. Kim, S.; Chu, K. H.; Al-Hamadani, Y. A.; Park, C. M.; Jang, M.; Kim, D.-H.; Yu, M.; Heo, J.; Yoon, Y., Removal of contaminants of emerging concern by membranes in water and wastewater: a review. *Chemical Engineering Journal* **2018,** *335*, 896-914.
91. Zhao, Y.; Wong, C.; Wong, M. H., Environmental contamination, human exposure and body loadings of perfluorooctane sulfonate (PFOS), focusing on Asian countries. *Chemosphere* **2012,** *89* (4), 355-368.
92. Pérez, F.; Nadal, M.; Navarro-Ortega, A.; Fàbrega, F.; Domingo, J. L.; Barceló, D.; Farré, M., Accumulation of perfluoroalkyl substances in human tissues. *Environment international* **2013,** *59*, 354-362.
93. Lindstrom, A. B.; Strynar, M. J.; Libelo, E. L., Polyfluorinated compounds: past, present, and future. ACS Publications: 2011.
94. EPA, Drinking water health advisories for PFOA and PFOS. **2016**.
95. Medina, V. F.; Waisner, S. A.; Mattei-Sosa, J.; Martinez-Guerra, E.; Griggs, C. S.; Lalley, J. M.; Henderson, D. L.; Moores, L. C.; Prager, B. H. *Simulated Field Evaluation of the Decontamination Effluent Treatment System (DETS) for Wash Water from Mass Personnel Decontamination (MPD), Road Test, and Evaluation Treating Perfluorinated Alkyl Substances (PFAS)*; ENGINEER RESEARCH AND DEVELOPMENT CENTER VICKSBURG United States: 2019.
96. Milinovic, J.; Lacorte, S.; Vidal, M.; Rigol, A., Sorption behaviour of perfluoroalkyl substances in soils. *Science of the Total Environment* **2015,** *511*, 63-71.
97. Rao, U.; Su, Y.; Khor, C. M.; Jung, B.; Ma, S.; Cwiertny, D. M.; Wong, B. M.; Jassby, D., Structural Dependence of Reductive Defluorination of Linear PFAS Compounds in a UV/Electrochemical System. *Environmental Science & Technology* **2020**.
98. Appleman, T. D.; Dickenson, E. R.; Bellona, C.; Higgins, C. P., Nanofiltration and granular activated carbon treatment of perfluoroalkyl acids. *Journal of Hazardous Materials* **2013,** *260*, 740-746.
99. Dickenson, E.; Higgins, C., Treatment mitigation strategies for polyand perfluorinated chemicals (pp 1–123). 2018.
100. Thompson, J.; Eaglesham, G.; Reungoat, J.; Poussade, Y.; Bartkow, M.; Lawrence, M.; Mueller, J. F., Removal of PFOS, PFOA and other perfluoroalkyl acids at water reclamation plants in South East Queensland Australia. *Chemosphere* **2011,** *82* (1), 9-17.
101. Lin, H.; Niu, J.; Ding, S.; Zhang, L., Electrochemical degradation of perfluorooctanoic acid (PFOA) by Ti/SnO2–Sb, Ti/SnO2–Sb/PbO2 and Ti/SnO2–Sb/MnO2 anodes. *Water research* **2012,** *46* (7), 2281-2289.

102. Zhuo, Q.; Deng, S.; Yang, B.; Huang, J.; Wang, B.; Zhang, T.; Yu, G., Degradation of perfluorinated compounds on a boron-doped diamond electrode. *Electrochimica Acta* **2012,** *77*, 17-22.
103. Hori, H.; Yamamoto, A.; Hayakawa, E.; Taniyasu, S.; Yamashita, N.; Kutsuna, S.; Kiatagawa, H.; Arakawa, R., Efficient decomposition of environmentally persistent perfluorocarboxylic acids by use of persulfate as a photochemical oxidant. *Environmental Science & Technology* **2005,** *39* (7), 2383-2388.
104. Darwent, B. d. *Bond dissociation energies in simple molecules*; National Standard Reference Data System: 1970.
105. Farwell, S.; Beland, F.; Geer, R., Reduction pathways of organohalogen compounds: part I. Chlorinated benzenes. *Journal of Electroanalytical Chemistry and Interfacial Electrochemistry* **1975,** *61* (3), 303-313.
106. Hunter, S.; Christophorou, L., Electron attachment to the perfluoroalkanes n-CN F2 N+ 2 (N= 1–6) using high pressure swarm techniques. *The Journal of chemical physics* **1984,** *80* (12), 6150-6164.
107. Marcus, R. A., Chemical and electrochemical electron-transfer theory. *Annual review of physical chemistry* **1964,** *15* (1), 155-196.
108. Ramaswamy, N.; Mukerjee, S., Influence of inner-and outer-sphere electron transfer mechanisms during electrocatalysis of oxygen reduction in alkaline media. *The Journal of Physical Chemistry C* **2011,** *115* (36), 18015-18026.
109. Maran, F.; Workentin, M. S., Dissociative electron transfer. *Interface-Electrochemical Society* **2002,** *11* (4), 44-50.
110. Song, Z.; Tang, H.; Wang, N.; Zhu, L., Reductive defluorination of perfluorooctanoic acid by hydrated electrons in a sulfite-mediated UV photochemical system. *Journal of hazardous materials* **2013,** *262*, 332-338.
111. Su, Y.; Rao, U.; Khor, C. M.; Jensen, M. G.; Teesch, L. M.; Wong, B. M.; Cwiertny, D. M.; Jassby, D., Potential-Driven Electron Transfer Lowers the Dissociation Energy of the CF Bond and Facilitates Reductive Defluorination of Perfluorooctane Sulfonate (PFOS). *ACS applied materials & interfaces* **2019**.
112. Jin, L.; Zhang, P., Photochemical decomposition of perfluorooctane sulfonate (PFOS) in an anoxic alkaline solution by 185 nm vacuum ultraviolet. *Chemical Engineering Journal* **2015,** *280*, 241-247.
113. Park, H.; Vecitis, C. D.; Cheng, J.; Dalleska, N. F.; Mader, B. T.; Hoffmann, M. R., Reductive degradation of perfluoroalkyl compounds with aquated electrons generated from iodide photolysis at 254 nm. *Photochemical & Photobiological Sciences* **2011,** *10* (12), 1945-1953.
114. Gu, Y.; Dong, W.; Luo, C.; Liu, T., Efficient reductive decomposition of perfluorooctanesulfonate in a high photon flux UV/sulfite system. *Environmental science & technology* **2016,** *50* (19), 10554-10561.
115. Tang, L.; Iddya, A.; Zhu, X.; Dudchenko, A. V.; Duan, W.; Turchi, C.; Vanneste, J.; Cath, T. Y.; Jassby, D., Enhanced Flux and Electrochemical Cleaning of Silicate Scaling on Carbon Nanotube-Coated Membrane Distillation Membranes Treating Geothermal Brines. *ACS applied materials & interfaces* **2017,** *9* (44), 38594-38605.
116. De Lannoy, C.; Jassby, D.; Davis, D.; Wiesner, M., A highly electrically conductive polymer–multiwalled carbon nanotube nanocomposite membrane. *Journal of membrane science* **2012,** *415*, 718-724.
117. Dudchenko, A. V.; Rolf, J.; Russell, K.; Duan, W.; Jassby, D., Organic fouling inhibition on electrically conducting carbon nanotube–polyvinyl alcohol composite ultrafiltration membranes. *Journal of Membrane Science* **2014,** *468*, 1-10.
118. Ronen, A.; Duan, W.; Wheeldon, I.; Walker, S.; Jassby, D., Microbial attachment inhibition through low-voltage electrochemical reactions on electrically conducting membranes. *Environmental science & technology* **2015,** *49* (21), 12741-12750.

119. Li, Y.-H.; Wang, S.; Wei, J.; Zhang, X.; Xu, C.; Luan, Z.; Wu, D.; Wei, B., Lead adsorption on carbon nanotubes. *Chemical Physics Letters* **2002,** *357* (3-4), 263-266.
120. Tournus, F.; Charlier, J.-C., Ab initio study of benzene adsorption on carbon nanotubes. *Physical Review B* **2005,** *71* (16), 165421.
121. Balasubramanian, K.; Burghard, M., Chemically functionalized carbon nanotubes. *small* **2005,** *1* (2), 180-192.
122. Ellerie, J. R.; Apul, O. G.; Karanfil, T.; Ladner, D. A., Comparing graphene, carbon nanotubes, and superfine powdered activated carbon as adsorptive coating materials for microfiltration membranes. *Journal of hazardous materials* **2013,** *261*, 91-98.
123. Scarselli, M.; Castrucci, P.; De Crescenzi, M., Electronic and optoelectronic nano-devices based on carbon nanotubes. *Journal of Physics: Condensed Matter* **2012,** *24* (31), 313202.
124. Dudchenko, A. V.; Chen, C.; Cardenas, A.; Rolf, J.; Jassby, D., Frequency-dependent stability of CNT Joule heaters in ionizable media and desalination processes. *Nature nanotechnology* **2017,** *12* (6), 557.
125. Gao, C.; Guo, Z.; Liu, J.-H.; Huang, X.-J., The new age of carbon nanotubes: an updated review of functionalized carbon nanotubes in electrochemical sensors. *Nanoscale* **2012,** *4* (6), 1948-1963.
126. McKibben, M.; Williams, A.; Elders, W.; Eldridge, C., Saline brines and metallogenesis in a modern sediment-filled rift: the Salton Sea geothermal system, California, USA. *Applied Geochemistry* **1987,** *2* (5-6), 563-578.
127. Romero, C.; Ramos, P.; Costa, C.; Márquez, M. C., Raw and digested municipal waste compost leachate as potential fertilizer: comparison with a commercial fertilizer. *Journal of Cleaner Production* **2013,** *59*, 73-78.
128. Van Kauwenbergh, S. J., *World phosphate rock reserves and resources*. IFDC Muscle Shoals: 2010.
129. Rehm, G. W., *Understanding phosphorus fertilizers*. Minnesota Extension Service, University of Minnesota: 1997.
130. Gilbert, N., Environment: the disappearing nutrient. *Nature News* **2009,** *461* (7265), 716-718.
131. Modak, J. M., Haber process for ammonia synthesis. *Resonance* **2002,** *7* (9), 69-77.
132. Sutton, M. A.; Oenema, O.; Erisman, J. W.; Leip, A.; van Grinsven, H.; Winiwarter, W., Too much of a good thing. *Nature* **2011,** *472* (7342), 159-161.
133. Ren, Z. J.; Umble, A. K., Water treatment: Recover wastewater resources locally. *Nature* **2016,** *529* (7584), 25-25.
134. Cornel, P.; Schaum, C., Phosphorus recovery from wastewater: needs, technologies and costs. *Water Science and Technology* **2009,** *59* (6), 1069-1076.
135. Abdel-Raouf, N.; Al-Homaidan, A.; Ibraheem, I., Microalgae and wastewater treatment. *Saudi Journal of Biological Sciences* **2012,** *19* (3), 257-275.
136. Xie, M.; Nghiem, L. D.; Price, W. E.; Elimelech, M., Toward resource recovery from wastewater: extraction of phosphorus from digested sludge using a hybrid forward osmosis–membrane distillation process. *Environmental Science & Technology Letters* **2014,** *1* (2), 191-195.
137. James M. Macdonald, D. N. Milk Production Continues Shifting to Large-Scale Farms. https://www.ers.usda.gov/amber-waves/2014/december/milk-production-continues-shifting-to-large-scale-farms/.
138. Eghball, B.; Power, J. F., Phosphorus-and nitrogen-based manure and compost applications corn production and soil phosphorus. *Soil Science Society of America Journal* **1999,** *63* (4), 895-901.
139. De Meester, S.; Demeyer, J.; Velghe, F.; Peene, A.; Van Langenhove, H.; Dewulf, J., The environmental sustainability of anaerobic digestion as a biomass valorization technology. *Bioresource technology* **2012,** *121*, 396-403.

140. Inoue, S.; Tsukahara, K.; Sawayama, S., Analysis of effluent after anaerobic digestion of liquid phase separated from liquidized garbage. *Journal of bioscience and bioengineering* **2002,** *93* (6), 607-609.
141. Arnon, S.; Dahan, O.; Elhanany, S.; Cohen, K.; Pankratov, I.; Gross, A.; Ronen, Z.; Baram, S.; Shore, L. S., Transport of testosterone and estrogen from dairy-farm waste lagoons to groundwater. *Environmental Science & Technology* **2008,** *42* (15), 5521-5526.
142. Hombach, S.; Oleszkiewicz, J.; Lagasse, P.; Amy, L.; Zaleski, A.; Smyrski, K., Impact of landfill leachate on anaerobic digestion of sewage sludge. *Environmental technology* **2003,** *24* (5), 553-560.
143. Tambone, F.; Scaglia, B.; D'Imporzano, G.; Schievano, A.; Orzi, V.; Salati, S.; Adani, F., Assessing amendment and fertilizing properties of digestates from anaerobic digestion through a comparative study with digested sludge and compost. *Chemosphere* **2010,** *81* (5), 577-583.
144. Al Seadi, T.; Drosg, B.; Fuchs, W.; Rutz, D.; Janssen, R., Biogas digestate quality and utilization. In *The biogas handbook*, Elsevier: 2013; pp 267-301.
145. Angenent, L. T.; Usack, J. G.; Xu, J.; Hafenbradl, D.; Posmanik, R.; Tester, J. W., Integrating electrochemical, biological, physical, and thermochemical process units to expand the applicability of anaerobic digestion. *Bioresource Technology* **2017**.
146. Peterson, A. A.; Vogel, F.; Lachance, R. P.; Fröling, M.; Antal Jr, M. J.; Tester, J. W., Thermochemical biofuel production in hydrothermal media: a review of sub-and supercritical water technologies. *Energy & Environmental Science* **2008,** *1* (1), 32-65.
147. Déniel, M.; Haarlemmer, G.; Roubaud, A.; Weiss-Hortala, E.; Fages, J., Energy valorisation of food processing residues and model compounds by hydrothermal liquefaction. *Renewable and Sustainable Energy Reviews* **2016,** *54*, 1632-1652.
148. Yin, S.; Dolan, R.; Harris, M.; Tan, Z., Subcritical hydrothermal liquefaction of cattle manure to bio-oil: effects of conversion parameters on bio-oil yield and characterization of bio-oil. *Bioresource Technology* **2010,** *101* (10), 3657-3664.
149. Biller, P.; Friedman, C.; Ross, A. B., Hydrothermal microwave processing of microalgae as a pre-treatment and extraction technique for bio-fuels and bio-products. *Bioresource technology* **2013,** *136*, 188-195.
150. Biller, P.; Sharma, B. K.; Kunwar, B.; Ross, A. B., Hydroprocessing of bio-crude from continuous hydrothermal liquefaction of microalgae. *Fuel* **2015,** *159*, 197-205.
151. Cantero-Tubilla, B.; Cantero, D. A.; Martinez, C. M.; Tester, J. W.; Walker, L. P.; Posmanik, R., Characterization of the solid products from hydrothermal liquefaction of waste feedstocks from food and agricultural industries. *The Journal of Supercritical Fluids* **2017**.
152. Posmanik, R.; Cantero, D.; Malkani, A.; Sills, D.; Tester, J., Biomass conversion to bio-oil using sub-critical water: Study of model compounds for food processing waste. *The Journal of Supercritical Fluids* **2017,** *119*, 26-35.
153. Qian, L.; Wang, S.; Savage, P. E., Hydrothermal liquefaction of sewage sludge under isothermal and fast conditions. *Bioresource Technology* **2017,** *232*, 27-34.
154. Sheehan, J. D.; Savage, P. E., Products, Pathways, and Kinetics for the Fast Hydrothermal Liquefaction of Soy Protein Isolate. *ACS Sustainable Chemistry & Engineering* **2016,** *4* (12), 6931-6939.
155. Elliott, D. C.; Biller, P.; Ross, A. B.; Schmidt, A. J.; Jones, S. B., Hydrothermal liquefaction of biomass: developments from batch to continuous process. *Bioresource technology* **2015,** *178*, 147-156.
156. Van Doren, L. G.; Posmanik, R.; Bicalho, F. A.; Tester, J. W.; Sills, D. L., Prospects for energy recovery during hydrothermal and biological processing of waste biomass. *Bioresource technology* **2017,** *225*, 67-74.
157. Tommaso, G.; Chen, W.-T.; Li, P.; Schideman, L.; Zhang, Y., Chemical characterization and anaerobic biodegradability of hydrothermal liquefaction aqueous products from mixed-culture wastewater algae. *Bioresource technology* **2015,** *178*, 139-146.

158. Tijing, L. D.; Woo, Y. C.; Choi, J.-S.; Lee, S.; Kim, S.-H.; Shon, H. K., Fouling and its control in membrane distillation—a review. *Journal of Membrane Science* **2015,** *475*, 215-244.
159. Slade, A.; Jassby, D., Affordable, flexible, and modular: a guide to open-source membrane-based water treatment systems. *Environmental Science: Water Research & Technology* **2016,** *2* (6), 965-974.
160. Schofield, R.; Fane, A.; Fell, C.; Macoun, R., Factors affecting flux in membrane distillation. *Desalination* **1990,** *77*, 279-294.
161. Schmarr, H.-G.; Bernhardt, J., Profiling analysis of volatile compounds from fruits using comprehensive two-dimensional gas chromatography and image processing techniques. *Journal of Chromatography A* **2010,** *1217* (4), 565-574.
162. El-Bourawi, M.; Ding, Z.; Ma, R.; Khayet, M., A framework for better understanding membrane distillation separation process. *Journal of membrane science* **2006,** *285* (1), 4-29.
163. Hayward, G.; Lau, I., Toxicity of organic solvents to fatty acid forming bacteria. *The Canadian Journal of Chemical Engineering* **1989,** *67* (1), 157-161.
164. Playne, M.; Smith, B., Toxicity of organic extraction reagents to anaerobic bacteria. *Biotechnology and bioengineering* **1983,** *25* (5), 1251-1265.
165. Davis, H.; Kloden, D.; Schaleger, L. *Chemistry and stoichiometry of wood liquefaction*; Lawrence Berkeley Lab., CA (USA): 1981.
166. Maddi, B.; Panisko, E.; Wietsma, T.; Lemmon, T.; Swita, M.; Albrecht, K.; Howe, D., Quantitative Characterization of Aqueous Byproducts from Hydrothermal Liquefaction of Municipal Wastes, Food Industry Wastes, and Biomass Grown on Waste. *ACS Sustainable Chemistry & Engineering* **2017,** *5* (3), 2205-2214.
167. Gollakota, A.; Kishore, N.; Gu, S., A review on hydrothermal liquefaction of biomass. *Renewable and Sustainable Energy Reviews* **2017**.
168. Berg, L.; Ratanapupech, P., Separation of ethyl acetate from ethanol and water by extractive distillation. Google Patents: 1983.
169. Amy, G.; Ghaffour, N.; Li, Z.; Francis, L.; Linares, R. V.; Missimer, T.; Lattemann, S., Membrane-based seawater desalination: Present and future prospects. *Desalination* **2017,** *401*, 16-21.
170. Elimelech, M.; Bhattacharjee, S., A novel approach for modeling concentration polarization in crossflow membrane filtration based on the equivalence of osmotic pressure model and filtration theory. *Journal of Membrane Science* **1998,** *145* (2), 223-241.
171. Kim, S.; Hoek, E. M., Modeling concentration polarization in reverse osmosis processes. *Desalination* **2005,** *186* (1-3), 111-128.
172. Song, L.; Elimelech, M., Theory of concentration polarization in crossflow filtration. *Journal of the Chemical Society, Faraday Transactions* **1995,** *91* (19), 3389-3398.
173. Andritsos, N.; Karabelas, A., Calcium carbonate scaling in a plate heat exchanger in the presence of particles. *International Journal of Heat and Mass Transfer* **2003,** *46* (24), 4613-4627.
174. Amjad, Z., *Mineral scale formation and inhibition*. Springer Science & Business Media: 2013.
175. Fu, F.; Wang, Q., Removal of heavy metal ions from wastewaters: a review. *Journal of environmental management* **2011,** *92* (3), 407-418.
176. Younos, T., Environmental issues of desalination. *Journal of Contemporary Water Research & Education* **2005,** *132* (1), 11-18.
177. Sheikholeslami, R.; Watkinson, A., Scaling of plain and externally finned heat exchanger tubes. *Journal of Heat Transfer* **1986,** *108* (1), 147-152.
178. Watkinson, A.; Martinez, O., Scaling of heat exchanger tubes by calcium carbonate. *Journal of Heat Transfer* **1975,** *97* (4), 504-508.
179. Shirazi, S.; Lin, C.-J.; Chen, D., Inorganic fouling of pressure-driven membrane processes—a critical review. *Desalination* **2010,** *250* (1), 236-248.

180. Auer, S.; Frenkel, D., Line tension controls wall-induced crystal nucleation in hard-sphere colloids. *Physical review letters* **2003,** *91* (1), 015703.
181. Mi, B.; Elimelech, M., Gypsum scaling and cleaning in forward osmosis: measurements and mechanisms. *Environmental science & technology* **2010,** *44* (6), 2022-2028.
182. Pouget, E. M.; Bomans, P. H.; Goos, J. A.; Frederik, P. M.; Sommerdijk, N. A., The initial stages of template-controlled CaCO3 formation revealed by cryo-TEM. *Science* **2009,** *323* (5920), 1455-1458.
183. Gryta, M., Calcium sulphate scaling in membrane distillation process. *Chemical Papers* **2009,** *63* (2), 146-151.
184. Lyster, E.; Kim, M.-m.; Au, J.; Cohen, Y., A method for evaluating antiscalant retardation of crystal nucleation and growth on RO membranes. *Journal of Membrane Science* **2010,** *364* (1-2), 122-131.
185. Rahardianto, A.; McCool, B. C.; Cohen, Y., Reverse osmosis desalting of inland brackish water of high gypsum scaling propensity: kinetics and mitigation of membrane mineral scaling. *Environmental science & technology* **2008,** *42* (12), 4292-4297.
186. Shih, W.-Y.; Rahardianto, A.; Lee, R.-W.; Cohen, Y., Morphometric characterization of calcium sulfate dihydrate (gypsum) scale on reverse osmosis membranes. *Journal of Membrane Science* **2005,** *252* (1-2), 253-263.
187. Hasson, D.; Drak, A.; Semiat, R., Inception of CaSO4 scaling on RO membranes at various water recovery levels. *Desalination* **2001,** *139* (1-3), 73-81.
188. Nghiem, L. D.; Cath, T., A scaling mitigation approach during direct contact membrane distillation. *Separation and Purification Technology* **2011,** *80* (2), 315-322.
189. Ahmed, F.; Lalia, B. S.; Kochkodan, V.; Hilal, N.; Hashaikeh, R., Electrically conductive polymeric membranes for fouling prevention and detection: A review. *Desalination* **2016,** *391*, 1-15.
190. Celik, E.; Park, H.; Choi, H.; Choi, H., Carbon nanotube blended polyethersulfone membranes for fouling control in water treatment. *Water research* **2011,** *45* (1), 274-282.
191. Duan, W.; Chen, G.; Chen, C.; Sanghvi, R.; Iddya, A.; Walker, S.; Liu, H.; Ronen, A.; Jassby, D., Electrochemical removal of hexavalent chromium using electrically conducting carbon nanotube/polymer composite ultrafiltration membranes. *Journal of Membrane Science* **2017,** *531*, 160-171.
192. Gustafsson, J. P., Visual MINTEQ 3.0 user guide. *KTH, Department of Land and Water Recources, Stockholm, Sweden* **2011**.
193. Vaisman, L.; Wagner, H. D.; Marom, G., The role of surfactants in dispersion of carbon nanotubes. *Advances in colloid and interface science* **2006,** *128*, 37-46.
194. Zhu, X.; Dudchenko, A. V.; Khor, C. M.; He, X.; Ramon, G. Z.; Jassby, D., Field-Induced Redistribution of Surfactants at the Oil/Water Interface Reduces Membrane Fouling on Electrically Conducting Carbon Nanotube UF Membranes. *Environmental science & technology* **2018,** *52* (20), 11591-11600.
195. Stojiljković, A. S.; Sužnjević, D. Ž.; Blagojević, S. N., Open-circuit potential of a Pt electrode immersed in different aqueous solutions. *Reaction Kinetics, Mechanisms and Catalysis* **2018,** *123* (1), 165-175.
196. Sablani, S.; Goosen, M.; Al-Belushi, R.; Wilf, M., Concentration polarization in ultrafiltration and reverse osmosis: a critical review. *Desalination* **2001,** *141* (3), 269-289.
197. Sirkar, K. K.; Rao, G. H., Approximate design equations and alternate design methodologies for tubular reverse osmosis desalination. *Industrial & Engineering Chemistry Process Design and Development* **1981,** *20* (1), 116-127.
198. Zhu, A.; Rahardianto, A.; Christofides, P. D.; Cohen, Y., Reverse osmosis desalination with high permeability membranes—cost optimization and research needs. *Desalination and Water Treatment* **2010,** *15* (1-3), 256-266.

199. Niibori, Y.; Kunita, M.; Tochiyama, O.; Chida, T., Dissolution rates of amorphous silica in highly alkaline solution. *Journal of nuclear science and technology* **2000,** *37* (4), 349-357.
200. Meng, S.; Mansouri, J.; Ye, Y.; Chen, V., Effect of templating agents on the properties and membrane distillation performance of TiO2-coated PVDF membranes. *Journal of membrane science* **2014,** *450*, 48-59.
201. Bremere, I.; Kennedy, M.; Mhyio, S.; Jaljuli, A.; Witkamp, G.-J.; Schippers, J., Prevention of silica scale in membrane systems: removal of monomer and polymer silica. *Desalination* **2000,** *132* (1-3), 89-100.
202. Ong, C.; Goh, P.; Lau, W.; Misdan, N.; Ismail, A., Nanomaterials for biofouling and scaling mitigation of thin film composite membrane: A review. *Desalination* **2016,** *393*, 2-15.
203. Vrijenhoek, E. M.; Hong, S.; Elimelech, M., Influence of membrane surface properties on initial rate of colloidal fouling of reverse osmosis and nanofiltration membranes. *Journal of membrane science* **2001,** *188* (1), 115-128.
204. Provis, J. L.; Duxson, P.; Lukey, G. C.; Separovic, F.; Kriven, W. M.; Van Deventer, J. S., Modeling speciation in highly concentrated alkaline silicate solutions. *Industrial & engineering chemistry research* **2005,** *44* (23), 8899-8908.
205. Gilron, J.; Hasson, D., Calcium sulphate fouling of reverse osmosis membranes: flux decline mechanism. *Chemical Engineering Science* **1987,** *42* (10), 2351-2360.
206. Lewis, A.; Nathoo, J.; Seewoo, S.; Lacour, S. In *Prevention of Scaling in Mine Waters Using Slurry Precipitation and Recycle Reverse Osmosis (SPARRO)*, International Symposium on Industrial Crystallization, 2002.
207. Lafuente, B.; Downs, R. T.; Yang, H.; Stone, N., The power of databases: the RRUFF project. In *Highlights in mineralogical crystallography*, Walter de Gruyter GmbH: 2016; pp 1-29.
208. Sheikholeslami, R.; Al-Mutaz, I.; Tan, S.; Tan, S., Some aspects of silica polymerization and fouling and its pretreatment by sodium aluminate, lime and soda ash. *Desalination* **2002,** *150* (1), 85-92.
209. Seewoo, S.; Van Hille, R.; Lewis, A., Aspects of gypsum precipitation in scaling waters. *Hydrometallurgy* **2004,** *75* (1-4), 135-146.
210. Gebauer, D.; Völkel, A.; Cölfen, H., Stable prenucleation calcium carbonate clusters. *Science* **2008,** *322* (5909), 1819-1822.
211. Saha, A.; Lee, J.; Pancera, S. M.; Bräeu, M. F.; Kempter, A.; Tripathi, A.; Bose, A., New Insights into the transformation of calcium sulfate hemihydrate to gypsum using time-resolved cryogenic transmission electron microscopy. *Langmuir* **2012,** *28* (30), 11182-11187.
212. Ahmi, F.; Gadri, A., Kinetics and morphology of formed gypsum. *Desalination* **2004,** *166*, 427-434.
213. Lochhead, M. J.; Letellier, S. R.; Vogel, V., Assessing the role of interfacial electrostatics in oriented mineral nucleation at charged organic monolayers. *The Journal of Physical Chemistry B* **1997,** *101* (50), 10821-10827.
214. Pope, J.; Yao, S.; Fane, A., Quantitative measurements of the concentration polarisation layer thickness in membrane filtration of oil-water emulsions using NMR micro-imaging. *Journal of Membrane Science* **1996,** *118* (2), 247-257.
215. Pomerantz, N.; Ladizhansky, Y.; Korin, E.; Waisman, M.; Daltrophe, N.; Gilron, J., Prevention of scaling of reverse osmosis membranes by "zeroing" the elapsed nucleation time. Part I. Calcium sulfate. *Industrial & engineering chemistry research* **2006,** *45* (6), 2008-2016.
216. Talapatra, S.; Chakraborty, S., Double layer overlap in ac electroosmosis. *European Journal of Mechanics-B/Fluids* **2008,** *27* (3), 297-308.
217. Gebauer, D.; Cölfen, H., Prenucleation clusters and non-classical nucleation. *Nano Today* **2011,** *6* (6), 564-584.

218. Arulanandam, S.; Li, D., Liquid transport in rectangular microchannels by electroosmotic pumping. *Colloids and Surfaces A: Physicochemical and Engineering Aspects* **2000,** *161* (1), 89-102.
219. Aslan, M.; Zeiger, M.; Jäckel, N.; Grobelsek, I.; Weingarth, D.; Presser, V., Improved capacitive deionization performance of mixed hydrophobic/hydrophilic activated carbon electrodes. *Journal of Physics: Condensed Matter* **2016,** *28* (11), 114003.
220. Guyes, E. N.; Shocron, A. N.; Simanovski, A.; Biesheuvel, P.; Suss, M. E., A one-dimensional model for water desalination by flow-through electrode capacitive deionization. *Desalination* **2017,** *415*, 8-13.
221. Wang, L.; Lin, S., Membrane capacitive deionization with constant current vs constant voltage charging: which is better? *Environmental science & technology* **2018,** *52* (7), 4051-4060.
222. Bazant, M. Z.; Thornton, K.; Ajdari, A., Diffuse-charge dynamics in electrochemical systems. *Physical review E* **2004,** *70* (2), 021506.
223. Atlas, I.; Ramon, G. Z., Periodic energy conversion in an electric-double-layer capacitor. *Journal of colloid and interface science* **2018,** *530*, 675-685.
224. Amrei, S. H.; Bukosky, S. C.; Rader, S. P.; Ristenpart, W. D.; Miller, G. H., Oscillating Electric Fields in Liquids Create a Long-Range Steady Field. *Physical review letters* **2018,** *121* (18), 185504.
225. Park, J.-S.; Choi, J.-H.; Woo, J.-J.; Moon, S.-H., An electrical impedance spectroscopic (EIS) study on transport characteristics of ion-exchange membrane systems. *Journal of colloid and interface science* **2006,** *300* (2), 655-662.
226. Eslamian, M., A mathematical model for the design and fabrication of polymer solar cells by spray coating. *Drying technology* **2013,** *31* (4), 405-413.
227. Authority, E. F. S., Perfluorooctane sulfonate (PFOS), perfluorooctanoic acid (PFOA) and their salts Scientific Opinion of the Panel on Contaminants in the Food chain. *Efsa Journal* **2008,** *6* (7), 653.
228. Harada, K.; Nakanishi, S.; Saito, N.; Tsutsui, T.; Koizumi, A., Airborne perfluorooctanoate may be a substantial source contamination in Kyoto area, Japan. *Bulletin of environmental contamination and toxicology* **2005,** *74* (1), 64-69.
229. Cheng, J.; Vecitis, C. D.; Park, H.; Mader, B. T.; Hoffmann, M. R., Sonochemical degradation of perfluorooctane sulfonate (PFOS) and perfluorooctanoate (PFOA) in landfill groundwater: environmental matrix effects. *Environmental science & technology* **2008,** *42* (21), 8057-8063.
230. Trojanowicz, M.; Bojanowska-Czajka, A.; Bartosiewicz, I.; Kulisa, K., Advanced Oxidation/Reduction Processes treatment for aqueous perfluorooctanoate (PFOA) and perfluorooctanesulfonate (PFOS)–A review of recent advances. *Chemical Engineering Journal* **2018,** *336*, 170-199.
231. Beach, S. A.; Newsted, J. L.; Coady, K.; Giesy, J. P., Ecotoxicological evaluation of perfluorooctanesulfonate (PFOS). In *Reviews of environmental contamination and toxicology*, Springer: 2006; pp 133-174.
232. Haug, L. S.; Huber, S.; Schlabach, M.; Becher, G.; Thomsen, C., Investigation on per-and polyfluorinated compounds in paired samples of house dust and indoor air from Norwegian homes. *Environmental science & technology* **2011,** *45* (19), 7991-7998.
233. Jogsten, I. E.; Nadal, M.; van Bavel, B.; Lindström, G.; Domingo, J. L., Per-and polyfluorinated compounds (PFCs) in house dust and indoor air in Catalonia, Spain: implications for human exposure. *Environment international* **2012,** *39* (1), 172-180.
234. Stahl, T.; Heyn, J.; Thiele, H.; Hüther, J.; Failing, K.; Georgii, S.; Brunn, H., Carryover of perfluorooctanoic acid (PFOA) and perfluorooctane sulfonate (PFOS) from soil to plants. *Archives of environmental contamination and toxicology* **2009,** *57* (2), 289-298.
235. Moody, C. A.; Hebert, G. N.; Strauss, S. H.; Field, J. A., Occurrence and persistence of perfluorooctanesulfonate and other perfluorinated surfactants in groundwater at a fire-training area at Wurtsmith Air Force Base, Michigan, USA. *Journal of Environmental Monitoring* **2003,** *5* (2), 341-345.

236. Saito, N.; Harada, K.; Inoue, K.; Sasaki, K.; Yoshinaga, T.; Koizumi, A., Perfluorooctanoate and perfluorooctane sulfonate concentrations in surface water in Japan. *Journal of Occupational Health* **2004,** *46* (1), 49-59.
237. Moody, C. A.; Martin, J. W.; Kwan, W. C.; Muir, D. C.; Mabury, S. A., Monitoring perfluorinated surfactants in biota and surface water samples following an accidental release of fire-fighting foam into Etobicoke Creek. *Environmental science & technology* **2002,** *36* (4), 545-551.
238. Moody, C. A.; Field, J. A., Determination of perfluorocarboxylates in groundwater impacted by fire-fighting activity. *Environmental science & technology* **1999,** *33* (16), 2800-2806.
239. Bossi, R.; Riget, F. F.; Dietz, R.; Sonne, C.; Fauser, P.; Dam, M.; Vorkamp, K., Preliminary screening of perfluorooctane sulfonate (PFOS) and other fluorochemicals in fish, birds and marine mammals from Greenland and the Faroe Islands. *Environmental Pollution* **2005,** *136* (2), 323-329.
240. Smithwick, M.; Norstrom, R. J.; Mabury, S. A.; Solomon, K.; Evans, T. J.; Stirling, I.; Taylor, M. K.; Muir, D. C., Temporal trends of perfluoroalkyl contaminants in polar bears (Ursus maritimus) from two locations in the North American Arctic, 1972− 2002. *Environmental science & technology* **2006,** *40* (4), 1139-1143.
241. Okada, E.; Kashino, I.; Matsuura, H.; Sasaki, S.; Miyashita, C.; Yamamoto, J.; Ikeno, T.; Ito, Y. M.; Matsumura, T.; Tamakoshi, A., Temporal trends of perfluoroalkyl acids in plasma samples of pregnant women in Hokkaido, Japan, 2003–2011. *Environment international* **2013,** *60*, 89-96.
242. Buck, R. C.; Franklin, J.; Berger, U.; Conder, J. M.; Cousins, I. T.; De Voogt, P.; Jensen, A. A.; Kannan, K.; Mabury, S. A.; van Leeuwen, S. P., Perfluoroalkyl and polyfluoroalkyl substances in the environment: terminology, classification, and origins. *Integrated environmental assessment and management* **2011,** *7* (4), 513-541.
243. Merino, N.; Qu, Y.; Deeb, R. A.; Hawley, E. L.; Hoffmann, M. R.; Mahendra, S., Degradation and removal methods for perfluoroalkyl and polyfluoroalkyl substances in water. *Environmental Engineering Science* **2016,** *33* (9), 615-649.
244. Park, H.; Vecitis, C. D.; Cheng, J.; Choi, W.; Mader, B. T.; Hoffmann, M. R., Reductive defluorination of aqueous perfluorinated alkyl surfactants: effects of ionic headgroup and chain length. *The Journal of Physical Chemistry A* **2009,** *113* (4), 690-696.
245. Vecitis, C. D.; Park, H.; Cheng, J.; Mader, B. T.; Hoffmann, M. R., Treatment technologies for aqueous perfluorooctanesulfonate (PFOS) and perfluorooctanoate (PFOA). *Frontiers of Environmental Science & Engineering in China* **2009,** *3* (2), 129-151.
246. Carter, K. E.; Farrell, J., Oxidative destruction of perfluorooctane sulfonate using boron-doped diamond film electrodes. *Environmental science & technology* **2008,** *42* (16), 6111-6115.
247. Taylor, P.; Yamada, T.; Striebich, R.; Graham, J.; Giraud, R., Investigation of waste incineration of fluorotelomer-based polymers as a potential source of PFOA in the environment. *Chemosphere* **2014,** *110*, 17-22.
248. Gu, Y.; Liu, T.; Wang, H.; Han, H.; Dong, W., Hydrated electron based decomposition of perfluorooctane sulfonate (PFOS) in the VUV/sulfite system. *Science of the Total Environment* **2017,** *607*, 541-548.
249. Yu, K.; Li, X.; Chen, L.; Fang, J.; Chen, H.; Li, Q.; Chi, N.; Ma, J., Mechanism and efficiency of contaminant reduction by hydrated electron in the sulfite/iodide/UV process. *Water research* **2018,** *129*, 357-364.
250. Ochoa-Herrera, V.; Sierra-Alvarez, R., Removal of perfluorinated surfactants by sorption onto granular activated carbon, zeolite and sludge. *Chemosphere* **2008,** *72* (10), 1588-1593.
251. Tang, C. Y.; Fu, Q. S.; Robertson, A.; Criddle, C. S.; Leckie, J. O., Use of reverse osmosis membranes to remove perfluorooctane sulfonate (PFOS) from semiconductor wastewater. *Environmental science & technology* **2006,** *40* (23), 7343-7349.

252. Ross, I.; McDonough, J.; Miles, J.; Storch, P.; Thelakkat Kochunarayanan, P.; Kalve, E.; Hurst, J.; S. Dasgupta, S.; Burdick, J., A review of emerging technologies for remediation of PFASs. *Remediation Journal* **2018,** *28* (2), 101-126.
253. Herrmann, J.-M., Heterogeneous photocatalysis: fundamentals and applications to the removal of various types of aqueous pollutants. *Catalysis today* **1999,** *53* (1), 115-129.
254. Yamamoto, T.; Noma, Y.; Sakai, S.-i.; Shibata, Y., Photodegradation of perfluorooctane sulfonate by UV irradiation in water and alkaline 2-propanol. *Environmental science & technology* **2007,** *41* (16), 5660-5665.
255. Lyu, X.-J.; Li, W.-W.; Lam, P. K.; Yu, H.-Q., Insights into perfluorooctane sulfonate photodegradation in a catalyst-free aqueous solution. *Scientific reports* **2015,** *5*, 9353.
256. Buxton, G. V.; Greenstock, C. L.; Helman, W. P.; Ross, A. B., Critical review of rate constants for reactions of hydrated electrons, hydrogen atoms and hydroxyl radicals (· OH/· O− in aqueous solution. *Journal of physical and chemical reference data* **1988,** *17* (2), 513-886.
257. Edition, F., Guidelines for drinking-water quality. *WHO chronicle* **2011,** *38* (4), 104-8.
258. Colomban, C. d.; Kudrik, E. V.; Afanasiev, P.; Sorokin, A. B., Catalytic defluorination of perfluorinated aromatics under oxidative conditions using N-bridged diiron phthalocyanine. *Journal of the American Chemical Society* **2014,** *136* (32), 11321-11330.
259. Marcus, R. A., Electron transfer reactions in chemistry. Theory and experiment. *Reviews of Modern Physics* **1993,** *65* (3), 599.
260. Christopher, P.; Xin, H.; Linic, S., Visible-light-enhanced catalytic oxidation reactions on plasmonic silver nanostructures. *Nature chemistry* **2011,** *3* (6), 467-472.
261. Closs, G.; Calcaterra, L.; Green, N.; Penfield, K.; Miller, J., Distance, stereoelectronic effects, and the Marcus inverted region in intramolecular electron transfer in organic radical anions. *The Journal of Physical Chemistry* **1986,** *90* (16), 3673-3683.
262. Chen, P.; McCreery, R. L., Control of electron transfer kinetics at glassy carbon electrodes by specific surface modification. *Analytical Chemistry* **1996,** *68* (22), 3958-3965.
263. Tomasi, J.; Bonaccorsi, R.; Cammi, R.; del Valle, F. J. O., Theoretical chemistry in solution. Some results and perspectives of the continuum methods and in particular of the polarizable continuum model. *Journal of Molecular Structure: THEOCHEM* **1991,** *234*, 401-424.
264. Del Valle, F. O.; Tomasi, J., Electron correlation and solvation effects. I. Basic formulation and preliminary attempt to include the electron correlation in the quantum mechanical polarizable continuum model so as to study solvation phenomena. *Chemical Physics* **1991,** *150* (2), 139-150.
265. Zhao, Y.; Truhlar, D. G., The M06 suite of density functionals for main group thermochemistry, thermochemical kinetics, noncovalent interactions, excited states, and transition elements: two new functionals and systematic testing of four M06-class functionals and 12 other functionals. *Theoretical Chemistry Accounts* **2008,** *120* (1-3), 215-241.
266. Pari, S.; Wang, I. A.; Liu, H.; Wong, B. M., Sulfate radical oxidation of aromatic contaminants: a detailed assessment of density functional theory and high-level quantum chemical methods. *Environmental Science: Processes & Impacts* **2017,** *19* (3), 395-404.
267. Grisenti, R.; Schöllkopf, W.; Toennies, J.; Hegerfeldt, G.; Köhler, T.; Stoll, M., Determination of the bond length and binding energy of the helium dimer by diffraction from a transmission grating. *Physical Review Letters* **2000,** *85* (11), 2284.
268. Szajdzinska-Pietek, E.; Gebicki, J.; Kroh, J., Pulse radiolytic investigation on intermicellar transport of hydrated electron in cationic micellar solutions of alkyltrimethylammonium halides. *Journal of colloid and interface science* **1995,** *176* (1), 264-266.
269. Nassar, A.-E. F.; Willis, W. S.; Rusling, J. F., Electron transfer from electrodes to myoglobin: facilitated in surfactant films and blocked by adsorbed biomacromolecules. *Analytical chemistry* **1995,** *67* (14), 2386-2392.

270. Bunton, C. A.; Nome, F.; Quina, F. H.; Romsted, L. S., Ion binding and reactivity at charged aqueous interfaces. *Accounts of chemical research* **1991,** *24* (12), 357-364.
271. Paul, A.; Wannere, C. S.; Schaefer, H. F., Do linear-chain perfluoroalkanes bind an electron? *The Journal of Physical Chemistry A* **2004,** *108* (43), 9428-9434.
272. Statistics, F., Food and Agriculture Organization of the United Nations. *Retrieved* **2010,** *3* (13), 2012.
273. Liu, J.; Avendaño, S. M., Microbial degradation of polyfluoroalkyl chemicals in the environment: a review. *Environment international* **2013,** *61*, 98-114.
274. McCarty, P. L. In *Biotic and abiotic transformations of chlorinated solvents in ground water*, Symposium on Natural Attenuation of Chlorinated Organics in Ground Water, Dallas/TX, 1996; pp 5-9.
275. Harding, K. C. Biotransformation of Persistent Groundwater Contaminants: Trichloroethene and Poly-and Perfluoroalkyl Substances (PFASs). UC Berkeley, 2014.
276. Ruder, A. M., Potential health effects of occupational chlorinated solvent exposure. *Annals of the New York Academy of Sciences* **2006,** *1076* (1), 207-227.
277. Sharma, B. M.; Bharat, G. K.; Tayal, S.; Larssen, T.; Bečanová, J.; Karásková, P.; Whitehead, P. G.; Futter, M. N.; Butterfield, D.; Nizzetto, L., Perfluoroalkyl substances (PFAS) in river and ground/drinking water of the Ganges River basin: emissions and implications for human exposure. *Environmental pollution* **2016,** *208*, 704-713.
278. da Silva-Rackov, C. K.; Lawal, W. A.; Nfodzo, P. A.; Vianna, M. M.; do Nascimento, C. A.; Choi, H., Degradation of PFOA by hydrogen peroxide and persulfate activated by iron-modified diatomite. *Applied Catalysis B: Environmental* **2016,** *192*, 253-259.
279. Lee, Y.-C.; Lo, S.-L.; Kuo, J.; Lin, Y.-L., Persulfate oxidation of perfluorooctanoic acid under the temperatures of 20–40 C. *Chemical Engineering Journal* **2012,** *198*, 27-32.
280. Schröder, H. F.; Meesters, R. J., Stability of fluorinated surfactants in advanced oxidation processes—a follow up of degradation products using flow injection–mass spectrometry, liquid chromatography–mass spectrometry and liquid chromatography–multiple stage mass spectrometry. *Journal of Chromatography A* **2005,** *1082* (1), 110-119.
281. Liu, C.; Shih, K.; Wang, F., Oxidative decomposition of perfluorooctanesulfonate in water by permanganate. *Separation and Purification Technology* **2012,** *87*, 95-100.
282. Liao, Z.; Farrell, J., Electrochemical oxidation of perfluorobutane sulfonate using boron-doped diamond film electrodes. *Journal of applied electrochemistry* **2009,** *39* (10), 1993-1999.
283. Huang, L.; Dong, W.; Hou, H., Investigation of the reactivity of hydrated electron toward perfluorinated carboxylates by laser flash photolysis. *Chemical Physics Letters* **2007,** *436* (1-3), 124-128.
284. Li, X.; Fang, J.; Liu, G.; Zhang, S.; Pan, B.; Ma, J., Kinetics and efficiency of the hydrated electron-induced dehalogenation by the sulfite/UV process. *Water research* **2014,** *62*, 220-228.
285. Sun, Z.; Zhang, C.; Chen, P.; Zhou, Q.; Hoffmann, M. R., Impact of humic acid on the photoreductive degradation of perfluorooctane sulfonate (PFOS) by UV/Iodide process. *Water research* **2017,** *127*, 50-58.
286. Yamijala, S. S. R. K. C.; Shinde, R.; Wong, B. M., Real-time degradation dynamics of hydrated per- and polyfluoroalkyl substances (PFASs) in the presence of excess electrons. *Phys Chem Chem Phys* **2020**.
287. Qu, Y.; Zhang, C.; Li, F.; Chen, J.; Zhou, Q., Photo-reductive defluorination of perfluorooctanoic acid in water. *Water research* **2010,** *44* (9), 2939-2947.
288. Hansen, M. C.; Børresen, M. H.; Schlabach, M.; Cornelissen, G., Sorption of perfluorinated compounds from contaminated water to activated carbon. *Journal of Soils and Sediments* **2010,** *10* (2), 179-185.

289. Bentel, M. J.; Yu, Y.; Xu, L.; Li, Z.; Wong, B. M.; Men, Y.; Liu, J., Defluorination of per-and polyfluoroalkyl substances (PFASs) with hydrated electrons: structural dependence and implications to PFAS remediation and management. *Environmental science & technology* **2019,** *53* (7), 3718-3728.
290. Luckhaus, D.; Yamamoto, Y.-i.; Suzuki, T.; Signorell, R., Genuine binding energy of the hydrated electron. *Science advances* **2017,** *3* (4), e1603224.
291. Zhao, L.; Bian, J.; Zhang, Y.; Zhu, L.; Liu, Z., Comparison of the sorption behaviors and mechanisms of perfluorosulfonates and perfluorocarboxylic acids on three kinds of clay minerals. *Chemosphere* **2014,** *114*, 51-58.
292. Pan, G.; Jia, C.; Zhao, D.; You, C.; Chen, H.; Jiang, G., Effect of cationic and anionic surfactants on the sorption and desorption of perfluorooctane sulfonate (PFOS) on natural sediments. *Environmental Pollution* **2009,** *157* (1), 325-330.
293. Du, Z.; Deng, S.; Chen, Y.; Wang, B.; Huang, J.; Wang, Y.; Yu, G., Removal of perfluorinated carboxylates from washing wastewater of perfluorooctanesulfonyl fluoride using activated carbons and resins. *Journal of hazardous materials* **2015,** *286*, 136-143.
294. Costentin, C.; Robert, M.; Savéant, J.-M., Stepwise and concerted electron-transfer/bond breaking reactions. Solvent control of the existence of unstable π ion radicals and of the activation barriers of their heterolytic cleavage. *Journal of the American Chemical Society* **2004,** *126* (51), 16834-16840.
295. Li, X.; Chen, S.; Quan, X.; Zhang, Y., Enhanced adsorption of PFOA and PFOS on multiwalled carbon nanotubes under electrochemical assistance. *Environmental science & technology* **2011,** *45* (19), 8498-8505.
296. Melander, L. C.; Saunders, W. H., *Reaction rates of isotopic molecules*. John Wiley & Sons: 1980.
297. Hofstetter, T. B.; Reddy, C. M.; Heraty, L. J.; Berg, M.; Sturchio, N. C., Carbon and chlorine isotope effects during abiotic reductive dechlorination of polychlorinated ethanes. *Environmental science & technology* **2007,** *41* (13), 4662-4668.
298. Marcus, R. A.; Sutin, N., Electron transfers in chemistry and biology. *Biochimica et Biophysica Acta (BBA)-Reviews on Bioenergetics* **1985,** *811* (3), 265-322.
299. Nelsen, S. F.; Blomgren, F., Estimation of Electron Transfer Parameters from AM1 Calculations. *The Journal of Organic Chemistry* **2001,** *66* (20), 6551-6559.
300. Newton, M. D., Quantum chemical probes of electron-transfer kinetics: the nature of donor-acceptor interactions. *Chemical Reviews* **1991,** *91* (5), 767-792.
301. Fortunelli, A.; Tomasi, J., The Implementation of Density-Functional Theory within the Polarizable Continuum Model for Solvation. *Chem Phys Lett* **1994,** *231* (1), 34-39.
302. Tomasi, J.; Bonaccorsi, R.; Cammi, R.; Delvalle, F. J. O., Theoretical Chemistry in Solution - Some Results and Perspectives of the Continuum Methods and in Particular of the Polarizable Continuum Model. *Theochem-J Mol Struc* **1991,** *80*, 401-424.
303. Delvalle, F. J. O.; Bonaccorsi, R.; Cammi, R.; Tomasi, J., Electron Correlation and Solvation Effects .3. Influence of the Basis Set and the Chemical-Composition on the Solvation Energy Components Evaluated with the Quantum-Mechanical Polarizable Continuum Model. *Theochem-J Mol Struc* **1991,** *76*, 295-312.
304. Delvalle, F. J. O.; Tomasi, J., Electron Correlation and Solvation Effects .1. Basic Formulation and Preliminary Attempt to Include the Electron Correlation in the Quantum-Mechanical Polarizable Continuum Model So as to Study Solvation Phenomena. *Chem Phys* **1991,** *150* (2), 139-150.
305. Aguilar, M. A.; Delvalle, F. J. O.; Tomasi, J., Electron Correlation and Solvation Effects .2. The Description of the Vibrational Properties of a Water Molecule in a Dielectric Given by the Application of the Polarizable Continuum Model with Inclusion of Correlation-Effects. *Chem Phys* **1991,** *150* (2), 151-161.

306. Raza, A.; Bardhan, S.; Xu, L.; Yamijala, S. S. R. K. C.; Lian, C.; Kwon, H.; Wong, B. M., A Machine Learning Approach for Predicting Defluorination of Per- and Polyfluoroalkyl Substances (PFAS) for Their Efficient Treatment and Removal. *Environmental Science & Technology Letters* **2019,** *6* (10), 624-629.
307. Li, K.; Stefan, M. I.; Crittenden, J. C., UV photolysis of trichloroethylene: Product study and kinetic modeling. *Environmental science & technology* **2004,** *38* (24), 6685-6693.
308. Chuang, Y.-H.; Chen, S.; Chinn, C. J.; Mitch, W. A., Comparing the UV/monochloramine and UV/free chlorine advanced oxidation processes (AOPs) to the UV/hydrogen peroxide AOP under scenarios relevant to potable reuse. *Environmental science & technology* **2017,** *51* (23), 13859-13868.
309. Lim, T. H.; Kim, S. D., Trichloroethylene degradation by photocatalysis in annular flow and annulus fluidized bed photoreactors. *Chemosphere* **2004,** *54* (3), 305-312.
310. Jin, F.; Wei, M.; Liu, C.; Ma, Y., The mechanism for the formation of OH radicals in condensed-phase water under ultraviolet irradiation. *Physical Chemistry Chemical Physics* **2017,** *19* (32), 21453-21460.